Multiscale dual-continuum modelling of deformable porous media

Mark Ashworth

Submitted for the degree of Doctor of Philosophy
Institute of GeoEnergy Engineering
Heriot-Watt University

Thursday 11th February, 2021

Abstract

Within the geosciences, we are often challenged by how to model the coupling of physical phenomena across varying space and time scales, as well as between different phenomena themselves. As a result, we forgo accuracy and physical consistency/understanding, in favour of efficiency and practicality. To address these tradeoffs we can use multiscale and multiphysics modelling. In this work, we are concerned with multiscale behaviours owing to the coupling between a microscale model and a (macroscopic) dual-continuum model. For the multiphysics component, we consider the coupling between linear deformation and flow, referred to as poroelasticity.

Accordingly, the goal of this thesis is to apply multiscale and multiphysics modelling concepts to the study of strongly heterogeneous (deformable) porous media, to better understand and represent the links between various scales of interest. We split this work into three main parts.

Part one investigates the relations between microscopic and dual-continuum poroelastic constitutive models, including previously introduced phenomenological models. To do so, we use micromechanical approaches. Subsequently, starting from the microscale, we derive a fully anisotropic dual-continuum poroelastic constitutive model using homogenisation. We then show how the resulting model is related to constitutive models available in literature. For these previously introduced models, we use micromechanical considerations and analytical solutions to compare and contrast the various modelling concepts used in their derivation. We also investigate various simplifying assumptions made by past users of these models. On the basis of our studies we provide recommendations for how and when to use the various dual-continuum poroelastic constitutive modelling concepts and simplifications.

Part two introduces a numerical framework for poroelastic dual-continuum modelling. We subsequently use this framework to further study the links between microscale and macroscale poroelastic materials. Our numerical framework considers anisotropy and uses a hybrid discretisation suited for the flow and deformation subproblems accordingly. We benchmark the resulting framework against analytical solutions and demonstrate its use on a complex geological grid. With the framework in-hand we compare and study dual-continuum behaviours against microscale representations given various modelling and material assumptions on the latter. We present a number of tests starting from isotropic

cases, progressing to more complex anisotropic cases. Our results show that anisotropy can have measurable effects on coupled behaviours. However, for the tests considered, we show the dual-continuum approach is capable of capturing the global poroelastic behaviours of microscopic representations.

Finally, part three establishes a computational multiscale approach based on machine learning to improve the accuracy of macroscopic approaches in subsurface modelling. Here the idea is to use data-driven modelling as a surrogate constitutive model within a hierarchical multiscale setting. Accordingly, we detail the framework, describing the key components and considerations therein. We then apply the framework to the problem of inter-continuum mass transfer, whilst considering an uncoupled (flow only) dual-continuum representation. We couple the resulting data-driven model to a physics-based model leading to a hybrid machine learning-physics-based approach. We show the resulting hybrid method to give high quality results with respect to a microscale model, without the computational expense of the latter.

For my teachers

Acknowledgements

As the saying goes 'the journey is often more important than the destination'. So I would like to thank all of those who have made the time leading up to this thesis an incredible journey.

First, my deep thanks to my supervisor Florian Doster, for your constant support, time and guidance over the years, and allowing me the freedom to learn and grow. Further thanks to Sebastian Geiger, I am always amazed, and inspired, by how you manage your research group with such warmth and compassion, whilst also being an exemplary academic. To Ahmed Elsheikh, although short, I am happy to have had the time to work and learn from you, and I hope we get the chance to collaborate again in the future. A last thank you to the teachers and educators that I have not mentioned, but who have continually inspired me over the years through school, university, books and online resources.

I am very grateful for the financial aid provided by Heriot-Watt University and the National Environmental Research Council, without which this experience would not have been possible. Further thanks also to my examiners, Matteo Icardi and Jingsheng Ma, for taking the time and effort to review this work.

Thank you to past and present colleagues within the Carbonates Reservoir family, our MuPhi family and the rest of Energy Academy. Being in such a diverse multicultural and multifaceted community has broadened my horizons and my taste buds. My mind and stomach are grateful. Special thanks also go to the more localised group from room 1.14: Aman, Atish and Masoud for making lunches, and brief moments of procrastination, enjoyable parts of my day.

To the friends I've made on the PhD journey outside of the research community. This includes the amazing people I've had the pleasure of living with, and those I've met through NERC. To my older friends 'The Boys' from home (aka. Babs, Chez, Darves, Jonah, Leo, Mike, Munt) and Harris, you have all been like brothers to me.

Lastly, thank you to my family. First, to Anne-Sophie Ruget. Your kindness and love are an ever-present source of strength, and I feel lucky to be on your team both as a partner and friend. Also, more importantly, thank you for getting me into running. To Greg and Huda Lane, I hope I can return a fraction of the advice, care and laughter you have given me over the years. To Dad, thank you for your support and for showing me the things not to look for in life. To my auntie, grandma and remainder of my family who have all taught me alot, even

if not intentionally. And finally, to mum, you are an inspiration and a legend, thank you for all you have done for me over the years.

<div align="right">Thursday 11th February, 2021</div>

Research Thesis Submission

Please note this form should be bound into the submitted thesis.

Name*:*	Mark Ashworth			
School:	EGIS			
Version: *(i.e. First, Resubmission, Final)*	Final	Degree Sought:	PhD	

Declaration

In accordance with the appropriate regulations I hereby submit my thesis and I declare that:

1. The thesis embodies the results of my own work and has been composed by myself
2. Where appropriate, I have made acknowledgement of the work of others
3. The thesis is the correct version for submission and is the same version as any electronic versions submitted*.
4. My thesis for the award referred to, deposited in the Heriot-Watt University Library, should be made available for loan or photocopying and be available via the Institutional Repository, subject to such conditions as the Librarian may require
5. I understand that as a student of the University I am required to abide by the Regulations of the University and to conform to its discipline.
6. I confirm that the thesis has been verified against plagiarism via an approved plagiarism detection application e.g. Turnitin.

ONLY for submissions including published works

Please note you are only required to complete the Inclusion of Published Works Form (page 2) if your thesis contains published works)

7. Where the thesis contains published outputs under Regulation 6 (9.1.2) or Regulation 43 (9) these are accompanied by a critical review which accurately describes my contribution to the research and, for multi-author outputs, a signed declaration indicating the contribution of each author (complete)
8. Inclusion of published outputs under Regulation 6 (9.1.2) or Regulation 43 (9) shall not constitute plagiarism.

*   *Please note that it is the responsibility of the candidate to ensure that the correct version of the thesis is submitted.*

Signature of Candidate*:*	*[signature]*	Date:	11-Feb-21

Submission

Submitted By *(name in capitals):*	MARK ASHWORTH
Signature of Individual Submitting:	*[signature]*
Date Submitted:	11-Feb-21

For Completion in the Student Service Centre (SSC)

Limited Access	Requested	Yes		No		Approved	Yes		No	
*E-thesis Submitted (**mandatory for final theses**)*										
Received in the SSC by *(name in capitals):*						Date:				

Inclusion of Published Works

Declaration

This thesis contains one or more multi-author published works. In accordance with Regulation 6 (9.1.2) I hereby declare that the contributions of each author to these publications is as follows:

Citation details	Ashworth, M. and Doster, F., 2019, March. An Open Source Numerical Framework for Dual-Continuum Geomechanical Simulation. In *SPE Reservoir Simulation Conference*. Society of Petroleum Engineers.
Author 1	Coded the framework and analytical solutions, wrote the manuscript.
Author 2	Desgined the question, read and suggested corrections / improvements to manuscript.
Signature:	
Date:	11-Feb-21

Citation details	Ashworth, M. and Doster, F., 2019. Foundations and their practical implications for the constitutive coefficients of poromechanical dual-continuum models. *Transport in Porous Media*, *130* (3), pp.699-730.
Author 1	Expanded the question, conducted the investigations, wrote the manuscript.
Author 2	Designed the question, read and suggested corrections / improvements to manuscript.
Signature:	
Date:	11-Feb-21

Citation details	Ashworth, M. and Doster, F., 2020. Anisotropic dual-continuum representations for multiscale poroelastic materials: Development and numerical modelling. *International Journal for Numerical and Analytical Methods in Geomechanics*, *44*(17), pp.2304-2328.
Author 1	Desgined the question, derived the model, wrote the manuscript.
Author 2	Read and suggested corrections / improvements to manuscript.
Signature:	
Date:	11-Feb-21

Contents

List of Figures

List of Tables

Notation

0	Reference conditions / configuration
$\hat{}$	Boundary assigned values
$\bar{}$	Volume average
$\bar{}_\alpha$	Intrinsic volume average over material phase α
$*$	Homogenised (effective) quantities (superscript)
α	Continuum alpha $[\alpha = m, f]$ (subscript)
β	Continuum beta such that $\beta \neq \alpha$ (subscript)
l	Fluid quantities (subscript)
m	Matrix quantities (subscript)
f	Fracture quantities (subscript)
s	Solid quantities (subscript)
a_f	Fracture aperture
A_{11-33}	Constitutive parameters for the macroscopic pure stiffness constitutive formulation as per Berryman (2002)
A	Strain concentration factor
$\mathbb{A}$	Strain concentration tensor
B	Stress concentration factor
$\mathbb{B}$	Stress concentration tensor
$\mathbf{b}, \mathbf{B}$	Microscopic and macroscopic tensorial Biot coefficient
$\mathcal{B}$	Microscopic Skempton coefficient
C	Macroscopic consolidation coefficient
d	Space dimension
$\boldsymbol{\epsilon}, \mathbf{E}$	Microscopic and macroscopic (linearised) strain tensor
E	Volumetric strain
E	Young's modulus
$\mathcal{F}_s$	Potential energy density of the skeleton
$\mathbf{g}$	Gravity acceleration vector
Γ	Edge

γ_α	Inter-continuum mass transfer rate for continuum α
γ'	Momentum source
$h(\cdot)$	Activation function
$\mathcal{H}_s$	Helmholtz free energy of the skeleton
$\mathbf{1}$	Second-order identity tensor
$\mathbb{I}$	Fourth-order identity tensor
K	Bulk modulus
K_ϕ	Pore modulus
k'	Interface permeability
$\mathbf{k}, \mathbf{K}$	Microscopic and Macroscopic permeability tensor
ℓ	Characteristic size of heterogeneities
l	Characteristic size of an REV
L	Characteristic size of a macroscopic structure
λ	Lamé constant
$m_{l,\alpha}$	Fluid mass content
m, M	Microscopic and macroscopic Biot modulus (variation of fluid volume content formulation)
μ_l	Fluid viscosity
$\mathbf{n}$	Unit surface normal vector
N_f	Number of fracture sets
n, N	Microscopic and macroscopic Biot modulus (variation of porosity formulation)
ν	Poisson ratio
Ω	Elementary volume
$\partial\Omega$	The boundary of Ω
Ω^p	Pore volume
$\Omega^{\mathcal{D}}$	(Arbitrary) domain volume
p, P	Microscopic and macroscopic fluid pressure
ψ_α	Pore fraction for continuum α
$\mathbf{q}$	Volume flux vector
Q	Cross-coupling modulus
φ, ϕ	Microscopic and macroscopic Lagrangian porosity
ρ	Bulk (solid and fluid) density
ρ_l	Intrinsic fluid density
S	Compliance modulus

$\mathbb{S}$	Compliance tensor
$\boldsymbol{\sigma}, \boldsymbol{\Sigma}$	Microscopic and macroscopic (Cauchy) stress tensor
Σ	Mean stress
$\boldsymbol{\sigma}', \boldsymbol{\Sigma}'$	Microscopic and macroscopic effective (Cauchy) stress tensor
$\boldsymbol{\theta}, \boldsymbol{\Theta}$	Basis function vector and matrix
ϑ	Macroscopic Eulerian porosity
$\mathbf{u}, \mathbf{U}$	Microscopic and macroscopic displacement vector
v	Volume fraction
v_l	Absolute fluid velocity
$\boldsymbol{w}$	Mass flux vector
$\mathbf{w}, \mathbf{W}$	Weight vector and matrix
$\mathcal{W}_s$	Strain work density of the skeleton
$\boldsymbol{x}, \mathbf{X}$	Microscopic and macroscopic position vector
$\mathbf{x}, \mathbf{X}$	Input (feature) vector and matrix
$y, \mathbf{y}$	Output (target) variable and vector
ξ	Fluid volume content
z	Arbitrary field

Vector and tensor notation

Using Einstein convention where summation is implied over repeated indices:

$$c = \mathbf{a} \cdot \mathbf{b} \quad \equiv \quad c = a_i b_i$$

$$\mathbf{c} = \mathbf{A} \cdot \mathbf{b} \quad \equiv \quad c_i = A_{ij} b_j$$

$$\mathbf{C} = \mathbf{a} \otimes \mathbf{b} \quad \equiv \quad C_{ij} = a_i b_j$$

$$c = \mathrm{tr}(\mathbf{A}) \quad \equiv \quad c = A_{ii}$$

$$c = \mathbf{A} : \mathbf{B} \quad \equiv \quad c = A_{ij} B_{ij}$$

$$\mathbf{C} = \mathbf{A} \cdot \mathbf{B} \quad \equiv \quad C_{ij} = A_{ik} B_{kj}$$

$$\mathbb{C} = \mathbf{A} \otimes \mathbf{B} \quad \equiv \quad C_{ijkl} = A_{ij} B_{kl}$$

$$\nabla a \quad \equiv \quad \partial a / \partial x_i$$

$$\nabla \mathbf{a} \quad \equiv \quad \partial a_i / \partial x_j$$

$$\nabla \cdot \mathbf{a} \quad \equiv \quad \partial a_i / \partial x_i$$

$$\nabla \cdot \mathbf{A} \quad \equiv \quad \partial A_{ij} / \partial x_j$$

Abbreviations

DC   Dual-continuum

MS   Microscale (explicit, fine-scale)

FC-NN   Fully-connected neural network

ML   Machine learning

PR   Polynomial regression

REV   Representative elementary volume

Publications

This thesis contains excerpts from the following papers:

Ashworth, M. and Doster, F., 2019, March. An Open Source Numerical Framework for Dual-Continuum Geomechanical Simulation. In *SPE Reservoir Simulation Conference.* Society of Petroleum Engineers.
DOI: 10.2118/193846-MS

Ashworth, M. and Doster, F., 2019. Foundations and their practical implications for the constitutive coefficients of poromechanical dual-continuum models. *Transport in Porous Media*, 130(3), pp.699-730.
DOI: 10.1007/s11242-019-01335-6

Ashworth, M. and Doster, F., 2020. Anisotropic dual-continuum representations for multiscale poroelastic materials: Development and numerical modelling. *International Journal for Numerical and Analytical Methods in Geomechanics*,
DOI: 10.1002/nag.3140

Ashworth, M., Elsheikh, A. and Doster, F. Machine learning-based multiscale constitutive modelling: Development and application to a multiscale pressure diffusion problem. *In preparation*

1

Introduction

In various fields of science and engineering, mathematical models give us the ability to develop physical insights and make predictions about behaviours beyond our observations. For example, the role of modelling plays a critical part in informing high cost, high risk subsurface activities such as geological storage, contaminant transport, and energy and groundwater extraction. However, choosing the 'best'[1] model for a given task is nontrivial, particularly when faced with a number of complex interdependent processes.

In the subsurface, strong heterogeneities exist within the rock fabric, as well as between the solids and saturating fluids. Subsequently, contrasts in material properties lead to strong couplings across space and time scales (*multiscale* phenomena), and between different physics (*multiphysics* phenomena). Given multiscale, multiphysics effects we now have a modelling dilemma: How complex can we afford, and do we need, our models to be? Depending on resources and requirements, modelling at the heterogeneity scale (*microscale*) may be intractable or provide more information than necessary. One possible solution is to use coarser (*macroscale*) models that consider an aggregation of physics over the microscale. Now, two important questions are: How do we encode microscale information that we do not directly model at the macroscale? And, how do assumptions at the microscale affect what we observe at the macroscale?

The latter questions above form recurring themes in this thesis. Subsequently, our objective in this dissertation is to investigate these questions within the context of strongly heterogenous porous media, with and without multiphysics behaviours. At the macroscale we use an implicit macroscopic modelling approach referred to as a dual-continuum model. In this paradigm we account for strong differences in timescale behaviour between two different characteristic porosity levels. For the multiphysics component, we are interested in the interactions between flow and linear deformation, referred to as poroelasticity within literature (e.g. Coussy 2004). In both cases, we endeavour to increase our un-

---

[1]Following Brooks and Tobias (1996), we refer to 'best' as a model that manages the trade-off between accuracy, complexity and efficiency.

derstanding of the links between microscopic and macroscopic representations using a range of modelling tools. Further, we wish to investigate new techniques in which we can pass information between scales.

For the remainder of this chapter we detail the topics and ideas explored in this work, finishing with the contributions and outline of this thesis.

1.1 Dual-continuum models

Geological materials exhibit strong heterogeneities in material properties over local and regional scales due to a variety of rock forming and altering processes (Geiger et al. 2004). Classic examples of such materials within the subsurface are naturally fractured rocks and aggregated soils (Nelson 2001; Gerke 2006; Borja and Koliji 2009; Adler et al. 2013). Perhaps the most intuitive approach to modelling these materials is to model them at the scale of the heterogeneity. So called explicit methods (Fig. 1.1), benefit from capturing high degrees of detail (Karimi-Fard et al. 2003), which can be important for costly decision making. However, over large scales such models are resource intensive, both from computational and data points of view, as well as being difficult to interpret and calibrate (Berkowitz 2002). To alleviate these challenges, we can reduce modelling complexity by replacing our heterogeneous microscale model with an 'equivalent' homogeneous macroscopic model. These latter type models are often referred to as implicit models (Berre et al. 2019) (Fig. 1.1).
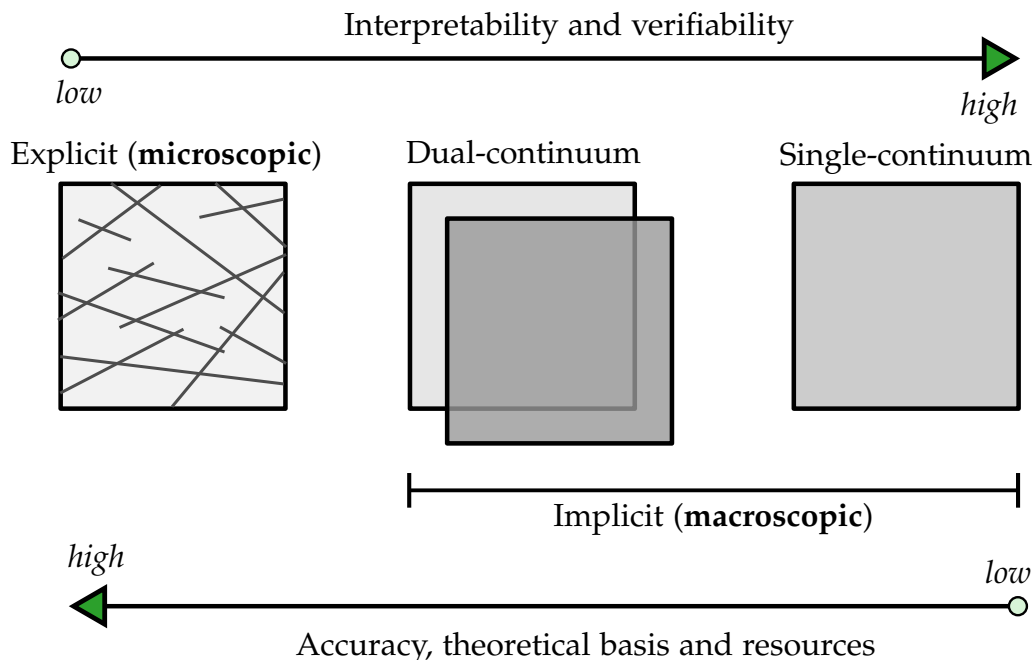
Figure 1.1: Modelling scales and approaches.

A natural starting point for replacing our heterogeneous material would be to use a single equivalent medium (Fig. 1.1). In this case, microscopic field variables and properties are replaced with effective equivalents at the macroscale. From a

theoretical point of view, adopting a continuum perspective over the microscale requires length scales over which material statistics and the wavelengths of physical processes remain stable (Hill 1963; Auriault 2002; Geers et al. 2010). However, in the case of fractured materials, identification of such scales is strongly debated due to the absence of characteristic length scales in fracture growth processes (Bonnet et al. 2001). Nevertheless, despite difficulties in identifying characteristic length scales, from a practical point of view it is often desirable to enable at least some form of effective description when modelling (Berkowitz 2002). Finally, single-continuum models can be inappropriate in cases where strong differences in timescale behaviour exist between different heterogeneity levels. As a result, these models tend to oversimplify the physics causing measurable inaccuracies (Lewandowska et al. 2004; Samardzioska and Popov 2005).

Multi-continuum models combat the disadvantage of single-continuum models described above, by modelling effective representations of the heterogeneities as distinct continua that overlap in space and time. Depending on the level of complexity required we are not restricted by the number of overlapping continua we can model (Pruess et al. 1985). However, the simplest and most common approach is to consider two interacting continua, leading to the so called dual-continuum (DC) model (Barenblatt et al. 1960; Warren and Root 1963) (Fig. 1.1).

In the dual-continuum paradigm one continuum typically represents a high storage, low permeability material (e.g. matrix). The other then represents a low storage, high permeability material (e.g. fractures). Depending on the dual-continuum model formulation, macroscopic communication across the storage material is either neglected (dual-porosity) or permitted (dual-permeability). Besides descriptions of *intra*-continuum communication, the other fundamental ingredient to the DC model is *inter*-continuum communication.

In flow modelling, inter-continuum communication concerns mass transfer between the two materials. Inter-continuum mass transfer is an area of much interest within the DC literature (e.g. Zimmerman et al. 1993; Lim and Aziz 1995; Haggerty and Gorelick 1995; Geiger et al. 2013). Here the challenge comes from the hysteretic dependence of the transfer model. As a result, the model is described as a convolution product over previous time levels leading to explicit time dependence (Royer et al. 1996). However, these complicated explicit time formulations are unsuitable for numerical modelling (Lim and Aziz 1995; Royer et al. 1996). Subsequently, it is common to remove explicit time by modelling the mass transfer as a linear function of the two continuum pressures (Barenblatt et al. 1960; Warren and Root 1963; Gerke and Van Genuchten 1993; Lim and Aziz 1995). The cost of this simplification is the introduction of errors in DC flow behaviour due to neglecting higher order transient terms at early time (Zimmerman et al. 1993).

On the basis of the above we identify two main challenges with the implicit modelling approach. The first is the identification, or lack, of suitable length scales over which an implicit approach can be justified. The second is formulating relations between macroscopic quantities, such as for inter-continuum mass transfer. In this work we align ourselves with the latter problem due to its commonality with the main themes of this thesis. We explore the details of this type of challenge in the following section of this chapter.

1.2 Multiscale modelling

Multiscale modelling encompasses a range of methods using multiple models simultaneously to describe scale dependent phenomena. Practically, there are two important situations when such an approach may be useful: First, in the presence of singularities, or in regions with high macroscopic gradients, there is a lack of scale separation in terms of the physical processes involved (Kouznetsova et al. 2004). Consequently, the two scales are strongly coupled and we need to use different scales, or methodologies, within different parts of our domain (Fish 2006). These types of problems are referred to as *concurrent* multiscale problems (Matouš et al. 2017). Alternatively, in regions where scales are not strongly coupled, coarser representations can be justified. However, and concerning the second situation, we may require microscale models to supplement missing constitutive information at the macroscale. Addressing this problem is the goal of micromechanics (Hashin 1983), where bridging between the micro and macroscales is then referred to as *homogenisation* (Babuška 1976). Accordingly, in this thesis we align ourselves with this latter, *hierarchical* multiscale modelling problem.

The hierarchical micromechanical problem described above can be addressed using analytical and/or computational approaches. With respect to the former, the earliest attempts to describe the effective macroscopic properties of microscopically heterogeneous materials came using the mixture rules provided by Voigt (1887, 1928) and Reuss (1929). These rules were developed whilst considering composite materials. Important developments with regards to composite material modelling then came from Eshelby (1957), who gave the solution to an elastic inclusion problem. A common theme held by Eshelby (1957) and others working around the same time-period, was a continuum description at the microscale. Subsequently, 'continuum micromechanics' was formally introduced by Hill (1965). Further analytical results and methods within this field were introduced by Hashin and Shtrikman (1963) and Hill (1963) (variational bounds), Budiansky (1965) and Hill (1965) (the self-consistent scheme), and Mori and Tanaka (1973) (mean-field homogenisation scheme) among others. We can group the ana-

lytical approaches, such as those just mentioned, under the term *micromechanical analysis*.

Computational approaches to multiscale modelling can be categorised according to their algorithmic basis. Following Matouš et al. (2017), these are parallel and sequential methods. In parallel methods, both scales are solved in a monolithic way. Alternatively, in sequential methods each scale is solved separately and information is passed between the scales. For example, information coming from the microscale could be precomputed offline and then called as needed in the macroscopic model. Nested finite-element methods (e.g. Feyel 1999; Kouznetsova et al. 2001), are a popular computational multiscale method that lie somewhere between parallel and sequential methods. In these approaches, microscopic boundary value problems are nested within points in the macroscopic domain, with the solution of the former providing information for the latter. In this sense, these methods are sequential. However, their solution is rather parallel in that equilibrium between both scales is established simultaneously through macro-micro and micro-macro compatibility conditions (Geers et al. 2017). Despite the effectiveness of these nested approaches, they can be computationally prohibitively to run at large scales, as well as producing significant amounts of data which needs to be stored and processed (Wang and Sun 2018). As a result, sequential methods remain popular (Stephenson et al. 2018).

Historically, sequential methods have involved the use of precomputed look-up tables (Weinan 2011). Interpolation schemes between points in these tables are then used when called by the macroscopic model. In this context, we can think of the look-up table and corresponding interpolation as a mapping linking various macroscopic fields. This mapping represents a *surrogate constitutive model* of input-output behaviour. More generally, surrogate modelling is the approximation of some unknown expensive-to-run function by one that is computationally cheaper-to-run (Razavi et al. 2012). Whilst the look-up table surrogate model is straightforward to understand, we lack a closed-form expression for the mapping. Accordingly, we acquire little knowledge about the function, the quality of our dataset and how well we may generalise to samples not included in the look-up table. An alternative to the look-up table approach is to somehow *learn* a surrogate model given our input-output data and other possible information. Learning such mappings is one of the fundamental goals of machine learning.

Machine learning (ML), or data-driven modelling, encompasses a range of algorithms that revise and update themselves from data in order to extract patterns, approximate functions or make sequential decisions. In the context of multiscale modelling ML is recieving increasing attention (Alber et al. 2019; Peng et al. 2020), with applications beyond the hierarchical multiscale scenario considered here. However, within the current context, ML methods form a natural

approach to sequential modelling of hierarchical multiscale problems. Indeed, these methods have been used to capture constitutive behaviour in multiscale settings in Wang and Sun (2018), Stephenson et al. (2018), Lu et al. (2019) and Ghavamian and Simone (2019) to name but a few. Given the surge in uptake of these approaches, it is interesting to further explore and develop their use in the multiscale setting considered in this work.

Lastly, with the increase in computing power, recent efforts into multiscale modelling have largely focused on computational developments (Weinan 2011). However, micromechanical analysis still remains useful for providing insight into multiscale behaviours and simplified models, as well as guidelines for the design of numerical procedures (Weinan 2011). Accordingly, in this thesis we consider both analytical and computational approaches to hierarchical multiscale modelling problems. For the latter, we are interested in data-driven approaches, with the focus being on the method rather than the application. For the former, we are interested in micromechanical analysis with applications to coupled flow and deformation processes in DC materials. This coupling, in the context of linear deformation, is referred to as poroelasticity and is explored in the next section.

1.3 Poroelasticity

Poroelasticity describes the coupling between fluid flow and linear deformation. Originally formulated by Biot (1941) on phenomenological grounds, this constitutive theory has since been supported through thermodynamical arguments (Biot and Temple 1972; Coussy 1995, 2004), theory of mixtures approaches (Bowen 1982; De Boer 2006) and homogenisation approaches (Burridge and Keller 1981; Chateau and Dormieux 2002; Dormieux et al. 2006) to name but a few. In its more common mixed compliance setting, the poroelastic constitutive theory relates a linear strain tensor and fluid pressure to the (Cauchy) stress tensor and porosity variation (Coussy 2004).

Within the context of dual-continua, the notion of flow and deformation coupling was first introduced by Aifantis (1977, 1979) and Wilson and Aifantis (1982). Later offerings then came from Elsworth and Bai (1992), Lewis and Ghafouri (1997) and Bai et al. (1999). However, the constitutive models presented in these works all made an implicit decoupling assumption within the DC poroelastic model. Specifically, the authors neglected the cross coupling effects of pressure changes in one continuum and porosity changes in the other continuum. The absence of these couplings was shown by Khalili (2003) to give nonphysical pressure responses for a uniaxial drainage problem. Specifically, the authors showed discontinuities in matrix and fracture pressures that were inconsistent with the

coupled response one would expect for the isotropic material geometry considered therein. The link between the observations made by Khalili (2003) and the role of pressure cross coupling still remains an open question. One goal of this work is to investigate this link in further detail.

Phenomenological models rectifying the decoupling deficiency mentioned above were introduced by Berryman and Wang (1995), Khalili and Valliappan (1996), Loret and Rizzi (1999), Berryman (2002) and Berryman and Pride (2002). These 'fully coupled' models differ in how the constitutive parameters of the DC poroelastic model are calculated. For example the models of Berryman and Wang (1995), Khalili and Valliappan (1996), Loret and Rizzi (1999) implicitly assume the transport phase to be all void space. In contrast, the models by Berryman (2002) and Berryman and Pride (2002) allow the same continuum to have an intrinsic stiffness.

The constitutive models introduced thus far formulate expressions for constitutive coefficients in terms of microscopic mechanical properties of the materials involved. Instead, Borja and Koliji (2009) and Choo and Borja (2015) use very different information: Based on thermodynamic arguments the authors derive a constitutive expression for stress, with relations for the constitutive coefficients formulated in terms of volume fractions. However, the authors stop short at deriving explicit constitutive expressions for continuum pore fraction (or porosity) variations. It is not quite clear what the lack of closure for these latter quantities will be on DC poroelastic behaviours. Considering the variety of models and modelling assumptions, it is interesting to compare how these different modelling concepts affect the overall macroscopic response of a poroelastic dual-material. Further, we would like to investigate possible links between the volume fraction based constitutive models and those based on intrinsic material properties.

Answers to structure-property relations, such as those posed above, can be investigated with the aid of micromechanics. Using this framework, Dormieux et al. (2006) derived a fully anisotropic poroelastic dual-continuum model complete with expressions for the constitutive parameters. By starting from the microscale we can see directly how assumptions at this scale manifest in the resulting macroscopic model. It is interesting to compare the constitutive models mentioned earlier in this section to one derived following the rigour of micromechanics.

Finally, the micromechanics framework provides a natural guide for testing the macroscopic poroelastic DC model against microscale equivalents. Work has gone into testing and validating the DC concept for the flow problem (e.g. Lewandowska et al. 2004; Egya et al. 2019). However, little has been done to asses validity of the poroelastically coupled DC approach. In particular it is interest-

ing to study the DC models in light of microscopically induced effects. In this work we consider anisotropy as one such effect in order to keep within the linear framework of (linear) poroelasticity. A natural approach to carry out these tests is to use numerical modelling. This requirement motivates, in part, the numerical framework introduced in this work. Our other motivation is to introduce a framework aligned with the traditional modelling approaches for the flow and deformation subproblems, as well as one equipped to handle the complex grid geometries encountered when modelling the subsurface.

1.4 Contributions and thesis outline

Given the themes described above, our goal of this work is to better understand and represent the links between microscale and macroscale models, within the context of strongly heterogenous porous media, considering poroelastically coupled and uncoupled representations. We address this goal by focusing on three main tasks:

1. Investigate the relations between microscale and dual-continuum poroelastic consitutive models, including previously introduced phenomogelogical models, using micromechanical approaches.

2. Introduce a numerical framework for dual-continuum poroelastic modelling. Use the resulting framework to further study the links between different modelling scales given various modelling and material assumptions made at the microscale.

3. Establish a machine learning-based multiscale modelling approach to improve the accuracy of macroscopic models. Apply the resulting framework to the modelling of inter-continuum mass transfer.

Subsequently, the main contributions of this thesis are:

- Derive a DC poroelastic constitutive model starting from the microscale using homogenisation. Show how previous constitutive models introduced in literature are special cases of the anisotropic one derived here.

- Compare and contrast different DC poroelastic constitutive model formulations introduced previously in literature, as well as assumptions made on these models, using micromechanical arguments and analytical solutions.

- Present a numerical framework for modelling poroelastic dual-continua aligned with traditional approaches for flow and deformation, that is also suitable for the complex grids encountered in the subsurface.

- Using the numerical framework, validate the poroelastic DC model against microscale models for varying degrees of material symmetry. Subsequently, compare and study the impacts of microscale modelling assumptions on macroscopic behaviours.

- Present a machine learning-based framework for multiscale constitutive modelling. In doing, describe the key elements and considerations of the framework.

- Demonstrate the potential of the multiscale modelling approach on the problem of inter-continuum mass transfer in a DC material (without multiphysics behaviours).

We structure this thesis into three parts (Fig. 1.2), aligned with the tasks described above:
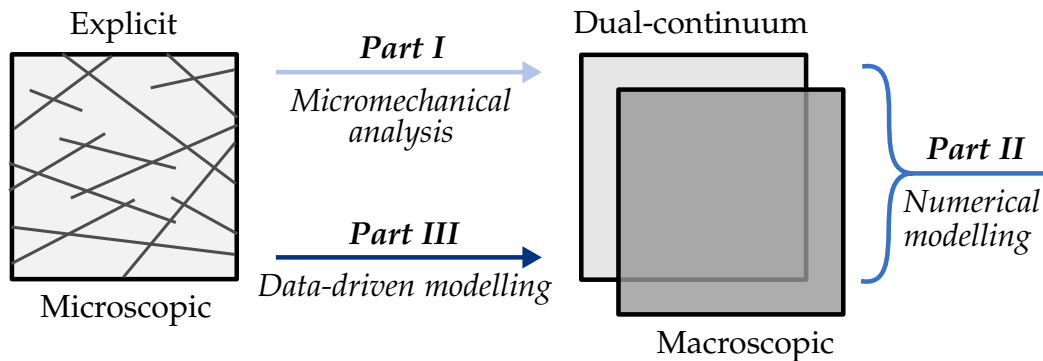
Figure 1.2: Thesis structure.

Part I investigates the link between microscopic and macroscopic poroelastic constitutive models using micromechanical analysis. In Chapter 2, we introduce the macroscopic equations describing dual-continuum materials, starting with the mass and momentum balance equations. Subsequently, we identify quantities needing closure by way of constitutive relations. To provide the poroelastic constitutive model we use a homogenisation approach, introducing the key micromechanical modelling concepts therein. In Chapter 3, we contrast and compare previously introduced poroelastic constitutive models. Further, we investigate previously made decoupling assumptions made on these models. To conduct our analyses of various modelling approaches and decoupling assumptions we use micromechanical perspectives and analytical solutions to a poroelastic model problem. On the basis of these analyses we formulate a set of recommendations for how and when to use various modelling approaches and decoupling assumptions.

Part II involves the numerical modelling of poroelastic dual-continua. Accordingly, in Chapter 4 we introduce a numerical framework suitable for subsurface modelling. Our framework also allows for anisotropic material properties based

on the constitutive model derived in Chapter 2. We demonstrate the framework on a geological grid that includes non-neighbouring connections. In Chapter 5, we use the resulting framework to test the poroelastic dual-continuum approach against a variety of microscale equivalent representations. Our tests vary in complexity, starting with isotropic test cases and progressing to anisotropic test cases. We compare the results between the two modelling scales, studying the effects at the macroscale of modelling and material assumptions made at the microscale.

Part III is dedicated to data-driven multiscale modelling. We introduce the machine learning-based multiscale constitutive modelling framework and details of the key components therein. With the framework in-hand we apply it to the problem of inter-continuum mass transfer in the remainder of Chapter 6. We introduce and compare various machine learning methods used to model the time-dependent transfer behaviour. To follow, we show how we inject the resulting surrogate model into a dual-continuum simulator. Lastly, we compare the resulting hybrid machine learning-physics modelling approach to a microscale model, and to a dual-continuum model using the linear transfer approximation, on several numerical test cases.

Finally, to keep notation brief for the remainder of this thesis, we refer to the low permeability storage continuum as the *matrix* continuum, and the low storage, high permeability transport continuum as the *fracture* continuum. However, the work herein is sufficiently general that other multiscale materials can be considered e.g. soil aggregates.

Part I

Micromechanical analysis

<div style="text-align: right; font-size: 4em; font-weight: bold; color: gray;">2</div>

Mathematical model: From micro to macro

In this chapter, we present the mathematical model for poroelastic dual-continuum materials including the derivation of an appropriate constitutive model through homogenisation. The latter is a novel addition to the literature for which we incorporate anisotropy and intrinsic fracture stiffness properties within the constitutive formulation. In Section 2.1, we start by introducing the representative elementary volume (REV), which serves as the building block for the (macroscopic) continuum approach. In Section 2.2, we give the continuity equations that govern the transport of mass and momentum between elementary volumes. To finish Section 2.2 we provide the constitutive relations necessary for a closed mathematical model. Specifically, we provide closure relations for the (uncoupled) DC flow model, and then highlight the need for the poroelastic constitutive model in the coupled case. To derive the latter we use a micromechanical-based homogenisation approach. Subsequently, in Section 2.3 we go over the key ingredients of the micromechanical approach. Then, in Section 2.4, using concepts introduced Section 2.3, we derive the poroelastic constitutive model. In Section 2.5 we show the relations and conditions linking the dual-continuum and single-continuum constitutive models. Finally, in Section 2.6 we summarise this chapter and provide recommendations for future work. The contents of this chapter are based on work done in Ashworth and Doster (2019b) and Ashworth and Doster (2020).

2.1 The representative elementary volume

In the continuum approach we model transport phenomena (e.g. mass, energy) as continuous processes, despite potential discontinuities at a microscopic scale. Subsequently, we assume infinitesimal volumes (with respect to a macroscopic body size) over which we can replace heterogeneous property fields with hypothetical homogeneous ones (Fig. 2.1). To start, an elementary volume Ω is defined such that effective properties (e.g. porosity) over the domain remain stable given small perturbations in volume size (Bear and Bachmat 1991). At

this point, we refer to the elementary volume as a representative elementary volume (REV) (Bear and Bachmat 1991). More formally, we can define the scale requirements for an REV according to the separation of scales principle (Bear and Bachmat 1991),

$$\ell \ll l \ll L. \tag{2.1}$$

where ℓ, l and L denote the characteristic lengths at the local heterogeneity, REV and macroscopic body scales respectively. Despite the geometrical arguments presented above for the definition of an REV (Fig. 2.1), Eq. (2.1) must also hold for the wavelengths of the physical processes involved (Auriault 2002; Geers et al. 2010). As a result, discontinuous processes such as shocks or localisations preclude the described continuum approach (Kouznetsova et al. 2004). Although the description of an REV presented here is brief, numerous literature exist detailing the finer points of REV definition (e.g. Bear and Bachmat 1991; Ostoja-Starzewski 2006).
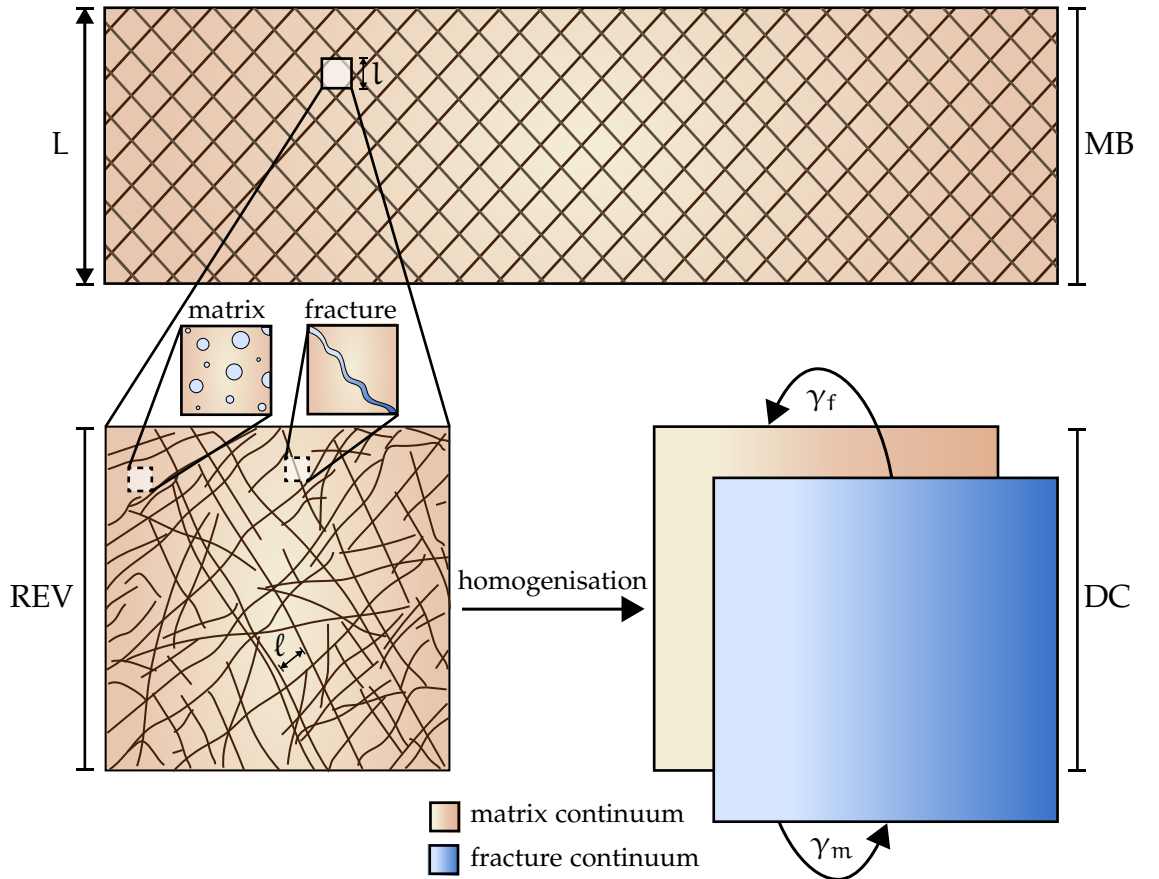
Figure 2.1: Identification of an REV over the microscopic scale from a large macroscopic body (MB). The REV is used to define the macroscopic dual-continuum (DC) model in which matrix (m) and fracture continua (f) are superposed in space and time. Inter-continuum mass exchange is described by the transfer term γ_α [$\alpha = m, f$]. Notations ℓ, l and L denote characteristic lengths of local heterogeneities, the REV and the macroscopic structure respectively.

Lastly, assigning an REV over fractured media is a subject of much debate due to the challenge of establishing criteria for scale separation (Long et al. 1982; Neuman 1988; Min and Jing 2003; Berre et al. 2019). In this thesis, however, we suppose a material for which an REV can be defined, such as densely fractured rock masses (Berkowitz 2002).

2.2 Model equations

In the following, we present the mathematical model for a dual-continuum with and without poroelasticity. As part of the DC approach we assume two-continua which overlap in space and time and communicate through a mass exchange term (Barenblatt et al. 1960). To start we introduce the balance equations that describe the (continuous) variations of mass and momentum within space and time. With respect to deformation, we operate under assumptions of small displacements ($|\mathbf{U}/L| \ll 1$) and infinitesimal transformations ($|\nabla \mathbf{U}| \ll 1$), where $\mathbf{U}$ is the macroscopic displacement vector. As a result, we make no distinction between Eulerian and Lagrangian frames. We then give the constitutive equations necessary to provide a closed mathematical model. First, we provide the constitutive equations for an uncoupled dual-continuum model (flow only). This model will form the basis of the work done in Chapter 6. Second, we identify the quantities in need of closure in the coupled case, addressed in the subsequent sections of this chapter. Lastly, notation for the vector and tensor operations used herein can be found in the corresponding subsection within Notation.

2.2.1 Mass balance

Following Coussy (2004) the balance of mass for a dual-continuum material is given as

$$\frac{\partial m_{l,m}}{\partial t} + \nabla \cdot \mathbf{w}_m = \gamma_m, \tag{2.2}$$

$$\frac{\partial m_{l,f}}{\partial t} + \nabla \cdot \mathbf{w}_f = \gamma_f, \tag{2.3}$$

where $m_{l,\alpha}$ [$\alpha = m, f$], $\mathbf{w}_\alpha$ and γ_α are the fluid mass content, mass flux and inter-continuum mass transfer rate associated with continuum α respectively. The fluid mass content is given by $m_{l,\alpha} = \rho_l \phi_\alpha$, where ρ_l and ϕ_α are the intrinsic fluid density and the Lagrangian porosity for continuum α respectively. The latter is defined as the ratio of the continuum pore volume $|\Omega_\alpha^p|$, to the bulk volume of the undeformed configuration $|\Omega^0|$, where superscript 0 denotes the reference state. Finally, owing to continuity $\gamma_f = -\gamma_m$.

Eqs. (2.2) to (2.3) are the starting blocks for the uncoupled (flow-only) DC model. However, when considering poroelasticity we also need to consider the balance of momentum.

2.2.2 Momentum balance

We present the momentum continuity under quasistatic loadings such that (Coussy 2004),

$$\nabla \cdot \mathbf{\Sigma} + \rho \mathbf{g} = \gamma', \tag{2.4}$$

where $\mathbf{\Sigma}$, ρ and $\mathbf{g}$ are the macroscopic (Cauchy) stress tensor, bulk density of the dual-material and the gravitational acceleration respectively. Notation γ' is a momentum source arising from the inter-continuum mass transfer (Coussy 2004). Accordingly, γ' is given as

$$\gamma' = \sum_{\alpha=m,f} \gamma_\alpha \mathbf{v}_{l,\alpha}, \tag{2.5}$$

where $\mathbf{v}_{l,\alpha}$ is the absolute fluid velocity within each continuum. For the remainder of this thesis, however, we assume $\gamma' \approx 0$, with respect to the other force density terms in Eq. (2.4). Further, we also neglect the effects of gravity $\mathbf{g}$.

2.2.3 Constitutive equations

To close Eqs. (2.2) to (2.4) we require constitutive equations that allow us to express the continuity equations in terms of continuum pressures P_α [$\alpha = m, f$], and when considering poroelasticity, U. In both the uncoupled and coupled case, the intra-continuum mass flux is given according to Darcy's law

$$\mathbf{w}_\alpha = \rho_l \mathbf{q}_\alpha = -\rho_l \frac{\mathbf{K}_\alpha}{\mu_l} \cdot (\nabla P_\alpha - \rho_l \mathbf{g}), \tag{2.6}$$

where $\mathbf{q}_\alpha$ and $\mathbf{K}_\alpha$ are the volume flux vector and macroscopic permeability tensor for continuum α respectively. Notation μ_l is the fluid viscosity. Further, we require a constitutive law for γ_α. Note, despite neglecting the effects of gravity in the remainder, we include it in Darcy's law Eq. (2.6), purely as a means of notational completeness.

For Chapters 3 to 5 we consider a simple linear transfer model of the form (Warren and Root 1963),

$$\gamma_\alpha = \rho_l \frac{\varkappa k'}{\mu_l} (P_\beta - P_\alpha), \tag{2.7}$$

where β denotes a continuum such that $\beta \neq \alpha$. Notation k' denotes the interface permeability, taken here as the intrinsic matrix permeability (Barenblatt et al. 1960; Choo and Borja 2015). Parameter $\varkappa$ is referred to as the shape factor (Warren and Root 1963). As the name suggests, $\varkappa$ encodes the geometrical information of the matrix blocks that interact with the fracture phase. For simplified geometries and boundary conditions $\varkappa$ can be determined analytically. In this work we make use of such simplifying assumptions. Accordingly, for square and cube geometries of isotropic matrix material, we use an analytically derived $\varkappa$ given according to Lim and Aziz (1995),

$$\varkappa = \frac{N_f \pi^2}{\ell^2}, \tag{2.8}$$

where N_f is a dimension parameter related to the number of fracture sets, and ℓ is the characteristic spacing length for the fracture continuum (Fig. 2.1). The first-order nature of Eq. (2.7) is known to oversimplify the physics of inter-continuum mass transfer, particularly at early times (Zimmerman et al. 1993). Rectifying this deficiency is one of the aims in Chapter 6. However, prior to this chapter we acknowledge this simplification with the focus being on multiphysics behaviours. Given expressions for w_α and γ_α, we still require expressions for ρ_l and ϕ_α from $m_{l,\alpha} = \rho_l \phi_\alpha$. For both coupled and uncoupled cases we consider isothermal fluid flow. Consequently, the following fluid compressibility relation holds

$$\frac{1}{K_l} = \frac{1}{\rho_l} \frac{\partial \rho_l}{\partial P_\alpha}, \tag{2.9}$$

where K_l is the fluid bulk modulus. If the fluid is only slightly compressible (high K_l), we only consider small pertubations in ρ_l ($d\rho_l / \rho_l^0 \ll 1$), allowing for the following linearisation

$$\rho_l = \rho_l^0 \left[1 + K_l^{-1} \left(P_\alpha - P_\alpha^0 \right) \right]. \tag{2.10}$$

We note, notation $d\rho_l$ refers to the variation of a quantity, in this case ρ_l, from a reference state ρ_l^0. Under linearity this reference state is taken to be the initial state.

For the remainder of this thesis, unless mentioned otherwise, we assume small perturbations in fluid density, allowing us to use $\rho_l \approx \rho_l^0$ where necessary.

2.2.4 Uncoupled

In the uncoupled case we consider only the mass balance equations Eqs. (2.2) to (2.3). Accordingly, we require a constitutive model for ϕ_α and define the following compressibility relation

$$\frac{1}{K_{\phi,\alpha}} = \frac{1}{\phi_\alpha} \frac{\partial \phi_\alpha}{\partial P_\alpha} \tag{2.11}$$

where $K_{\phi,\alpha}$ is the pore modulus for continuum α. Considering small pertubations in ϕ_α ($d\phi_\alpha/\phi_\alpha^0 \ll 1$) leads to the following linearisation

$$\phi_\alpha = \phi_\alpha^0 \left[1 + K_{\phi,\alpha}^{-1} \left(P_\alpha - P_\alpha^0 \right) \right], \tag{2.12}$$

For the remainder of this thesis, unless mentioned otherwise, we assume small perturbations in porosity, allowing us to use $\phi_\alpha \approx \phi_\alpha^0$ where necessary.

Finally, whilst simple, Eq. (2.12) neglects the potentially significant effect of deformation on pore pressure and vice versa (Zimmerman 2000). However, a good starting point to address this deficiency is the framework of poroelasticity (Biot 1941).

2.2.5 Coupled

In the coupled case we also consider the momentum balance equation Eq. (2.4). Accordingly, we need constitutive equations for $\boldsymbol{\Sigma}$ and for quantities associated with the fluid. For the latter, we first consider variations in the fluid occupied pore space by way of changes in Lagrangian porosity. Then, we extend these formulations to account for variations in fluid mass.

Variation in Lagrangian porosity formulation

Here we provide the relations between $\boldsymbol{\Sigma}$, ϕ_m and ϕ_f in terms of $\mathbf{E}$ (respectively $\mathbf{U}$), P_m and P_f, where $\mathbf{E}$ is the linearised macroscopic strain tensor. The link between these quantities can be verified by the energy approach to poroelasticity. We can show from a purely macroscopic approach (Coussy 2004; Section 4.1, pg. 72), that the increment in strain work density $d\mathcal{W}_s$ on the skeleton due to the strain triplet ($d\mathbf{E}$, $d\phi_m$, $d\phi_f$) can be expressed as

$$d\mathcal{W}_s = \boldsymbol{\Sigma} d\mathbf{E} + P_m d\phi_m + P_f d\phi_f. \tag{2.13}$$

Due to elasticity, our system is non-dissipative and thus the skeletal strain energy is stored entirely as an elastic potential

$$d\mathcal{W}_s = d\mathcal{H}_s, \tag{2.14}$$

where $\mathcal{H}_s$ denotes the Helmholtz free energy of the skeleton, and from which it follows

$$\mathbf{\Sigma} d\mathbf{E} + P_m d\phi_m + P_f d\phi_f - d\mathcal{H}_s = 0. \tag{2.15}$$

Eq. (2.15) is a trivial extension of the skeleton free energy expression for single-porosity materials, and is indeed analogous (and identical) to the expression for the multiphase fluid single-porosity poroelastic problem (e.g. Coussy 2004). Now introducing the following Legendre transform

$$\mathcal{F}_s = \mathcal{H}_s - P_m(\phi_m - \phi_m^0) - P_f(\phi_f - \phi_f^0), \tag{2.16}$$

where $\mathcal{F}_s$ is a potential energy of the skeleton. Substitution of Eq. (2.16) into Eq. (2.15) results in

$$\mathbf{\Sigma} d\mathbf{E} - (\phi_m - \phi_m^0)dP_m - (\phi_f - \phi_f^0)dP_f - d\mathcal{F}_s = 0. \tag{2.17}$$

From Eq. (2.17) we arrive at the following state equations

$$\mathcal{F}_s = \mathcal{F}_s(\mathbf{E}, P_m, P_f): \quad \mathbf{\Sigma} = \frac{\partial \mathcal{F}_s}{\partial \mathbf{E}}; \quad \phi_m - \phi_m^0 = -\frac{\partial \mathcal{F}_s}{\partial P_m}; \quad \phi_f - \phi_f^0 = -\frac{\partial \mathcal{F}_s}{\partial P_f}. \tag{2.18}$$

Applying Eq. (2.18) to Eq. (2.17), and making use of the Maxwell symmetry relations which arise naturally from Eq. (2.18) (Appendix A), leads to

$$d\mathbf{\Sigma} = \mathbb{C}^* : d\mathbf{E} - \mathbf{B}_m dP_m - \mathbf{B}_f dP_f, \tag{2.19}$$

$$d\phi_m = \mathbf{B}_m : d\mathbf{E} + \frac{dP_m}{N_m} + \frac{dP_f}{Q_m}, \tag{2.20}$$

$$d\phi_f = \mathbf{B}_f : d\mathbf{E} + \frac{dP_m}{Q_f} + \frac{dP_f}{N_f}, \tag{2.21}$$

The parameters $\mathbb{C}^*$, $\mathbf{B}_\alpha$, N_α^{-1} and Q_α^{-1} are referred to as tangent properties (Coussy 2004). Parameter $\mathbb{C}^*$ is the (homogenised) stiffness tensor for the dual-medium, whilst $\mathbf{B}_\alpha$, N_α^{-1} and Q_α^{-1} are the effective Biot coefficient, effective Biot modulus and poroelastic cross-coupling modulus for continuum α respectively. Finally, we note that within poroelasticity literature it is common to refer to the quantity $\mathbb{C}^* : \mathbf{E}$ as the effective stress $\mathbf{\Sigma}' = \mathbb{C}^* : \mathbf{E}$ (Bishop 1959; Nur and Byerlee 1971; Borja 2006). We can further simplify Eqs. (2.19) to (2.21) by first invoking integration on the variations, under the assumptions of linearity from reference

conditions. Further, we assume the tangent properties remain constant. Accordingly, given the linearity, our reference state corresponds to the initial state, for which we assume the initial stress, strain and continuum pressures are zero, leading to

$$\boldsymbol{\Sigma} = \mathbb{C}^* : \mathbf{E} - \mathbf{B}_m P_m - \mathbf{B}_f P_f, \tag{2.22}$$

$$d\phi_m = \mathbf{B}_m : \mathbf{E} + \frac{P_m}{N_m} + \frac{P_f}{Q_m}, \tag{2.23}$$

$$d\phi_f = \mathbf{B}_f : \mathbf{E} + \frac{P_m}{Q_f} + \frac{P_f}{N_f}, \tag{2.24}$$

We make the distinction between Eqs. (2.19) to (2.21) and Eqs. (2.22) to (2.24) as for the most part in this thesis, we assume problems for which the reference state is as described in formulating Eqs. (2.22) to (2.24). However, the variation formulation shown in Eqs. (2.19) to (2.21) will be useful for the developments in Chapter 3.

Variation in fluid mass content formulation

An alternative formulation to Eqs. (2.20) to (2.21) (resp. Eqs. (2.23) to (2.24)) involves variations in continuum fluid mass. Accordingly, the definition for the variation in fluid mass content is (Dormieux et al. 2006),

$$dm_{l,\alpha} = \rho_l \phi_\alpha - \rho_l^0 \phi_\alpha^0. \tag{2.25}$$

Using the small perturbation in fluid density assumption introduced in Section 2.3.2 ensures linearity of the constitutive relations. As a result, we express Eq. (2.25) as

$$\frac{dm_{l,\alpha}}{\rho_l^0} = d\phi_\alpha + \phi_\alpha^0 \frac{d\rho_l}{\rho_l^0}. \tag{2.26}$$

Introducing the following notation $\xi_\alpha = m_{l,\alpha}/\rho_l^0$, in which ξ_α denotes the fluid volume content for continuum α, and making use of Eq. (2.10) gives

$$d\xi_\alpha = d\phi_\alpha + \frac{\phi_\alpha^0}{K_l}. \tag{2.27}$$

Finally, substituting Eqs. (2.20) to (2.21) into Eq. (2.27), for each continuum, gives

$$d\xi_m = \mathbf{B}_m : d\mathbf{E} + \frac{dP_m}{M_m} + \frac{dP_f}{Q_m}, \tag{2.28}$$

$$d\xi_f = \mathbf{B}_f : s\mathbf{E} + \frac{dP_m}{Q_f} + \frac{dP_f}{M_f}, \tag{2.29}$$

where

$$\frac{1}{M_\alpha} = \frac{1}{N_\alpha} + \frac{\phi_\alpha^0}{K_l}.$$

(2.30)

Eqs. (2.28) to (2.29) will be useful for the analyses conducted in Chapter 3.

In the remainder of this chapter, we see how the constitutive model in Eqs. (2.22) to (2.24), and expressions for the constitutive parameters in terms of constituent information, can be directly obtained from the microscale. To do so we use homogenisation.

2.3 Micromechanical preliminaries

To start, we present the key ingredients that enable the homogenisation approach used here. In this work we consider homogenisation to refer to methodologies leading to an effective (homogeneous) macroscopic description of a material characterised by a heterogeneous microstructure. Accordingly, we introduce the averaging operation required by the homogenisation procedure used herein. With this operation in-hand, we provide the links between microscopic and macroscopic quantities, introducing important relations that will be used for deriving the constitutive model.

2.3.1 Volume averaging

Typical approaches for averaging include the volume average, moving average and the ensemble average (Beran 1971; Hashin 1983; Bear and Bachmat 1991; Nemat-Nasser and Hori 1993). The first is a spatially independent average taken over a (sub)volume element from a large macroscopic body. The second defines averages taken on a fixed specimen over elementary volumes at different points within the body. The third is a statistical treatment representing the average taken at fixed points across an ensemble of bodies.

To reconcile these different averaging operations we introduce the concept of statistical homogeneity. This assumption states that the statistics describing the distributions of heterogeneities across any number of REVs are spatially invariant (Hashin 1972). Consequently, the volume average and moving average coincide (Nemat-Nasser and Hori 1993). Further, by the definition of an REV in a statistically homogeneous body, averages over the REV itself approach averages taken over the whole body (Hashin 1972). Finally, statistical homogeneity lets us define an ergodic hypothesis between the moving average and the ensemble average. Accordingly, the ensemble average coincides with the ensemble average over the body, or the volume average over an REV (Hashin 1972).

Following the arguments above, in this work we assume statistically homogeneous materials and define the classical volume averaging expression

$$\bar{z} = \frac{1}{|\Omega|} \int_{\Omega} z(\mathbf{x}) \, dV, \tag{2.31}$$

where z is an arbitrary field quantity.

2.3.2 Strain and stress average theorems

In the following, we provide the links between the microscopic linearised strain tensor $\boldsymbol{\epsilon}$ and (Cauchy) stress tensor $\boldsymbol{\sigma}$, and their macroscopic counterparts $\mathbf{E}$ and $\boldsymbol{\Sigma}$ respectively. To do so we make use of the averaging operation described above.

Substituting $\boldsymbol{\epsilon}$ and $\boldsymbol{\sigma}$ into Eq. (2.31) gives

$$\bar{\boldsymbol{\epsilon}} = \frac{1}{|\Omega|} \int_{\Omega} \boldsymbol{\epsilon}(\mathbf{x}) \, dV, \tag{2.32}$$

$$\bar{\boldsymbol{\sigma}} = \frac{1}{|\Omega|} \int_{\Omega} \boldsymbol{\sigma}(\mathbf{x}) \, dV. \tag{2.33}$$

Further, we can express the average quantities shown in Eqs. (2.32) to (2.33) in terms of intrinsic averages. Specifically, these are volume averages considered over one of the constituent domains $\Omega_{\alpha} \subset \Omega$, as oppose to the whole domain Ω. Assuming a perfectly bonded two phase material we write

$$\bar{\boldsymbol{\epsilon}} = v_1 \bar{\boldsymbol{\epsilon}}_1 + v_2 \bar{\boldsymbol{\epsilon}}_2, \tag{2.34}$$

$$\bar{\boldsymbol{\sigma}} = v_1 \bar{\boldsymbol{\sigma}}_1 + v_2 \bar{\boldsymbol{\sigma}}_2, \tag{2.35}$$

where subscripts 1 and 2 are just arbitrary notations for denoting two distinct phases or constituents. Notation v_{α} denotes the volume fraction, given as the ratio of the undeformed constituent volume $|\Omega_{\alpha}^0|$ to $|\Omega^0|$. The intrinsic average of a field is then

$$\bar{z}_{\alpha} = \frac{1}{|\Omega_{\alpha}|} \int_{\Omega_{\alpha}} z(\mathbf{x}) \, dV. \tag{2.36}$$

We now move on to the strain and stress average theorems for which we follow the working of Hashin (1972). Starting with strain, we first note the microscopic strain-displacement compatibility relation

$$\boldsymbol{\epsilon} = \underline{\nabla} \mathbf{u} = \frac{1}{2} \left(\nabla \mathbf{u} + \nabla^{\top} \mathbf{u} \right), \tag{2.37}$$

where $\mathbf{u}$ is the microscopic displacement vector, and $\underline{\nabla}$ denotes the symmetric gradient operator. Then, introducing Eq. (2.37) into Eq. (2.32) followed by application of Gauss's theorem leads to

$$\overline{\boldsymbol{\epsilon}} = \frac{1}{2|\Omega|} \int_{\partial\Omega} (\mathbf{u} \otimes \mathbf{n} + \mathbf{n} \otimes \mathbf{u}) \ dS, \tag{2.38}$$

where $\partial\Omega$ and $\mathbf{n}$ denote the boundary of Ω, and the unit normal surface vector respectively. Next, we introduce the uniform displacement boundary conditions at the boundary of our REV

$$\mathbf{u}(\mathbf{x}) = \mathbf{E} \cdot \mathbf{x} \quad \forall \mathbf{x} \in \partial\Omega. \tag{2.39}$$

Substitution of Eq. (2.39) into Eq. (2.38) leads naturally to the strain average theorem

$$\overline{\boldsymbol{\epsilon}} = \mathbf{E}, \tag{2.40}$$

which holds for any compatible strain fields Eq. (2.37) that obey Eq. (2.39). We can derive a similar relation to Eq. (2.40) for stress. Using the relation

$$\nabla \cdot (\mathbf{x} \otimes \boldsymbol{\sigma}) = \boldsymbol{\sigma}, \tag{2.41}$$

in Eq. (2.33), followed by Gauss's theorem leads to

$$\overline{\boldsymbol{\sigma}} = \frac{1}{|\Omega|} \int_{\Omega} (\mathbf{x} \otimes \boldsymbol{\sigma} \cdot \mathbf{n}) \ dS. \tag{2.42}$$

Next we introduce the uniform stress boundary conditions

$$\boldsymbol{\sigma}(\mathbf{x}) \cdot \mathbf{n}(\mathbf{x}) = \boldsymbol{\Sigma} \cdot \mathbf{n}(\mathbf{x}) \quad \forall \mathbf{x} \in \partial\Omega. \tag{2.43}$$

Substitution of Eq. (2.43) into Eq. (2.42) leads naturally to the stress average theorem

$$\overline{\boldsymbol{\sigma}} = \boldsymbol{\Sigma}, \tag{2.44}$$

which holds for any equilibrated (divergence free) stress fields that obey Eq. (2.43).

It is worth noting that the uniform boundary conditions just described produce statistically homogeneous fields. Specifically, fields whose averages are spatially invariant with respect to an REV. The importance of this statement together with the statistically homogeneous body assumption, is that both conditions ensure reciprocity between effective moduli (Hashin 1972). Accordingly, the homogenised behaviour can be predicted from either of the uniform boundary con-

ditions. Further, both of the aforementioned points imply that averaged fields, such as stress, are approximately equal for both of the homogeneous boundary conditions (Dormieux et al. 2006).

2.3.3 Hill-Mandel condition

The final averaging theorem comes by way of the Hill-Mandel condition (Hill 1963). This condition expresses the strain energy density equivalence between the micro and macroscales. As a result, we need to find the assumptions that allow the following to hold

$$\overline{\sigma : \epsilon} = \overline{\sigma} : \overline{\epsilon}. \tag{2.45}$$

One can show (e.g. Hashin 1972; Nemat-Nasser and Hori 1993) for a compatible strain field corresponding to Eq. (2.39) and using Eq. (2.40)

$$\overline{\sigma : \epsilon} = \overline{\sigma} : E = \overline{\sigma} : \overline{\epsilon}. \tag{2.46}$$

Similarly, for an equilibrated stress field corresponding to Eq. (2.43) and using Eq. (2.44) we obtain

$$\overline{\sigma : \epsilon} = \Sigma : \overline{\epsilon} = \overline{\sigma} : \overline{\epsilon}. \tag{2.47}$$

Thus the Hill-Mandel condition is satisfied for compatible strain fields and equilibrated stress fields using either of the uniform boundary conditions (Zaoui 2002).

2.3.4 Effective properties

The final part of this section concerns the averaging results for the microscopic linear elasticity constitutive relations

$$\sigma = \mathbb{C} : \epsilon, \tag{2.48}$$

$$\epsilon = \mathbb{S} : \sigma, \tag{2.49}$$

where $\mathbb{C}$ and $\mathbb{S}$ denote the microscopic stiffness and compliance tensors respectively. Note, $\mathbb{S} = \mathbb{C}^{-1}$.

Following Dormieux et al. (2006) we consider the following local uniform strain boundary problem

$$\nabla \cdot \sigma = 0 \quad \text{in } \Omega, \tag{2.50}$$

$$\sigma = \mathbb{C}(x) : \epsilon \quad \text{in } \Omega, \tag{2.51}$$

$$\mathbf{u}(\mathbf{x}) = \mathbf{E} \cdot \mathbf{x} \quad \text{on } \partial\Omega, \tag{2.52}$$

where $\boldsymbol{\sigma} = \mathbb{C}(\mathbf{x}) : \boldsymbol{\epsilon} \leftrightarrow \boldsymbol{\epsilon} = \mathbb{S}(\mathbf{x}) : \boldsymbol{\sigma}$.

Owing to the linearity of Eq. (2.50) we can define a linear relation between $\boldsymbol{\epsilon}$ and $\mathbf{E}$

$$\boldsymbol{\epsilon}(\mathbf{x}) = \mathbb{A}(\mathbf{x}) : \mathbf{E}. \tag{2.53}$$

where $\mathbb{A}(\mathbf{x})$ is the fourth-order strain concentration tensor (Hill 1963). The concentration tensor $\mathbb{A}(\mathbf{x})$ represents a mapping between the macroscopic strain tensor $\mathbf{E}$ to its local counterpart $\boldsymbol{\epsilon}(\mathbf{x})$. Due to the linearity of elasticity, $\mathbb{A}(\mathbf{x})$ in fact represents the strain solution to an elasticity problem for which the macroscopic strain components are unit strains (Hashin 1972). As a result, $\mathbb{A}(\mathbf{x})$ is dependent on the geometry and phase moduli at the microscale (Hill 1963).

Combining Eq. (2.53) with Eq. (2.34) whilst using the strain average theorem it can be shown

$$\overline{\boldsymbol{\epsilon}} = \mathbf{E} = v_1 \overline{\mathbb{A}}_1 : \mathbf{E} + v_2 \overline{\mathbb{A}}_2 : \mathbf{E}, \tag{2.54}$$

where $\overline{\mathbb{A}}_\alpha$ denotes the intrinsic average of the strain concentration tensor over constituent α. From Eq. (2.54) we can see

$$\mathbb{I} = \overline{\mathbb{A}} = v_1 \overline{\mathbb{A}}_1 + v_2 \overline{\mathbb{A}}_2 \tag{2.55}$$

where $\mathbb{I}$ is the fourth-order identity tensor. Next, using Eq. (2.53) in Eq. (2.48) and then taking the volume average leads to

$$\boldsymbol{\Sigma} = \overline{\mathbb{C} : \mathbb{A} : \mathbf{E}} = \mathbb{C}^* : \mathbf{E}, \tag{2.56}$$

where

$$\mathbb{C}^* = \overline{\mathbb{C} : \mathbb{A}}, \tag{2.57}$$

denotes the homogenised (or effective) stiffness tensor. Note, we adopt the definition $\boldsymbol{\Sigma} = \overline{\boldsymbol{\sigma}}$ within the framework of uniform strain boundary conditions owing to the statistical homogeneity assumptions described previously. Eq. (2.56) then represents the macroscopic linear stress-strain constitutive relation for a hypothetically homogeneous material arising after homogenisation of a heterogeneous microstructure.

We can express $\mathbb{C}^*$ in terms of constituent stiffnesses $\mathbb{C}_1$ and $\mathbb{C}_2$. From Eq. (2.55) and the definition in Eq. (2.57), it can be shown that (Hashin 1972),

$$\mathbb{C}^* = v_1 \overline{\mathbb{A}}_1 : \mathbb{C}_1 + v_2 \overline{\mathbb{A}}_2 : \mathbb{C}_2. \tag{2.58}$$

Next, comparison of Eq. (2.54) with Eq. (2.34) yields the following relations

$$\overline{\epsilon}_1 = \overline{\mathbb{A}}_1 : \mathbf{E}, \quad \overline{\epsilon}_2 = \overline{\mathbb{A}}_2 : \mathbf{E}. \tag{2.59}$$

In situations where experimental determination for the entries of $\mathbb{C}^*$ are prohibitive, we seek alternative approaches. Accordingly, from Eq. (2.58), if we can calculate either $\overline{\mathbb{A}}_1$ or $\overline{\mathbb{A}}_2$, provided we know the phase moduli, we can calculate $\mathbb{C}^*$. However, determination of $\overline{\mathbb{A}}_\alpha$ is nontrivial owing to the often complex nature of the microstructure. Instead $\overline{\mathbb{A}}_\alpha$ can be approximated, which is the goal of analytical techniques such as the self-consistent scheme and Mori-Tanaka method mentioned in Section 1.2. Alternatively, one could approach the determination of $\overline{\mathbb{A}}_\alpha$ numerically (e.g. Brassart et al. 2010). However, in this context, the standard approach with numerical approaches is to setup virtual experiments to calculate directly $\mathbb{C}^*$ (e.g. using computational homogenisation), as oppose to calculating $\overline{\mathbb{A}}_\alpha$.

We can derive similar relations to Eqs. (2.53) to (2.59) following averaging of Eq. (2.49). To do so, we consider a boundary value problem as per Eqs. (2.50) to (2.52) where instead we use the uniform stress boundary conditions Eq. (2.43) in place of the uniform displacement boundary conditions in Eq. (2.52). Again, due to linearity, we define the following mapping between σ and Σ

$$\sigma(\mathbf{x}) = \mathbb{B}(\mathbf{x}) : \Sigma. \tag{2.60}$$

where $\mathbb{B}(\mathbf{x})$ is the fourth-order stress concentration tensor (Hill 1963). Combining Eq. (2.60) with Eq. (2.35) whilst using the stress average theorem it can be shown

$$\overline{\sigma} = \Sigma = v_1 \overline{\mathbb{B}}_1 : \Sigma + v_2 \overline{\mathbb{B}}_2 : \Sigma. \tag{2.61}$$

where $\overline{\mathbb{B}}_\alpha$ denotes the intrinsic average of the stress concentration tensor over constituent α. Using Eq. (2.60) in Eq. (2.49) and then taking the volume average leads to

$$\mathbf{E} = \overline{\mathbb{S} : \mathbb{B} : \Sigma} = \mathbb{S}^* : \Sigma, \tag{2.62}$$

where

$$\mathbb{S}^* = \overline{\mathbb{S} : \mathbb{B}}, \tag{2.63}$$

denotes the homogenised compliance tensor. Due to the statistical homogeneity assumptions described previously in Section 2.3, $\mathbb{S}^* \approx (\mathbb{C}^*)^{-1}$. Finally, we can

show an analogous expression to Eq. (2.58) for S^* by using Eq. (2.55) and the definition in Eq. (2.63)

$$S^* = v_1 \overline{\mathbb{B}}_1 : S_1 + v_2 \overline{\mathbb{B}}_2 : S_2. \tag{2.64}$$

Lastly, in analogy to Eq. (2.59) we define the following

$$\overline{\sigma}_1 = \overline{\mathbb{B}}_1 : \Sigma, \quad \overline{\sigma}_2 = \overline{\mathbb{B}}_2 : \Sigma. \tag{2.65}$$

2.4 Homogenisation for a dual-continuum

In the final part of this chapter, we develop the DC poroelastic constitutive model. To start, we introduce the underlying modelling assumptions, whilst considering the material symmetry and mechanical properties of the constituents in the process. With respect to the latter, previous DC poroelastic models have, for the most part, assumed isotropy of the continua and bulk material (Berryman and Wang 1995; Khalili and Valliappan 1996; Loret and Rizzi 1999; Choo and Borja 2015). However, rock formations are well known to exhibit anisotropic properties (Snow 1969; Price and Cosgrove 1990; Babuska and Cara 1991). Recent work by Zhang et al. (2019) showed that anistotropic permeabilities can have measurable impacts on the flow-patterns in poroelastic dual-continuum materials. Further to anisotropy, and in the case of fractured materials, the fractures themselves can have intrinsic mechanical properties owing to local asperities and/or bridging material between fracture faces (Olsson and Barton 2001; Lemarchand et al. 2009; Jaeger et al. 2009). Intrinsic mechanical properties of both continua have been considered for isotropic materials in the works of Elsworth and Bai (1992), Berryman (2002), Berryman and Pride (2002) and Nguyen and Abousleiman (2010). Further, despite works such as Olsson and Barton (2001) and Jaeger et al. (2009) considering the nonlinearity of fracture deformation, incorporating such effects within a continuum framework is nontrivial. The starting point considered within this work, is therefore to consider fracture deformation under infinitesimal deformations at the microscale. Indeed this is the modelling assumption made by previously introduced dual-continuum poroelastic constitutive models. Such an assumption could be valid within fractures containing a significant portion of stiff infill material.

To derive the constitutive relations, we add to a micromechanically derived anisotropic constitutive model by Dormieux et al. (2006). Contrary to the model by Dormieux et al. (2006) (Section 5.6, pg. 161), we incorporate linear (poro)elastic properties for the fracture continuum at the microscale. In this case *both* the matrix and the fracture continua are considered to have intrinsic stiffness properties.

Following homogenisation, the resulting model, complete with expressions for the effective parameters, is an anisotropic, dual-stiffness constitutive model.

2.4.1   Microscale problem definition

To extend the homogenisation problem introduced by Dormieux et al. (2006) we consider the domain Ω over an REV in which there exists a porous matrix $\Omega_m \subset \Omega$, and porous fracture domain $\Omega_f \subset \Omega$. Accordingly, each domain represents a continuum at the microscale. We assume linear poroelasticity for each continuum domain (Biot 1941, Coussy 2004), and that the continua are saturated by the same slightly compressible fluid. Further, following Section 2.2 we assume isothermal evolutions and zero initial stress and pressure conditions.

An important assumption is that we consider microscopic fluctuations in pressures are negligible with respect to the macroscopic continuum pressures (Dormieux et al. 2006). As a result, fluids are assumed to be in steady-state, but at different equilibrium pressures, within the respective domains in the REV. Consequently, we model solid-fluid interactions at the microscale using uniform continuum pressures (Van den Eijnden et al. 2016). In situations when hydrostatic equilibrium within each phase is not fulfilled, one could expect the aforementioned microscale pressure assumption to lead to measurable inaccuracies at the macroscale. An example of one such situation would be for the case of highly compressible fluids. We explore the impacts of this microscale pressure assumption in further detail in Chapter 5. As is customary we take stress and strain as positive in the tensile direction. Finally, to ease notation in the forthcoming derivation, we consider reference states to coincide with natural initial states. Accordingly, the initial micro and macro stresses, strains and pressures are zero. However, extensions to the derivation herein to include prestressed states can be made following the working of Dormieux et al. (2006) (Section 5.5, pg. 160).

With the given assumptions, the local constitutive model for a microscopic continuum α is then

$$\boldsymbol{\sigma}_\alpha = \mathbb{C}_\alpha : \boldsymbol{\epsilon}_\alpha - \mathbf{b}_\alpha P_\alpha \quad \text{in } \Omega_\alpha, \tag{2.66}$$

$$d\varphi_\alpha = \mathbf{b}_\alpha : \boldsymbol{\epsilon}_\alpha + \frac{P_\alpha}{n_\alpha} \quad \text{in } \Omega_\alpha. \tag{2.67}$$

where $\mathbb{C}_\alpha$ $[\alpha = m, f]$ is the intrinsic fourth-order stiffness tensor for continuum α, and the second-order tensors, $\boldsymbol{\sigma}_\alpha$, $\boldsymbol{\epsilon}_\alpha$, $\mathbf{b}_\alpha$, are the microscopic Cauchy stress and linearised strain tensors, and intrinsic Biot coefficient for continuum α respectively. Parameter n_α is the microscopic Biot modulus, and $d\varphi_\alpha = \varphi_\alpha - \varphi_\alpha^0$ is the evolution of the local Lagrangian porosity from the reference state, all written in terms of continuum α. The local Lagrangian porosity is the ratio of the

continuum pore volume $|\Omega_\alpha^p|$, to the bulk volume of the undeformed continuum configuration $|\Omega_\alpha^0|$. Accordingly, the relation between the micro and macroscopic continuum Lagrangian porosities is given as

$$\phi_\alpha = \nu_\alpha \varphi_\alpha. \tag{2.68}$$

The intrinsic Biot coefficient and Biot modulus in Eqs. (2.66) to (2.67) are given as

$$\mathbf{b}_\alpha = \mathbf{1} - \mathbb{C}_\alpha : (\mathbb{C}_\alpha^s)^{-1} : \mathbf{1}, \tag{2.69}$$

$$\frac{1}{n_\alpha} = \left(\mathbf{b}_\alpha - \varphi_\alpha^0 \mathbf{1} \right) : (\mathbb{C}_\alpha^s)^{-1} : \mathbf{1}, \tag{2.70}$$

where $\mathbb{C}_\alpha^s$ is the fourth-order stiffness tensor related to the solid material in continuum α.

It is useful to re-write Eqs. (2.66) to (2.67) in a unified way as follows (Dormieux et al. 2006),

$$\boldsymbol{\sigma}(\mathbf{x}) = \mathbb{C}(\mathbf{x}) : \boldsymbol{\epsilon}(\mathbf{x}) + \boldsymbol{\sigma}^p(\mathbf{x}) \quad \forall \mathbf{x} \in \Omega, \tag{2.71}$$

where $\mathbb{C}(\mathbf{x})$, and the prestress tensor distribution related to the fluid pressure $\boldsymbol{\sigma}^p(\mathbf{x})$ (Chateau and Dormieux 2002), are given by

$$\mathbb{C}(\mathbf{x}) = \begin{cases} \mathbb{C}_m & \text{in } \Omega_m \\ \mathbb{C}_f & \text{in } \Omega_f \end{cases}, \tag{2.72}$$

$$\boldsymbol{\sigma}^p(\mathbf{x}) = \begin{cases} -\mathbf{b}_m P_m & \text{in } \Omega_m \\ -\mathbf{b}_f P_f & \text{in } \Omega_f \end{cases}, \tag{2.73}$$

respectively.

The essence of the homogenisation approach is to define a boundary value problem on the REV, the solution to which allows for the determination of macroscopic constitutive properties. Accordingly, the momentum balance boundary value problem is defined as

$$\nabla \cdot \boldsymbol{\sigma} = 0 \quad \text{in } \Omega, \tag{2.74}$$

$$\boldsymbol{\sigma} = \mathbb{C}(\mathbf{x}) : \boldsymbol{\epsilon} + \boldsymbol{\sigma}^p(\mathbf{x}) \quad \text{in } \Omega, \tag{2.75}$$

$$\hat{\mathbf{u}} = \mathbf{E} \cdot \mathbf{x} \quad \text{on } \partial\Omega, \tag{2.76}$$

where quantities denoted by ˆ are boundary assigned values i.e. $u(x) = \hat{u}$ on $\partial\Omega$. With the definition of the microscopic boundary value problem and the underlying modelling assumptions we now proceed to homogenisation.

2.4.2 Recovery of the constitutive system

From the superposition property in linear systems, Eqs. (2.74) to (2.76) can be decomposed into two subproblems. Subproblem I can be interpreted as a drained poroelastic problem:

$$\nabla \cdot \sigma^I = 0 \quad \text{in } \Omega, \tag{2.77}$$

$$\sigma^I = \mathbb{C}(x) : \epsilon^I \quad \text{in } \Omega, \tag{2.78}$$

$$\hat{u}^I = E \cdot x \quad \text{on } \partial\Omega, \tag{2.79}$$

$$\text{with} \quad \Sigma^I = \overline{\sigma}^I = \mathbb{C}^* : E \tag{2.80}$$

where we have used the results and assumptions from Section 2.3 in defining Eq. (2.80). Subproblem II defines a constrained material ($E = 0$) subject to loading via the prestress field σ^p:

$$\nabla \cdot \sigma^{II} = 0 \quad \text{in } \Omega, \tag{2.81}$$

$$\sigma^{II} = \mathbb{C}(x) : \epsilon^{II} + \sigma^p(x) \quad \text{in } \Omega, \tag{2.82}$$

$$\hat{u}^{II} = 0 \quad \text{on } \partial\Omega, \tag{2.83}$$

$$\text{with} \quad \Sigma^{II} = \overline{\sigma}^{II} = \overline{\mathbb{C}(x) : \epsilon^{II}} + \overline{\sigma^p(x)} \tag{2.84}$$

In fact, we can show Eq. (2.84) is equivalent to

$$\Sigma^{II} = \Sigma^p = \overline{\sigma^p : \mathbb{A}}, \tag{2.85}$$

Following Dormieux et al. (2006), by considering the Hill-Mandel condition for the stress field σ^{II} and strain field ϵ^I

$$\overline{\sigma^{II} : \epsilon^I} = \Sigma^{II} : E. \tag{2.86}$$

Rewriting the left-hand side of Eq. (2.86) following the definition for σ^{II} in Eq. (2.82)

$$\overline{\sigma^{II} : \epsilon^I} = \overline{\epsilon^{II} : \mathbb{C}(x) : \epsilon^I} + \overline{\sigma^p : \epsilon^I}. \tag{2.87}$$

Applying the Hill-Mandel condition to the first term on the right-hand side of Eq. (2.88), whilst noting $\overline{\epsilon}^{II} = 0$ due to Eq. (2.83) leaves

$$\overline{\sigma^{II} : \epsilon^{I}} = \overline{\sigma^{p} : \epsilon^{I}}. \tag{2.88}$$

Finally, from Eq. (2.86), and with Eq. (2.53) in Eq. (2.88), we obtain the relation shown in Eq. (2.85).

Eq. (2.85) is a part of a classical result in micromechanics referred to as Levin's theorem (Levin 1967). That is, the macroscopic constitutive equation follows the form of the linear local constitutive relation Eq. (2.66),

$$\Sigma = \Sigma^{I} + \Sigma^{II} = \mathbb{C}^{*} : E + \Sigma^{p}, \tag{2.89}$$

where we make use of the linearity of the problem to superpose subproblems I and II. Owing to the definition of $\mathbb{C}(x)$, and from Eq. (2.58) together with Eq. (2.55), the homogenised stiffness tensor of the composite dual-material is defined as

$$\mathbb{C}^{*} = v_m \overline{\mathbb{A}}_m : \mathbb{C}_m + (\mathbb{I} - v_m \overline{\mathbb{A}}_m) : \mathbb{C}_f, \tag{2.90}$$

where subscripts 1 and 2 in Eq. (2.58) have been replaced with m and f respectively. Similarly, the homogenised prestress tensor is given as

$$\Sigma^{p} = -v_m \overline{\mathbb{A}}_m : \mathbf{b}_m P_m - (\mathbb{I} - v_m \overline{\mathbb{A}}_m) : \mathbf{b}_f P_f. \tag{2.91}$$

Intuitively, Eq. (2.91) can be interpreted as a weighted sum of the continuum pressures. In the work of Borja and Koliji (2009), the authors derive a pore fraction weighting formulation that is thermodynamically consistent. Such an approach was also proposed in Coussy (2004). Given the thermodynamic consistency, it would be interesting to see how one could recover a pore fraction weighted formulation within the general framework of micromechanics.

To proceed, using Eq. (2.91), and with the result from Eq. (2.90), we can identify the first of the macroscopic constitutive parameters, that is the effective Biot coefficients

$$\mathbf{B}_m = \left[(\mathbb{C}^{*} - \mathbb{C}_f) : (\mathbb{C}_m - \mathbb{C}_f)^{-1} \right] : \mathbf{b}_m, \tag{2.92}$$

$$\mathbf{B}_f = \mathbf{b}_f : \mathbb{I} - \left[(\mathbb{C}^{*} - \mathbb{C}_f) : (\mathbb{C}_m - \mathbb{C}_f)^{-1} \right] : \mathbf{b}_f. \tag{2.93}$$

From Section 2.2.5 we showed the dual-continuum model requires state equations for the evolutions of macroscopic Lagragian porosity. Accordingly, for subproblem I

$$d\phi_\alpha^I = v_\alpha \overline{d\varphi}_\alpha = v_\alpha \overline{A}_\alpha : b_\alpha : E$$
$$= B_\alpha : E. \tag{2.94}$$

where we have used Eq. (2.67) in defining Eq. (2.94).

Given subproblem II we have

$$d\phi_m^{II} = v_m b_m : \overline{\epsilon}_m^{II} + \frac{v_m}{n_m} P_m, \tag{2.95}$$

$$d\phi_f^{II} = -v_m b_f : \overline{\epsilon}_m^{II} + \frac{v_f}{n_f} P_f, \tag{2.96}$$

where we have used Eq. (2.34) together with $\overline{\epsilon}^{II} = 0$ to eliminate $v_f \overline{\epsilon}_f$. To advance, we must substitute for $v_m \overline{\epsilon}_m^{II}$. Following Dormieux et al. (2006), $v_m \overline{\epsilon}_m^{II}$ can be expressed as

$$v_m \overline{\epsilon}_m^{II} = (\mathbb{C}_m - \mathbb{C}_f)^{-1} : [(v_m b_m - B_m) P_m + (v_f b_f - B_f) P_f]. \tag{2.97}$$

With Eq. (2.97) in Eqs. (2.95) to (2.96) we recover

$$d\phi_m^{II} = \frac{P_m}{N_m} + \frac{P_f}{Q_m}, \tag{2.98}$$

$$d\phi_f^{II} = \frac{P_m}{Q_f} + \frac{P_f}{N_f}, \tag{2.99}$$

where the effective constitutive parameters N_α^{-1} and Q_α^{-1} are defined as

$$\frac{1}{N_m} = \left[(v_m b_m - B_m) : (\mathbb{C}_m - \mathbb{C}_f)^{-1} \right] : b_m + \frac{v_m}{n_m}, \tag{2.100}$$

$$\frac{1}{Q_m} = \left[(v_f b_f - B_f) : (\mathbb{C}_m - \mathbb{C}_f)^{-1} \right] : b_m, \tag{2.101}$$

$$\frac{1}{N_f} = \left[(B_f - v_f b_f) : (\mathbb{C}_m - \mathbb{C}_f)^{-1} \right] : b_f + \frac{v_f}{n_f}, \tag{2.102}$$

$$\frac{1}{Q_f} = \left[(B_m - v_m b_m) : (\mathbb{C}_m - \mathbb{C}_f)^{-1} \right] : b_f. \tag{2.103}$$

Provided the storage and transport continua are isotropic, $Q^{-1} = Q_m^{-1} = Q_f^{-1}$ since $b_\alpha[\alpha = m, f] = b_\alpha 1$ where 1 is the second-order identity tensor (Dormieux et al. 2006).

Through superposition of subproblems I and II for the macroscopic variables Σ and $d\phi_\alpha$, we finally recover the anisotropic, dual-stiffness constitutive model for the poroelastic dual-material as given in Eqs. (2.22) to (2.24). Subsequently,

expressions for the effective constitutive parameters $\mathbb{C}^*$, $\mathbf{B}_m$, $\mathbf{B}_f$, N_m^{-1}, Q_m^{-1}, N_f^{-1}, and Q_f^{-1} are given by Eq. (2.82), Eqs. (2.92) to (2.93), and Eqs. (2.100) to (2.103) respectively.

2.5 Relation to the single-porosity constitutive model

In this section we provide the link between the constitutive model derived herein and the well-known single-porosity poroelastic constitutive model (Biot 1941; Coussy 2004).

Under long-term drainage $P = P_m = P_f$. We therefore anticipate dual-continuum models to reduce to single-continuum equivalents under certain assumptions of the moduli involved, for the long-term drainage case. To enable this contraction, we require the following compatibility relations:

$$\mathbf{B} = \mathbf{1} - \mathbb{C}^* : \mathbb{C}_s^{-1} : \mathbf{1} = \mathbf{B}_m + \mathbf{B}_f, \tag{2.104}$$

$$\frac{1}{N} = (\mathbf{B} - \phi\mathbf{1}) : \mathbb{C}_s^{-1} : \mathbf{1} = \frac{1}{N_m} + \frac{1}{N_f} + \frac{1}{Q_m} + \frac{1}{Q_f}, \tag{2.105}$$

where $\mathbb{C}_s$ is the homogeneous solid-grain stiffness tensor and $\phi = \phi_m + \phi_f$. From, Eqs. (2.92) to (2.93) and Eqs. (2.99) to (2.103), Eqs. (2.104) to (2.105) hold provided $\mathbb{C}_s = \mathbb{C}_m^s = \mathbb{C}_f^s$. Accordingly, applying the long-term drainage condition, and contracting Eqs. (2.22) to (2.24) we recover the single-porosity constitutive model originally proposed in Biot (1941), albeit for anisotropic materials. If the equality between solid stiffnesses does not hold, then under long-term drainage, the contracted DC model does not reduce to the conventional single-porosity constitutive model as we know it. However, as an alternative to the long-term drainage condition and solid stiffnesses assumption, we can achieve the contraction to the single-porosity model by setting $\nu_f = 0$. Accordingly, $\mathbb{C}_f = \mathbb{C}_f^s = 0$, $\mathbb{C}^* = \mathbb{C}_m$, and $\mathbb{C}_s = \mathbb{C}_m^s$.

Similar to this current section, in the next chapter we show how previously introduced DC constitutive models, and expressions for the effective parameters therein, can be obtained from the model just derived under certain material assumptions.

2.6 Discussion

This chapter presented the system of equations necessary for uncoupled (flow only) and poroelastically coupled dual-continua. With regards to the latter, we used a micromechanics approach to derive the poroelastic constitutive model. In doing, we highlighted the various assumptions at the microscale that enable the homogenisation approach herein. Further, by starting at the microscale we can

directly see how effective constitutive parameters are related to intrinsic constituent parameters. In the next chapter we see how several previously introduced DC poroelastic constitutive models are related to the one derived in this chapter.

Going beyond the work in this chapter, and this thesis more generally, we identify several challenges related to several simplifying assumptions with regards to the fracture material. First, at the microscale we have treated the fracture morphology as a poroelastic continuum. However, a key challenge is how to map individual fracture measurements to continuum properties. This challenge is not unique to this work and is one faced by the subsurface community more generally (Berkowitz 2002). In the context of this challenge, a micromechanical framework could provide useful insights into experimental and theoretical methodologies for mapping such quantities (e.g. Lemarchand et al. 2009).

Second, we considered linear deformations at the microscale through infinitesimal strain theory. Such an assumption could be valid under the influence of significant amounts of stiff infill or bridging material. However, in general, fractures (and soil aggregate) are well known to deform in a geometrically nonlinear (and irreversible) fashion at the microscale (Bemer et al. 2001; Deude et al. 2002; Bidgoli et al. 2013; Borja and Choo 2016). As a result, we expect nonlinearities at the microscale to have measurable impacts at the macroscale due to material nonlinearities. An example of the latter, is the well known phenomena of stress-dependent permeability. Whilst a first step toward understanding phenomena such as stress-dependent permeability could be achieved within a linear framework, such an approach would be limited in high cost applications where the need for greater accuracy is important (Min et al. 2004). However, developing nonlinear macroscopic constitutive models is nontrivial using experimental and analytical approaches. We thus envisage that useful progress could be made by using the model derived here, within a comprehensive computational multiscale setting. In this case, we would model with infinitesimal deformation at the macroscale, but finite strain at the microscale. The latter would then lead to material nonlinearities at the macroscale. Information passing between scales then needs to be addressed within the computational framework. Such multiscale frameworks within the context of dual-continuum materials have been investigated in Wang and Sun (2018, 2019). However, in these works the authors make use of a volume fraction based formulation to the dual-continuum constitutive model (Borja and Koliji 2009). In the following chapter, we investigate differences between volume fraction based constitutive formulations and those based on intrinsic mechanical properties such as derived here.

Despite the assumptions above, we anticipate the poroelastic model derived in this chapter to be a good starting point for modelling contexts where an REV approach could be justified. A good example of the latter would be dense

fracture corridors. We suggest this model as a starting point for such cases due to its relative simplicity in comparison to more detailed, explicit fracture models. Accordingly, we can gain a useful qualitative understanding in to the complex behaviours of coupled flow and deformation phenomena before adding more physics. Lastly, the micromechanical framework used to obtain the model serves as a reference to understanding the otherwise implicit assumptions made on previously introduced phenomenological constitutive models.

3

Poroelastic constitutive model formulations and their impacts

In this chapter we investigate the relationships between, and assumptions on, previous models presented in literature, as well as the impacts of their use on a poroelastic model problem. In Section 3.1, we provide the contextual motivation behind the investigations carried out in this chapter. Subsequently, in Section 3.2 we introduce and review the various models presented previously in literature. In doing, we highlight decoupling assumptions that have been made by previous users of these models. In Section 3.3, we link the different DC poroelastic constitutive models described in Section 3.2 to the one derived in the previous chapter. In Section 3.4, we study the various decoupling assumptions, investigating their impacts and links to well established micromechanical results. In Section 3.5, we conduct a series of qualitative experiments using a poroelastic model problem to further asses the impacts of the different modelling concepts and decoupling assumptions. In Section 3.6, we present the subsequent results and discussion for these tests. Lastly, in Section 3.7 we offer conclusions and recommendations for model use. The contents of this chapter are based on work done mainly in Ashworth and Doster (2019b) and partly in Ashworth and Doster (2020).

3.1 Background

Following on from Chapter 1, we highlighted several works in which poroelastic cross coupling between the two continua was implicitly neglected. As a result, we term these models as *implicitly decoupled*. However, several 'fully coupled' phenomenological models, namely those coming from Berryman and Wang (1995), Khalili and Valliappan (1996), Berryman (2002) and Berryman and Pride (2002) have since rectified these coupling deficiencies. The differences between these fully coupled models come from the information used to calculate their constitutive parameters. We refer to the expressions used for effective parameter calculations as *coefficient models*.

More recent users of the constitutive/coefficient models introduced by Berryman 2002 (resp. Berryman and Pride 2002), have *explicitly decoupled* pore domain pressures when expressing the constitutive relations in terms of stress and continuum pressures (pure stiffness setting) (Nguyen and Abousleiman 2010; Kim et al. 2012; Mehrabian and Abousleiman 2014; Mehrabian 2018). In these works, the decoupling has been done as a form of non-algebraic closure. Additionally, these decouplings provide explicit relations between effective and constituent properties resulting in simplified coefficient models. However, such assumptions have been made without discussing the origin and sensitivities that may arise as a result.

The constitutive/coefficient models introduced above are based on constituent mechanical property information. However, Borja and Koliji (2009) derive coefficient models based on very different information. Instead, the authors define effective parameters in terms pore fractions coming from their constitutive relation for macroscopic effective stress. Further, Borja and Koliji (2009) identify the constitutive requirement for variations in pore fraction through an energy conjugacy with pressure. However, the authors do not provide explicit relations for this property. Instead, later users of this model (Choo and Borja 2015; Choo et al. 2016; Zhang et al. 2019), assume a non-algebraic closure condition for the pore fraction variations. Given the differences in formulation it is interesting to understand how this model may relate to the mechanical property based coefficient models.

In the remainder of this chapter we explore in further detail the various constitutive modelling concepts, decoupling assumptions in light of micromechanical results, and the resulting impacts of modelling differences.

3.2 Poroelastic dual-continuum constitutive models from literature

In the following we compare three modelling concepts that make use of different properties for the calculation of the constitutive parameters:

1. Khalili and Valliappan (1996) - Constituent mechanical properties, assuming the high permeability, low storage continuum is all void space (no intrinsic fracture properties),

2. Borja and Koliji (2009) - Constituent pore fractions, assuming the high permeability, low storage continuum is all void space,

3. Berryman (2002) - Constituent mechanical properties, including intrinsic fracture properties.

We recognise these models, to the best of our ability, as the most dominant within the literature. They have been used in the works of Khalili et al. (2000),

Callari and Federico (2000), Pao and Lewis (2002), Fornells et al. (2007), Taron et al. (2009), Kim et al. (2012), Mehrabian and Abousleiman (2014), Choo and Borja (2015),Choo et al. (2016), Wang and Sun (2018) and Zhang et al. (2019). It should be stressed that in most cases the modelling concepts introduced in this section build on, or are aligned with, previous works and concepts introduced by Aifantis (1977, 1979); Wilson and Aifantis (1982); Elsworth and Bai (1992); Berryman and Wang (1995); Tuncay and Corapcioglu (1995, 1996); Loret and Rizzi (1999); Dormieux et al. (2006) to name but a few. These works should thus be borne in mind in the remainder of this section.

3.2.1 Preliminaries

In the following, we give relations that will be useful for the analyses in this chapter given the isotropy of the constituent and bulk materials assumed in the models to follow. Accordingly, tensorial quantities within the constitutive equations are given in terms of their scalar invariants. As a result, we introduce the mean stress Σ and volumetric strain E as

$$\Sigma = \frac{1}{3}\mathrm{tr}(\boldsymbol{\Sigma}), \tag{3.1}$$

$$E = \mathrm{tr}(\mathbf{E}). \tag{3.2}$$

Further, mappings for the second order and fourth order (poro)elastic tensors to their scalar equivalents are given as

$$K = \frac{1}{d^2}\mathbf{1} : \mathbf{C} : \mathbf{1}, \tag{3.3}$$

$$B = \frac{1}{d}\mathbf{B} : \mathbf{1}, \tag{3.4}$$

where we drop subscripts and superscripts to highlight the generality of the mappings. Notation d denotes the spatial dimension i.e. $d = 2$ or 3. Based on the relations and mappings in Eqs. (3.1) to (3.4) we give Eqs. (2.19) to (2.21) in terms of their scalar invariants such that

$$d\Sigma = K^* dE - B_m dP_m - B_f dP_f, \tag{3.5}$$

$$d\phi_m = B_m dE + \frac{dP_m}{N_m} + \frac{dP_f}{Q_m}, \tag{3.6}$$

$$d\phi_f = B_f dE + \frac{dP_m}{Q_f} + \frac{dP_f}{N_f}. \tag{3.7}$$

Analogously, Eqs. (2.28) to (2.29) are given as

$$d\xi_m = B_m dE + \frac{dP_m}{M_m} + \frac{dP_f}{Q_m}, \tag{3.8}$$

$$d\xi_f = B_f dE + \frac{dP_m}{Q_f} + \frac{dP_f}{M_f}. \tag{3.9}$$

Note, in Eqs. (3.5) to (3.9), we make use of the variation formulation for the constitutive system. We do this to aid in the analyses conducted later in this chapter.

Next, we give the isotropic equivalent relation to Eq. (2.90), doing the same also for the homogenised isotropic compliance, such that

$$K^* = K_m + v_f(K_f + K_m)\overline{A}_f, \tag{3.10}$$

$$S^* = S_m + v_f(S_f + S_m)\overline{B}_f, \tag{3.11}$$

where we have replaced v_m in favour of v_f in the current formulations compared to Eq. (2.90). Notations $\overline{A}_\alpha$ and $\overline{B}_\alpha$ are the scalar equivalents to the intrinsically averaged concentration tensors introduced in Eq. (2.59) and Eq. (2.65) respectively. These scalar concentration factors thus provide mappings between the macroscopic volumetric strain and mean stress to their intrinsicly averaged counterparts respectively. Accordingly,

$$\overline{\epsilon}_m = \overline{A}_m E, \quad \overline{\epsilon}_f = \overline{A}_f E, \tag{3.12}$$

$$\overline{\sigma}_m = \overline{B}_m \Sigma, \quad \overline{\sigma}_f = \overline{B}_f \Sigma. \tag{3.13}$$

As per Section 2.3.4, provided we can estimate $\overline{A}_f$ (resp. $\overline{B}_f$) we can calculate K^* (resp. S^*). Estimating the concentration factors can be done using analytical approaches such as those mentioned in Section 2.3.4 (see Watt et al. 1976 for a review of such approaches). Alternatively, for special microscopic distributions of strain and stress, the concentration factors are shown to equal unity (Hill 1963). Accordingly, Eqs. (3.12) to (3.13) lead to the well known bounding theorems corresponding to the Voigt and Reuss averages for effective moduli respectively. These moduli bounds, and their associated physical behaviours, are explored in further detail within this chapter.

Finally, due to isotropy $Q^{-1} = Q_m^{-1} = Q_f^{-1}$ (see Section 2.4.2). With the above relations, we are now ready to investigate the various modelling concepts and decoupling assumptions in further detail.

3.2.2 Khalili and Valliappan (1996)

The authors take a top-down approach by first presenting the governing equations for a poroelastic DC material. The quantities requiring closure are subsequently identified in the process. Constitutive behaviours are then sought through thought experiments that isolate volumetric changes of the constituents. Superposition due to linearity, and Betti's reciprocal work theorem finally allow for recovery of the macroscopic behaviour in terms of constituent responses. In doing, expressions for the effective coefficients are identified.

Khalili and Valliappan (1996) implicitly assume that the fracture phase is all void space. Additionally, the following assumption is also made: $B_m \phi_f^0 = B_f \phi_m^0$. This relation is restrictive, and is later removed in Khalili (2003) and Khalili and Selvadurai (2003), due to the resulting compatibility enforced between bulk moduli (Loret and Rizzi 1999). We present coefficient models derived by the authors without this assumption (Table 3.1). The coefficient models from Khalili and Valliappan (1996) (Table 3.1), are then consistent with results from Berryman and Wang (1995), Loret and Rizzi (1999), and Dormieux et al. (2006) (the latter whilst assuming isotropy).

3.2.3 Borja and Koliji (2009)

In Borja and Koliji (2009), the authors consider the evolution of internal energy density and derive a thermodynamically consistent effective stress expression. Aggregate material is used as their reference material. The void space assumption is thus implicit. We present the effective stress expression from Borja and Koliji (2009) for an isotropic single phase dual-continuum system as follows

$$d\Sigma' = d\Sigma + \psi_m B dP_m + \psi_f B dP_f, \tag{3.14}$$

where $B = 1 - K^*/K_s$ is the equivalent single-porosity Biot coefficient for an isotropic material in which K_s denotes the bulk modulus of the solid matrix (grain) material. Notation ψ_α is the pore fraction of continuum α such that

$$\psi_\alpha = \frac{\vartheta_\alpha}{\vartheta}, \tag{3.15}$$

where ϑ_α is the Eulerian porosity for continuum α. ϑ_α is defined as the ratio of the current continuum pore volume $|\Omega_\alpha^p|$ to the bulk volume of the current (deformed) configuration $|\Omega|$. Notation $\vartheta = \vartheta_m + \vartheta_f$ is the equivalent single Eulerian porosity. In the limit of infinitesimal transformations $\vartheta_\alpha \approx \vartheta_\alpha^0 = \phi_\alpha^0$ (Dormieux et al. 2006; Choo et al. 2016). As a result $\psi_\alpha \approx \psi_\alpha^0$. Finally, comparison of Eq. (3.14) with Eq. (3.5) leads to the following relations for effective (isotropic) Biot coefficients $B_m = \psi_m^0 B$ and $B_f = \psi_f^0 B$.

	B_f	B_m	M_f^{-1}	Q^{-1}	M_m^{-1}
Khalili and Valliappan (1996)[+]	$1 - \dfrac{K^*}{K_m}$	$\dfrac{K^*}{K_m} - \dfrac{K^*}{K_s}$	$\dfrac{\phi_f^0}{K_l} + \dfrac{b_f - \phi_f^0}{K_m}$	$\dfrac{b_f - \phi_f^0}{K_s} - \dfrac{b_f - \phi_f^0}{K_m}$	$\dfrac{\phi_m^0}{K_l} + \dfrac{b_m - \phi_m^0}{K_s} - \dfrac{1}{Q}$
Borja and Koliji (2009)[+]	$\psi_f^0 B$	$\psi_m^0 B$	$\dfrac{\phi_f^0}{K_l}$	0	$\dfrac{\phi_m^0}{K_l}$
Berryman (2002)[++]	$b_f \dfrac{K^* - K_m}{K_f - K_m}$	$b_m \dfrac{K^* - K_f}{K_m - K_f}$	$A_{33} - \dfrac{(b_f)^2}{K^*}$	$A_{23} - \dfrac{b_m b_f}{K^*}$	$A_{22} - \dfrac{(b_m)^2}{K^*}$

Table 3.1: Poroelastic coefficient formulations by author. [+] Assuming $\partial \psi_\alpha / \partial t \approx 0$. [++] Coefficients A_{22}, A_{23} and A_{33} are given in Table 3.2. Note that our expressions for coefficient models from Khalili and Valliappan (1996) are slightly different to their original presentation. This is done to highlight the similarities between expressions for B_f and M_f^{-1} and single-porosity equivalents, B and M^{-1} (see for example Section 2.5 or Coussy (2004)).

Borja and Koliji (2009) identify the requirement for a constitutive expression for variations in ψ_α based on energy conjugacy with P_α (their Eq. (76)). However, explicit constitutive equations for ψ_α remain, to the best of the current authors' knowledge, an open question. We do note, however, that Borja and Choo (2016) develop a framework that allows for the tracking of pore fraction evolutions numerically.

As an initial approach to deriving an algebraic expression for variations in ψ_α we first consider the following mass balance equation given in Borja and Koliji (2009) (see also Choo and Borja 2015),

$$B_\alpha \frac{\partial E}{\partial t} + \phi^0 \frac{\partial \psi_\alpha}{\partial t} + \frac{\phi_\alpha^0}{K_l} \frac{\partial P_\alpha}{\partial t} + \frac{q_\alpha}{K_l} \nabla P_\alpha + \nabla \cdot q_\alpha = \frac{\gamma_\alpha}{\rho_l^0}. \tag{3.16}$$

where we have used the small perturbation assumptions described in Sections 2.2.3 and 2.2.4, allowing us to set $\rho_l \approx \rho_l^0$ and $\phi_\alpha \approx \phi_\alpha^0$.

We can derive an alternative form of the mass balance here by substitution of Eq. (3.8) or Eq. (3.9), together with Darcy's law, into Eq. (2.2) (resp. Eq. (2.3)) such that

$$B_\alpha \frac{\partial E}{\partial t} + \left(\frac{1}{N_\alpha} + \frac{\phi_\alpha^0}{K_l} \right) \frac{\partial P_\alpha}{\partial t} + \frac{1}{Q} \frac{\partial P_\beta}{\partial t} + \nabla \cdot q_\alpha = \frac{\gamma_\alpha}{\rho_l^0}, \tag{3.17}$$

where we have used Eq. (2.30) to decompose M_α^{-1}.

Under the assumption of small variations in fluid density (low compressibility), the fourth term on the left-hand side of Eq. (3.16) can be neglected. Comparing Eq. (3.16) and Eq. (3.17) leads to the following identity

$$\phi^0 \frac{\partial \psi_\alpha}{\partial t} = \frac{1}{N_\alpha} \frac{\partial P_\alpha}{\partial t} + \frac{1}{Q} \frac{\partial P_\beta}{\partial t} \tag{3.18}$$

In the works of Choo and Borja (2015) and Choo et al. (2016), the authors achieve non-algebraic closure of the mass balance equations for each continuum by assuming $\partial \psi_\alpha / \partial t \approx 0$. This assumption is equivalent to

$$\frac{1}{N_\alpha} = \frac{1}{Q} = 0 \quad \text{or} \quad \frac{\partial P_\alpha}{\partial t} = -\frac{N_\alpha}{Q} \frac{\partial P_\beta}{\partial t}, \tag{3.19}$$

in Eq. (3.18). In this work we focus on the first relation in Eq. (3.19), given our interest in the parameters themselves. Accordingly, we identify the closure condition $\partial \psi_\alpha / \partial t \approx 0$ with values for material coefficients N_α^{-1} and Q^{-1} of zero.

A summary of the coefficient models from Borja and Koliji (2009), under the explicit assumption $\partial \psi_\alpha / \partial t \approx 0$, mapped to the constitutive model of Eq. (3.5) and Eqs. (3.8) to (3.9) is shown in Table 3.1.

3.2.4 Berryman (2002)

The motivation behind the approach by Berryman (2002) is to formulate coefficient models using intrinsic (continuum) fracture properties such as the fracture bulk modulus K_f. Accordingly, the authors use a top-down approach whose starting point is the macroscopic constitutive model written within a pure stiffness setting (Σ and P_α as primary variables, contrary to conventional poroelastic modelling)

$$
\begin{bmatrix} dE \\ d\xi_m \\ d\xi_f \end{bmatrix} = \begin{bmatrix} A_{11} & A_{12} & A_{13} \\ A_{21} & A_{22} & A_{23} \\ A_{31} & A_{32} & A_{33} \end{bmatrix} \begin{bmatrix} d\Sigma \\ dP_m \\ dP_f \end{bmatrix}.
\tag{3.20}
$$

The goal is then to find expressions for coefficients $A_{11} - A_{33}$. Symmetry of the coefficient matrix in Eq. (3.20) is implied. A comparison of Eq. (3.20) with Eq. (3.5) and Eqs. (3.8) to (3.9) reveals the following relations

$$
K^* = \frac{1}{A_{11}}, \qquad B_m = \frac{A_{12}}{A_{11}}, \qquad B_f = \frac{A_{13}}{A_{11}},
$$
$$
\frac{1}{M_m} = A_{22} - \frac{(A_{12})^2}{A_{11}}, \qquad \frac{1}{Q} = A_{23} - \frac{A_{12}A_{13}}{A_{11}}, \qquad \frac{1}{M_f} = A_{33} - \frac{(A_{13})^2}{A_{11}}.
\tag{3.21}
$$

To identify expressions for the parameters in Eq. (3.20), Berryman (2002) considers scenarios of uniform expansion (or contraction). These scenarios are equivalent to asking whether we can find combinations of $d\Sigma = d\bar{\sigma}_m = d\bar{\sigma}_f$ and pore pressures dP_m and dP_f, such that expansion or contraction is self-similar, i.e. $dE = d\bar{\epsilon}_m = d\bar{\epsilon}_f$ (Berryman 2002). Note, intrinsic averages are implied, but not explicitly mentioned by Berryman (2002). As a result of the expansion/contraction thought experiments, the authors are able to relate Eq. (3.20) to (averaged) microscale constituent equations. To define these averaged equations we consider arguments posed by Hashin (1972) for intrinsic averaging over the microscopic stress-strain relation for phase α. Accordingly, following intrinsic averaging over a local stress-strain relation as per Hashin (1972),

$$
\bar{\sigma}_\alpha = \overline{(\mathbb{C}_\alpha : \epsilon_\alpha)}_\alpha = \mathbb{C}_\alpha \bar{\epsilon}_\alpha.
\tag{3.22}
$$

From Eq. (3.22) we see that the parameters from the local constituent constitutive relation following intrinsic averaging remain unchanged. Consequently, using

and extending the arguments carried by Eq. (3.22), the averaged microscale equations used in Berryman (2002) are posed in the pure stiffness formulation as

$$d\bar{\epsilon}_\alpha = \frac{1}{K_\alpha}\left(d\bar{\sigma}_\alpha - b_\alpha dP_\alpha\right) \tag{3.23}$$

$$d\xi_\alpha = \frac{v_\alpha}{K_\alpha}\left(b_\alpha d\bar{\sigma}_\alpha + \frac{dP_\alpha}{\mathcal{B}_\alpha}\right) \tag{3.24}$$

where $\mathcal{B}_\alpha$ denotes the microscopic Skempton coefficient, given as (Cheng 2016),

$$\mathcal{B}_\alpha = \frac{b_\alpha m_\alpha}{K_\alpha + (b_\alpha)^2 m_\alpha} \tag{3.25}$$

where K_α^s is the bulk modulus of the solid material in continuum α and the microscopic Biot modulus $(m_\alpha)^{-1}$ is given as (Cheng 2016),

$$\frac{1}{m_\alpha} = \frac{\varphi_\alpha^0}{K_l} + \frac{b_\alpha - \varphi_\alpha^0}{K_\alpha^s} \tag{3.26}$$

Expressions for $A_{11} - A_{33}$ are finally recovered (Table 3.2), using the uniform expansion/contraction thought experiments described above. With the relations in Eq. (3.21) we get material coefficient formulations pertaining to the conventional mixed compliance setting (E and P_α as primary variables) (Table 3.1).

Coefficient	Berryman (2002) Formulation
A_{11}	$\dfrac{1}{K^*}$
A_{12}	$\dfrac{b_m}{K_m}\dfrac{1-K_f/K^*}{1-K_f/K_m}$
A_{13}	$\dfrac{b_f}{K_f}\dfrac{1-K_m/K^*}{1-K_m/K_f}$
A_{22}	$\dfrac{v_m b_m}{\mathcal{B}_m K_m} - \left(\dfrac{b_m}{1-K_m/K_f}\right)^2\left\{\dfrac{v_m}{K_m} + \dfrac{v_f}{K_f} - \dfrac{1}{K^*}\right\}$
A_{23}	$\dfrac{K_m K_f b_m b_f}{(K_f-K_m)^2}\left\{\dfrac{v_m}{K_m} + \dfrac{v_f}{K_f} - \dfrac{1}{K^*}\right\}$
A_{33}	$\dfrac{v_f b_f}{\mathcal{B}_f K_f} - \left(\dfrac{b_f}{1-K_f/K_m}\right)^2\left\{\dfrac{v_m}{K_m} + \dfrac{v_f}{K_f} - \dfrac{1}{K^*}\right\}$

Table 3.2: Berryman (2002) material coefficient formulations for the pure stiffness constitutive model.

As a final note on the Berryman (2002) coefficient models, recent users have explicitly assumed $A_{23} = A_{32} = 0$ as a closure condition to generalise the dual-continuum system to a multi-continuum one (Kim et al. 2012; Mehrabian and Abousleiman 2014; Mehrabian 2018). Subsequently, this condition provides ex-

plicit relations between material properties and simplifies the coefficient models. It is still unclear how this assumption may affect the system.

3.2.5 In sum

Coefficient models from Khalili and Valliappan (1996) and Borja and Koliji (2009) both make an underlying void space assumption for the high permeability, low storage continuum. Subsequently, under the void space assumption $K_f = 0$ and $\nu_f = \phi_f$. Models from Borja and Koliji (2009) make use of continuum pore fractions, but still require a final closure relationship for the evolution of each pore fraction. Finally, models from Berryman (2002) make no underlying assumption on the microscopic porosity, and thus the stiffness of the high permeability, low storage continuum. Consequently, $K_f > 0$ and $\varphi_f = \phi_f/\nu_f$ from Eq. (2.68).

In terms of pressure decoupling assumptions we have two types: The first are implicit assumptions for which the constitutive relations are postulated without inter-continuum pressure coupling. The second are explicit assumptions for which the full constitutive model is the starting point (or the requirement for constitutive expressions are at least identified in the case of Borja and Koliji (2009)). The explicit decoupling assumptions are then made so as to provide relations between material properties and to simplify coefficient models (e.g. due to non-algebraic closure). However, the physical justifications and/or implications of these assumptions still remain an open question. We explore these implications in the remainder of this chapter, after a brief detour to reconcile several of the constitutive models just introduced with the one derived in Chapter 2.

3.3 Constitutive model equivalencies

Under certain conditions, the coefficient models introduced in Eqs. (2.92) to (2.93) and Eqs. (2.100) to (2.103) reduce to the mechanical property based parameter models discussed in Section 3.2. For the latter, we assume a natural reference state for stress, strain and continuum pressures such that the constitutive forms coincide. Lastly, to provide equivalences we make use of the decomposition in Eq. (2.30).

In the case of soils, the high permeability (transport) continuum is all void space (Koliji et al. 2008). As a result $\mathbb{C}_f = 0$, and we recover the original anisotropic parameter models proposed by Dormieux et al. (2006). For an isotropic material, the constitutive system is written in terms of scalar invariants of the tensorial quantities. Accordingly, with a change from the mixed compliance constitutive formulation to a pure stiffness formulation, we recover the dual-stiffness models introduced by Berryman (2002) (Table 3.1). Finally, combining the void space transport and isotropic dual-material assumptions, allows us to recover

parameter models originally proposed by Berryman and Wang (1995) and Khalili and Valliappan (1996) (Table 3.1).

By highlighting equivalences between the micromechanically derived model and the phenomenological models, we can see how explicit modelling assumptions made in the former arise implicitly in the latter. Such insights highlight the benefits of a micromechanical approach. We extend these insights in the next section where we study explicit constitutive decoupling assumptions.

3.4 Explicit decoupling and parameter bounds

In the following, we explore the implications of various explicit decoupling assumptions such as those where $A_{23} = A_{32} = 0$ in Eq. (3.20). To do so, we use arguments from micromechanics to show heuristically that the inverse to explicit decoupling is to assume that Eq. (3.10) or Eq. (3.11) can be calculated directly by considering certain limiting behaviours. These limiting behaviours correspond to bounds on K^*. Accordingly, bounds on the effective constitutive coefficients then follow from bounds on K^*. Such bounds on parameters are attractive as they provide simple estimates of effective properties of interest, as well as a means to verify the values of these properties (Torquato 1991).

3.4.1 Isostrain: $Q^{-1} = 0$

Whilst this explicit assumption has not been used within literature its consideration remains instructive. We define assumption $Q^{-1} = 0$ in terms of $d\phi_m$ (although converse arguments may be used for $d\phi_f$). From Eq. (3.6), the term $Q^{-1} = 0$ is then equivalent to

$$\frac{1}{Q} = \frac{\partial \phi_m}{\partial P_f}\bigg|_{\substack{dE=0 \\ dP_m=0}} = 0. \tag{3.27}$$

Next we define the following intrinsic average over the variation form of the constitutive model in Eqs. (2.66) to (2.67), whilst also assuming isotropy such that

$$d\overline{\sigma}_\alpha = K_\alpha d\overline{\epsilon}_\alpha - b_\alpha dP_\alpha, \tag{3.28}$$

$$d\phi_\alpha = v_\alpha \left(b_\alpha d\overline{\epsilon}_\alpha + \frac{dP_\alpha}{n_\alpha} \right). \tag{3.29}$$

We consider Eqs. (3.28) to (3.29) for the case $\alpha = m$. Under a drained matrix, $dP_m = 0$. Subsequently, Eq. (3.29) shows that a zero matrix porosity variation ($d\phi_m = 0$) can only hold if the average volumetric matrix strain variation is zero ($d\overline{\epsilon}_m = 0$). Further, we can see from Eq. (3.28) that if the matrix is drained and

does not deform, the average mean matrix stress variation is also zero ($d\overline{\sigma}_m = 0$). This latter result will be useful for discussions on the explicit decoupling assumption $A_{23} = 0$.

Proceeding with Eq. (3.27) and the macroscopic strain constraint $dE = 0$ (or $E = E^0$), the strain partition in Eq. (2.34) suggests that if $dE = d\overline{\epsilon}_m = 0$ then $d\overline{\epsilon}_f = 0$. Accordingly, $Q^{-1} = 0$ holds under a strain distribution condition referred to as *isostrain*

$$dE = d\overline{\epsilon}_m = d\overline{\epsilon}_f, \quad \overline{A}_m = \overline{A}_f = 1. \tag{3.30}$$

Several interesting features can be observed from Eq. (3.30). First, we consider isostrain in the variation form holding such that $E^0 = \overline{\epsilon}_m^0 = \overline{\epsilon}_f^0$ and $E = \overline{\epsilon}_m = \overline{\epsilon}_f$. Further, we restate that the first equality in Eq. (3.30) is only equal to zero under a constrained macroscopic strain condition of $dE = 0$ such as that in Eq. (3.27). Accordingly, from these strain equalities, and the zero strain variation constraint, we see $Q^{-1} = 0$ holds when $\left[E^0 = \overline{\epsilon}_m^0 = \overline{\epsilon}_f^0 \right] \equiv \left[E = \overline{\epsilon}_m = \overline{\epsilon}_f \right]$. Evidently, in the case with an initial strain state of zero, the latter equivalence is trivially satisfied by $E = \overline{\epsilon}_m = \overline{\epsilon}_f = 0$. Lastly, equivalence of microscopically averaged strains and macroscopic strain under isostrain in Eq. (3.12), gives rise to the average strain concentration factors relation in Eq. (3.30).

The isostrain distribution can be obtained when elements are set in parallel to the direction of loading (Fig. 3.1). Under isostrain, the upscaled bulk modulus is then the Voigt average of the constituent moduli (Voigt 1887, 1928),

$$K^* = K^{\mathcal{V}} = v_m K_m + v_f K_f. \tag{3.31}$$

Hill (1963) used variational principles to show that the Voigt average represents an upper bound on K^*, and is naturally obtained by substitution of $\overline{A}_f = 1$ into Eq. (3.10). As a result, effective coefficients calculated with $K^{\mathcal{V}}$ correspond to bounds on these parameters. To explore this further we consider the case for the effective Biot coefficients under the the void space assumption.

Assuming a drained *void* fracture continuum ($dP_f = 0$) and from Eq. (3.29), the average volumetric fracture strain variation is equal to the effective fracture pore strain ($d\overline{\epsilon}_f = d\phi_f/\phi_f^0$). Note, the void space assumption means $b_f = 1$ since $K_f = 0$, and $\phi_f^0 = v_f$ from Eq. (2.68) since $\varphi_f^0 = 1$. Thus, in analogy to Eq. (3.30), isostrain can be summarised for this case as

$$dE = d\overline{\epsilon}_m = \frac{d\phi_f}{\phi_f^0}. \tag{3.32}$$

From Eq. (3.7) with drained matrix and fracture continua, together with the void space isotrain condition Eq. (3.32), we get the following lower bound on B_f

$$B_f = \frac{\partial \phi_f}{\partial E}\Big|_{\substack{dP_m=0 \\ dP_f=0}} = \phi_f^0.$$

(3.33)

From Eq. (2.104), $B = B_m + B_f$, the lower bound on B_f corresponds to an upper bound on B_m

$$B_m = v_m \left(1 - \frac{K_m}{K_s}\right),$$

(3.34)

where $v_m = 1 - \phi_f^0$, and where we have used $K^* = K^\mathcal{V} = v_m K_m$.

From the first equality in Eq. (3.27) we expect $Q^{-1} \leqslant 0$ since matrix porosity must reduce in order to accommodate the pressure driven fracture expansion (see also similar arguments in Berryman and Wang (1995)). Thus, based on the arguments described in this section we can infer that the explicit decoupling assumption $Q^{-1} = 0$ is concurrent with an *upper bound* on Q.
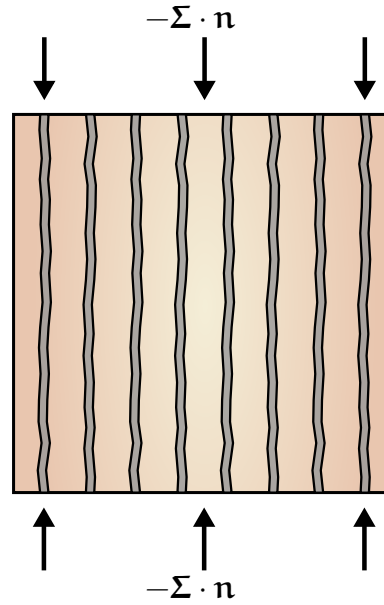
Figure 3.1: Constituent arrangements in the isostrain condition.

3.4.2 *Incompressible grain isostrain:* $(N_\alpha)^{-1} = Q^{-1} = 0$

We now investigate the coefficient models from Borja and Koliji (2009) under the assumption $\partial \psi_\alpha / \partial t \approx 0$ made by Choo and Borja (2015) and Choo et al. (2016).

In Section 3.2.3, we considered the case $\partial \psi_\alpha / \partial t \approx 0$ amounting to $(N_\alpha)^{-1} = Q^{-1} = 0$ when mapping to the constitutive model shown in Eqs. (3.5) to (3.7). It is of interest to see under what conditions the result $(N_\alpha)^{-1} = Q^{-1} = 0$ arises when starting from the void space coefficient models built from constituent mechanical properties (e.g. those from Khalili and Valliappan (1996)).

The set of explicit assumptions: $(N_\alpha)^{-1} = Q^{-1} = 0$, can easily be derived from the microscale by first considering isostrain (and thus $Q^{-1} = 0$). With the resulting bounds arising from isostrain, Eqs. (3.33) to (3.34), along with the assumption $K_s = \infty$, we obtain $(N_\alpha)^{-1} = 0$ using the coefficient models of Khalili and Valliappan (1996) (Table 3.1, with Eq. (2.30) to decompose $(M_\alpha)^{-1}$). We therefore refer to conditions resulting in $(N_\alpha)^{-1} = Q^{-1} = 0$ as *incompressible grain isostrain*.

As far as parameters in the balance of mass are concerned, Eq. (3.16) and Eq. (3.17) are identical when assuming $\partial\psi_\alpha/\partial t \approx 0$ in the former and incompressible grain isostrain in the latter. However, differences in mass balance behaviour may be introduced through the way in which B_α is modelled. It is therefore of interest to see how the effective Biot coefficients calculated using the respective void space coefficient models under incompressible grain isostrain compare to the bounds established in Eqs. (3.33) to (3.34).

Under the incompressible grain assumption the upper bound for B_m now reads $B_m = \nu_m$. Accordingly, when using $K^\mathcal{V} = \nu_m K_m$ and $K_s = \infty$ in the coefficient models of Khalili and Valliappan (1996) we can see that the bounds on $B_m = \nu_m$ and $B_f = \phi_f^0$ are naturally recovered (Table 3.1). In contrast, from Table 3.1 the effective Biot coefficients calculated using the models of Borja and Koliji (2009) are $B_m = \psi_m$ and $B_f = \psi_f$, since $B = 1$ for incompressible solid material. Due to the differences in effective Biot coefficients (and thus other constitutive parameters), we expect disparity in poroelastic behaviour when using the two sets of void space coefficient models.

3.4.3 Isostress: $A_{23}(= A_{32}) = 0$

Finally, we study the pure stiffness setting with the condition $A_{23} = 0$ in light of the assumptions made in Nguyen and Abousleiman (2010), Kim et al. (2012), Mehrabian and Abousleiman (2014) and Mehrabian (2018). Given that cross coupling coefficients are equivalent in both the variation in fluid volume content and variation in Lagrangian porosity formulations, we write

$$A_{23} = \left.\frac{\partial\xi_m}{\partial P_f}\right|_{\substack{d\Sigma=0\\dP_m=0}} \equiv \left.\frac{\partial\phi_m}{\partial P_f}\right|_{\substack{d\Sigma=0\\dP_m=0}} = 0. \tag{3.35}$$

In Section 3.4.1 we established that a drained matrix experiencing no deformation is concurrent with a average mean matrix stress variation of zero. Considering the macroscopic stress constraint in Eq. (3.35) ($d\Sigma = 0$) and the stress partition in Eq. (2.35), if $d\Sigma = d\overline{\sigma}_m = 0$ then $d\overline{\sigma}_f = 0$. Accordingly, $(A_{23})^{-1} = 0$ holds under a stress distribution condition referred to as *isostress*

$$d\Sigma = d\overline{\sigma}_m = d\overline{\sigma}_f, \quad \overline{B}_m = \overline{B}_f = 1. \tag{3.36}$$

Following similar logic as for the isostrain case, we deduce that $(A_{23})^{-1} = 0$ holds when $\left[\Sigma^0 = \overline{\sigma}_m^0 = \overline{\sigma}_f^0\right] \equiv \left[\Sigma = \overline{\sigma}_m = \overline{\sigma}_f\right]$. Further, in the case with an initial stress state of zero, the stress equivalence at the updated state is trivially satisfied by $\Sigma = \overline{\sigma}_m = \overline{\sigma}_f = 0$. Lastly, equivalence of microscopically averaged stresses and macroscopic stress under isostress in Eq. (3.13), gives rise to the average stress concentration factors relation in Eq. (3.36).

The classical configuration for the isostress condition, are constituent elements arranged transversely to the direction of applied load (Fig. 3.2a). For isotropic fracture networks, a more frequent configuration that shows isostress behaviour is within a solid-fluid suspension (Fig. 3.2b). Such a situation may occur if a network of open fractures totally permeates the solid, thus completely dissociating the matrix material.

(a) Transverse arrangement

(b) Solid-fluid suspension
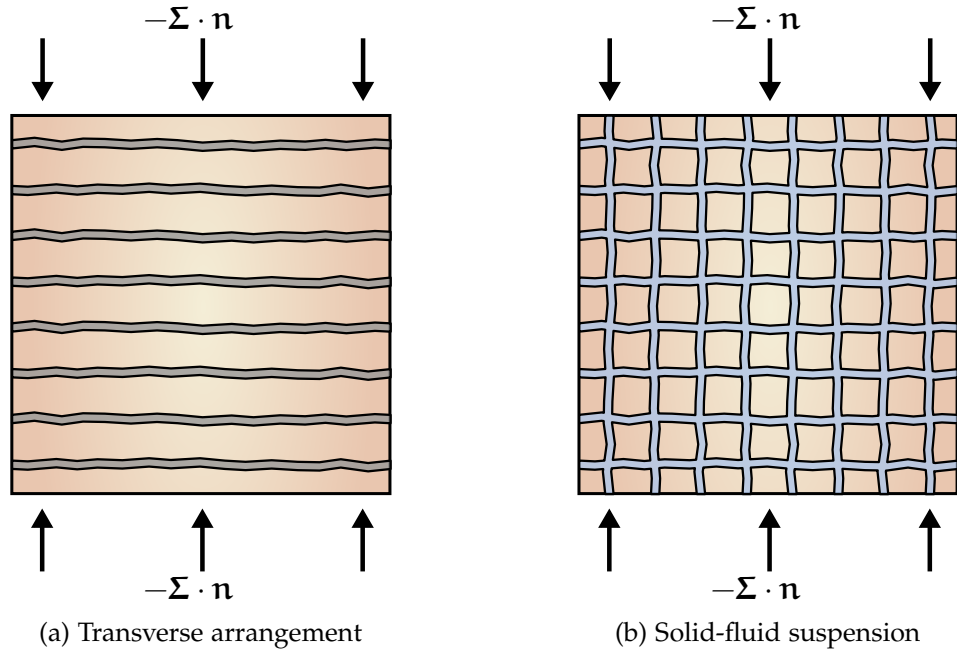
Figure 3.2: Constituent arrangements leading to the isostress condition.

Under isostress, the bulk modulus of the heterogeneous material is then the Reuss average of the constituent bulk moduli (Reuss 1929),

$$\frac{1}{K^*} = \frac{1}{K^{\mathcal{R}}} = \frac{\nu_m}{K_m} + \frac{\nu_f}{K_f}. \tag{3.37}$$

Hill (1963) showed that the Reuss average is a lower bound on K^*, and is naturally obtained by substitution of $\overline{B}_f = 1$ into Eq. (3.11), or from $A_{23} = 0$ in Table 3.2. In the former we assume $S^* \approx (K^*)^{-1}$ on the basis of the statistical homogeneity assumptions introduced in the previous chapter. In analogy to $K^{\mathcal{V}}$, use of $K^{\mathcal{R}}$ for the calculation of the effective constitutive parameters will result in bounds on these parameters. We investigate this statement in the remainder of this section.

We consider the case when K_f is zero (void space fracture phase). Accordingly, from Eq. (3.37) K^* is also zero. From Eq. (3.36) with Eq. (3.5) for $d\Sigma$, and Eq. (3.28) for $d\overline{\sigma}_m$ and $d\overline{\sigma}_f$, we obtain

$$B_m dP_m - B_f dP_f = K_m d\overline{\epsilon}_m - b_m dP_m = -1dP_f. \tag{3.38}$$

From the required isostress equality $d\Sigma = d\overline{\sigma}_f$ and thus from Eq. (3.38) we have $B_m dP_m - B_f dP_f = -1dP_f$. Consequently, Eq. (3.38) followed by Eq. (2.104) allows us to establish the following parameter bounds under isostress

$$B_m = 0, \quad B_f = 1. \tag{3.39}$$

From Eq. (3.39) we see that use of the Reuss bound corresponds to an upper bound on B_f and a lower bound on B_m. Interestingly, the bounds on B_f from this section and Section 3.4.1 ($\phi_f^0 \leqslant B_f \leqslant 1$), are very similar to those established on B for the single-porosity model ($\phi^0 \leqslant B \leqslant 1$) (Dormieux et al. 2006).

3.4.4 On moduli upscaling

In Nguyen and Abousleiman (2010), Kim et al. (2012), Kim and Moridis (2013), Mehrabian and Abousleiman (2014, 2015) and more recently Mehrabian (2018), isostress is implicitly assumed. Upscaling of constituent moduli is then admitted through the Reuss average. This raises the question as to whether this is a reasonable approach to upscaling or not?

In the previous section we stated that the Reuss and Voigt average represent lower and upper bounds for effective moduli respectively. Specifically, these bounds represent a minimum and maximum limit, between, or at which, effective moduli arise. However, for the effective bulk modulus of isotropic heterogeneous materials, variational bounds by Hashin and Shtrikman (1963) have been shown in the same paper to be the best possible, given only constituent moduli and volume fractions. This result is obtained by solving exactly for the effective bulk modulus of a specific heterogeneous material geometry (composite sphere assemblage). One then observes that the resultant solution coincides with either bound, depending on the stiffness of the inclusion relative to the host material. The lower Hashin-Shtrikman (HS) effective bulk modulus bound is given as

$$K^{\mathcal{H}-} = K_f + \frac{v_m}{(K_m - K_f)^{-1} + v_f(K_f + \frac{4}{3}G_f)^{-1}}, \tag{3.40}$$

where G_f denotes the shear modulus of the fracture material. The upper bound, $K^{\mathcal{H}+}$ can be determined by swapping subscripts f and m in Eq. (3.40).

When $G_f = 0$, such as in a fluid suspension geometry, the HS lower bound and the Reuss bound coincide. It follows that in this geometry, with the stiffness of a void space fracture phase ($K_f = 0$), both the Reuss and HS lower bound result in $K^{\mathcal{R}} = K^{\mathcal{H}-} = 0$. However, in situations when the fracture phase has an intrinsic stiffness, the Reuss and HS lower bounds may be significantly different (Watt et al. 1976).

Bounds can be used as a first approach to upscaling under certain geometries. If a fracture network completely percolates a matrix then it will have the maximum effect of weakening the rock (Watt et al. 1976). The effective bulk modulus of the heterogeneous material will then coincide with the HS lower bound (Boucher 1974; Watt et al. 1976). In the general case fractures are likely to have an associated stiffness (Jaeger et al. 2009). We thus recommend using the HS lower bound over the Reuss average as a first approach to upscaling for such geometries. This procedure is also in line with the assumptions built into the continuum approach: The continuum assumption is linked to ones ability to define an REV over which properties can be averaged. For a fractured system, such an REV cannot be justified if the system is poorly connected (Berkowitz 2002). Use of the HS lower bound, as a first approach to moduli averaging, thus supports the notion of a well-connected isotropic dense fracture network, over which an REV could be defined.

When the underlying material geometry precludes the use of bounds as methods for upscaling, one must use other homogenisation methods. Comprehensive summaries of such approaches can be found in the works of Aboudi (1991), Nemat-Nasser and Hori (1993) and Torquato (2002) for example.

3.5 Qualitative analysis using the Mandel problem

In this section we further investigate the physical impacts of different coefficient modelling concepts and assumptions on the poroelastic response of a dual-continuum material. To do so we use solutions to the dual-continuum Mandel-problem from Nguyen and Abousleiman (2010) (Appendix B).

First, we study the effects of including intrinsic fracture properties or not, as assumed by the coefficient models of Berryman (2002) and Khalili and Valliappan (1996) respectively. Secondly, we consider the effects of implicit decoupling assumptions, where the constitutive model starts with no pressure coupling. Finally, we investigate the effects of explicit decoupling assumptions, where the full constitutive model Eqs. (3.5) to (3.7) is the starting point but inter-continuum pressure coupling is neglected. As a result, bounds are used for the calculation of K^* (and thus the calculation of the effective constitutive coefficients).

Finally, in the remainder of this analysis we assume our dual-continuum to be a dual-porosity material. Subsequently, the effective permeability of the matrix is zero. Further, we assume a natural reference state for which the initial stress, strain and continuum pressures are zero.

3.5.1 Dual-continuum Mandel problem

The problem geometry is described as an infinitely long cuboid such that the plane-strain condition holds (i.e. $u_z = 0$ and $q_{m,z} = q_{f,z} = 0$) (Fig. 3.3). The domain is sandwiched between two impermeable rigid plates, and is free to displace both laterally and vertically. A constant compressive force, $\int_{-h_1}^{h_1} -\Sigma_{yy} \, dx = F$, is applied at the rigid plate boundaries, Γ_N and Γ_S (north and south boundaries respectively). The east and west boundaries, Γ_E and Γ_W respectively, are then free to drain such that $P_m = P_f = 0$ at these boundaries.

In summary the boundary conditions are,

$$\Sigma_{xx} = \Sigma_{xy} = 0 \quad \text{on } \Gamma_E \cup \Gamma_W, \tag{3.41}$$

$$P_m = P_f = 0 \quad \text{on } \Gamma_E \cup \Gamma_W, \tag{3.42}$$

$$\Sigma_{xy} = 0 \quad \text{on } \Gamma_N \cup \Gamma_S, \tag{3.43}$$

$$q_{m,y} = q_{f,y} = 0 \quad \text{on } \Gamma_N \cup \Gamma_S, \tag{3.44}$$

$$\int_{-h_1}^{h_1} -\Sigma_{yy} \, dx = F \quad \text{on } \Gamma_N \cup \Gamma_S, \tag{3.45}$$

where only a quarter of the domain need be considered due to the symmetry of the problem (Fig. 3.3).

For an isotropic dual-continuum material Eq. (2.22) can be rewritten (using Voigt notation for the tensors), as

$$\Sigma = 2G^*E + \lambda^*E\mathbf{1} - \sum_{\alpha=m,f} B_\alpha P_\alpha \mathbf{1} \tag{3.46}$$

where $\lambda^* = (2G^*v^*)/(1 - 2v^*)$ is the macroscopic Lamé constant, in which G^* and v^* are the macroscopic shear modulus and Poisson's ratio respectively. Further, we define the macroscopic strain-displacement compatibility relation

$$E = \underline{\nabla}U = \frac{1}{2}\left(\nabla U + \nabla^\top U\right). \tag{3.47}$$

Substitution of Eq. (3.47) into Eq. (3.46), followed by injection of the result into Eq. (2.4) yields

$$G^*\nabla^2 U + (\lambda^* + G^*)\nabla E = \sum_{\alpha=m,f} B_\alpha \nabla P_\alpha \mathbf{1} - \rho g, \tag{3.48}$$
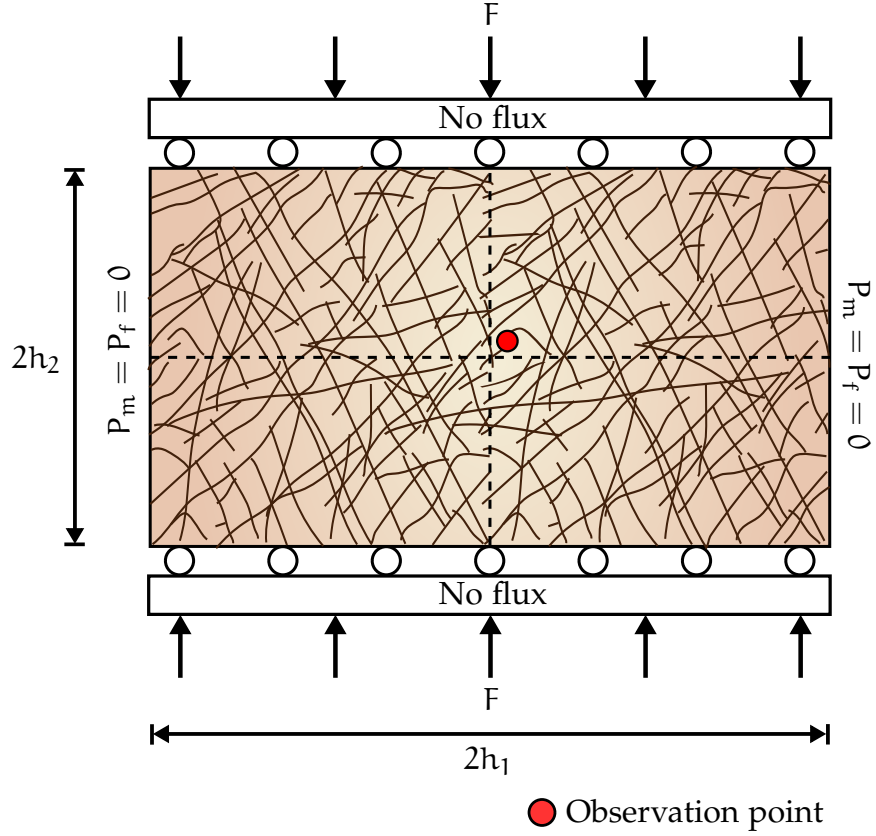
Figure 3.3: Mandel problem setup.

assuming $\gamma' \approx 0$. It can be shown that $\nabla^2 U = \nabla E$, with which, and in the absence of body forces, Eq. (3.48) reduces to

$$\nabla E = \sum_{\alpha=m,f} C_\alpha \nabla P_\alpha, \tag{3.49}$$

where $C_\alpha = [B_\alpha(1 - 2v^*)]/[2G^*(1 - v^*)]$ is the consolidation coefficient belonging to material α.

Integration of Eq. (3.49) leads to

$$E = \sum_{i=m,f} C_\alpha P_\alpha + I(t), \tag{3.50}$$

where $I(t)$ is an integration function. Use of Eq. (3.50) in Eq. (3.17) leads to a set of diffusion equations written entirely in terms of continuum pressures. Solutions to the resulting system of equations are presented in Appendix B, which are based on the original works of Nguyen and Abousleiman (2010).

3.5.2 Data for analysis

For the qualitative analysis we use a quarter of a 2 m $\times$ 2 m deformable porous domain. The studied domain is subjected to a constant top boundary force, $\int_0^1 -2 \times 10^6$ Pa d$x = -2$ MPa·m. Where possible we use values for material prop-

erties that are typically encountered in naturally fractured carbonate reservoirs. We specify the following mechanical properties for all test cases: $K_m = 20$ GPa, $K_s = 70$ GPa, and $\nu^* = 0.2$ (Wang 2000). Values for K^* and K_f are problem dependent. In cases where no rigorous justification is used, we choose values for K^* and K_f without any strict upscaling procedure. In these instances, parameter values are chosen either arbitrarily (but still lying between modulus bounds) or as fractions of already used stiffness moduli. Accordingly, we denote stiffness moduli, whose values are specified without a rigorous justification, by a superscript †.

In all test cases we set fluid properties typical for those of water, such that $\rho_l^0 = 1000$ kg m^{-3}, $\mu_l = 1$ cp and $K_l = 2.5$ GPa. Rock properties related to fluid storage and flow for the test cases are $\phi_m^0 = 0.05$, $k_m = k' = 0.01$ md [1] and $\phi_f^0 = 0.01$ (Nelson 2001). Volume fractions of each material are given as $\nu_f = 0.01$ and $\nu_m = 1 - \nu_f = 0.99$. We assume a dual-porosity material, thus $K_m = 0$. For the effective fracture permeability we use the cubic law (Witherspoon et al. 1980), using a fracture aperture of $a_f = 1.4 \times 10^{-5}$ m and fracture spacing $\ell = 2.8 \times 10^{-3}$ m. Accordingly, we calculate $K_f \approx 1000$ md. Note, a_f and ℓ were also used for the calculations of ϕ_f^0 and ν_f.

3.5.3 Test cases

We consider one test case to investigate the differences between void space and stiff fracture coefficient models, and three test cases to investigate implicit and explicit decoupling assumptions. To calculate the effective constitutive parameters we make use of the models provided in Table 3.1. For each case, analytical solutions to the dual-continuum Mandel problem are compared. Differences in solutions for each case then arise due the parameter permutations described in the case descriptions that follow.

Case 1: Intrinsic fracture properties

In Case 1, we are interested in comparing the differences that arise when considering intrinsic fracture properties. In particular, it is of interest to investigate if coefficient models from Khalili and Valliappan (1996) could still be used even when a fracture has an associated phase stiffness.

To build a hypothesis for when to use Khalili and Valliappan (1996), we consider situations for which we are close to the void space approximation for the fracture phase. In these cases, the initial intrinsic porosity is close to unity ($\varphi_f^0 \approx 1$), and the fracture phase stiffness is likely to be orders of magnitude lower than the grain stiffness ($K_f \ll K_s^f$). As a result, from Eq. (2.69) and Eq. (3.26),

---

[1] 1 darcy (d) = 9.87 $\times 10^{-13}$ m^2.

we expect the intrinsic fracture Biot coefficient and modulus respectively to approach the following: $b_f = 1$ and $(m_\alpha)^{-1} = (K_l)^{-1}$. Accordingly, we anticipate that void space coefficient models could substitute coefficient models using intrinsic fracture properties, when the fracture phase approaches the void space approximation.

To test our hypothesis we consider various combinations of φ_f and K_f, whilst using coefficient models from Khalili and Valliappan (1996) and Berryman (2002). In the former, φ_f and K_f are not explicitly included in the parameter formulations. However, if φ_f and K_f are close to their void space estimates, we expect differences between models to be negligible. We vary fracture moduli magnitude with respect to the solid grain modulus. Accordingly, we consider one case where $K_f^\dagger = K_s^f/1750$ and another case where $K_f^\dagger = K_s^f/35$. For the fracture solid stiffness we take $K_s^f = K_s$.

We consider a heterogeneous material with a network of fractures that completely dissociates the matrix. Upscaling for K^* is then done using the HS lower bound. As a note, use of void space coefficient models implies $K_f = 0$. However, we relax this requirement for the upscaling procedure and use the same effective bulk modulus for both coefficient model cases. The only differences between the constitutive models then come from the inclusion of intrinsic fracture properties in the other effective coefficient models.

Case 2: Implicit decoupling assumptions

For Case 2, we investigate the impact of implicit decoupling assumptions. This is particularly relevant given the use of such decoupled constitutive models in the recent works of Cordero et al. (2019) and Hajiabadi and Khoei (2019). Further, in Khalili (2003) the author showed that implicit decoupling led to non-physical matrix and fracture pressure responses for the uniaxial case considered therein. However, the precise link between implicit decoupling and the observations made by Khalili (2003) still remains an open question.

To mimic implicit assumptions we consider $Q^{-1} = 0$ and $A_{23} = 0$ separately, and make no acknowledgement of these assumptions with respect to relations between mechanical properties. When considering $Q^{-1} = 0$ we use coefficient models from Khalili and Valliappan (1996). When considering $A_{23} = 0$ we use coefficient models Berryman (2002) with with $K_f = 0$. We reference results calculated using the described parameter models against ones for which no decoupling is made with coefficient models from Khalili and Valliappan (1996).

Since we do not enforce relations on K^* through implicit decoupling we take an arbitrary value of $K^{*,\dagger} = 10$ GPa. As a result bounds on the effective constitutive coefficients are not enforced.

Case 3: Explicit decoupling assumption: Isostrain

For Case 3, we investigate the effect of assuming isostrain at the microscale whilst making use of coefficient models from Khalili and Valliappan (1996). Under isostrain the effective and constituent bulk moduli are linked by the Voigt average ($K^{\mathcal{V}} = 19.8$ GPa using the volume fractions defined in Section 3.5.2). This leads naturally to bounds on the effective constitutive coefficients, with $Q = 0$ representing an upper bound. We compare the isostrain results to those computed when using coefficient models with a homogenised bulk modulus coinciding with the HS upper bound and an arbitrary value ($K^{\mathcal{H}+} = 19.5$ GPa and $K^{*,\dagger} = 10$ GPa respectively).

Following Section 3.4.2, we also compare results when using the void space coefficient models of Borja and Koliji (2009) under the assumption of $\partial\psi_\alpha/t = 0$, and Khalili and Valliappan (1996) under the assumption of incompressible grain isostrain. We use $K^{\mathcal{V}} = 19.8$ GPa and $K_s = \infty$ for both sets of coefficient models in this latter isostrain investigation.

Case 4: Explicit decoupling assumption: Isostress

For Case 4, we study the effect of assuming isostress at the microscale. In previous works the coefficient models of Berryman (2002) have been used with an explicit decoupling assumption ($A_{23} = 0$) that implies isostress (Kim et al. 2012; Mehrabian and Abousleiman 2014; Mehrabian 2018).

To avoid cases where $K^* = 0$ we consider the fracture phase to have the following properties: $\varphi_f = 0.7$ with $K_s^f = K_s$ and $K_f^\dagger = K_m/500$. Coefficient models from Berryman (2002) are then used.

We compare results between models parameterised by calculating the effective bulk modulus with the Reuss average ($K^{\mathcal{R}} = 3.3$ GPa), the HS lower bound ($K^{\mathcal{H}-} = 5.7$ GPa) and an arithmetic average of the HS bounds ($K^{A\mathcal{H}} = 12.7$ GPa). The latter modulus is tested in analogy to a dual system with inclusions that do not have the maximum weakening effect on the host material. One example would be a fracture system composed of a network of open and closed fractures. Another would be aggregate material.

3.6 Results and discussion

In the following, we show results of the test cases described above for the dual-continuum Mandel problem. Results are given in terms in evolutions of matrix and fracture pressures, and vertical strain with time.

To aid in our analysis for pressure and vertical strain we introduce the following notions of the *instantaneous* problem and the *time-dependent* problem. In both

cases, mechanical equilibrium is governed for this system by Eq. (3.48). In the instantaneous problem, fluid pressure for continuum α can be shown to be a state function of total stress and fluid pressure P_β. In the time-dependent problem, continuum pressures are governed by way of the diffusion equation, Eq. (3.17).

The instantaneous problem considers the change of the system from an unloaded state t_0 to a loaded state t_{0+} upon application of instantaneous loading. Under such conditions the rate of loading is infinitely faster than the rate of inter-continuum fluid transfer (Coussy 2004). Consequently, each continuum is undrained $m_{l,\alpha}^{t_{0+}} = m_{l,\alpha}^{t_0}$. From Eqs. (3.8) to (3.9), together with the undrained condition ($dm_{l,\alpha} = 0$) we can recover

$$P_\alpha = \left(\frac{1}{M_\alpha} - \frac{M_\beta}{(Q)^2} \right)^{-1} \left(\frac{M_\beta B_\beta}{Q} - B_\alpha \right) E. \tag{3.51}$$

We note that $E_{yy} \propto E$. Substitution of Eq. (3.5) into Eq. (3.51) leads to

$$P_\alpha = -\frac{M_\alpha b_\alpha}{[K^* + M_\alpha(B_\alpha)^2]} \left[\Sigma + \left(B_\beta + \frac{K^*}{B_\alpha Q} \right) P_\beta \right]. \tag{3.52}$$

3.6.1   Case 1: Intrinsic fracture properties

Fig. 3.4a and Fig. 3.4c show matrix and fracture pressure evolutions with varying intrinsic fracture properties. We find a good match in both matrix and fracture pressure evolutions using coefficient models from Khalili and Valliappan (1996) and Berryman (2002) when the fracture is almost all void space ($\varphi_f \approx 1$). In this case the fracture phase stiffness is orders of magnitude lower than the solid grain stiffness ($K_f \ll K_s^f$) (Fig. 3.4a). Even when the intrinsic fracture porosity is diminishing ($\varphi_f = 0.2$), provided the fracture phase stiffness is orders of magnitude lower than the solid stiffness, the difference between early time matrix pressures with the different coefficient model formulations is small (Fig. 3.4a). However, when the fracture bulk modulus is only an order of magnitude lower than the solid modulus ($K_f \not\ll K_s^f$), early time fracture pressure differences become measurable as intrinsic porosity decreases (Fig. 3.4c). This phenomenon can be explained by considering the intrinsic Skempton coefficient. Accordingly, we consider an alternative formulation for $\mathcal{B}_f$ to that shown in Eq. (3.25) (Cheng 2016),

$$\mathcal{B}_f = 1 - \frac{\varphi_f K_f(K_s^f - K_l)}{K_l(K_s^f - K_f) + \varphi_f K_f(K_s^f - K_l)}. \tag{3.53}$$

Use of Eq. (3.53) allows us to cast our observations as a bounding problem such that

$$\mathscr{B}_f(\varphi_f = 1, K_f) < \mathscr{B}_f(\varphi_f < 1, K_f) \leqslant 1. \tag{3.54}$$

The lower bound in Eq. (3.54) is a fictitious one in that technically materials with an intrinsic porosity of one should also have a zero stiffness. However, accepting this contradiction is useful in approaching the bounding problem from a purely quantitative point of view. For the upper bound, Eq. (3.54) shows that as φ_f approaches zero, $\mathscr{B}_f$ must asymptotically approach one.

If the lower bound in Eq. (3.54) for a given K_f is close to one then changes in intrinsic fracture porosity are negligible due to the proximity of the lower and upper bounds. This is the case when $K_f \ll K_s^f$. If the fracture phase stiffness is *not* orders of magnitude lower than the solid stiffness, then the lower bound of $\mathscr{B}_f$ may be significantly less than one. In this case, changes in $\mathscr{B}_f$ cannot be captured when using void space coefficient models alone. Consequently, with these models early time fracture pressure is underestimated as φ_f decreases (Fig. 3.4c).

Fig. 3.4b and Fig. 3.4d show the variation in vertical strain for the softer and stiffer fracture phases respectively. In Fig. 3.4b, the strain evolutions are almost identical when using the more compliant fracture phase for the range of intrinsic fracture porosities. This observation is coupled to the similarity in pressure evolutions. Whilst induced fracture pressures are significantly larger when fracture stiffness and intrinsic porosity are non-negligible, Fig. 3.4d shows very little differences in vertical strain across the whole intrinsic porosity range. This is a direct consequence of the algebraic coefficient of strain in Eq. (3.51) for the fracture phase, which scales proportionally with the variation in fracture pressure.

3.6.2 Case 2: Implicit decoupling

Fig. 3.5 presents the pressure and vertical strain results for the implicit decoupling assumptions test case. When assuming $A_{23} = 0$, the matrix and fracture pressure evolutions are almost identical to the reference case (Fig. 3.5a). Consequently, vertical strains are also very similar to the reference for this decoupling case (Fig. 3.5b). When assuming $Q^{-1} = 0$, the early time matrix and fracture pressures are measurably lower than the reference case (Fig. 3.5a). Accordingly, the early time vertical strain is also greater than the reference when $Q^{-1} = 0$ (Fig. 3.5b).

The results in Fig. 3.5a suggest that the assumption $Q^{-1} = 0$ has the most noticeable effect on the poroelastic behaviour of the dual-medium. As discussed in Section 3.4.1 we would expect $Q^{-1} < 0$. From Eq. (3.52), setting $Q^{-1} = 0$

(a) Pressure

(b) Vertical Strain, E_{yy}

(c) Pressure

(d) Vertical Strain, E_{yy}

Figure 3.4: Matrix ('M') and fracture ('F') pressure (a, c), and vertical strain (b, d) evolutions for the dual-continuum Mandel problem whilst considering the effects of intrinsic fracture properties. 'K&V' denote models from Khalili and Valliappan (1996). Different values of intrinsic fracture porosity $\varphi_f = 1$ ('K&V'), $\varphi_f = 0.8$, $\varphi_f = 0.2$, and hence different coefficient models, are tested for $K_f^\dagger = K_s^f/1750$, (a, b), and $K_f^\dagger = K_s^f/35$, (c, d).

thus has the effect of removing a pressure source from continuum α. Removal of this poroelastic coupling explains the lower than expected induced matrix and fracture pressures. Accordingly, these results and discussion provide an explanation for the results observed in Khalili (2003). Specifically, removal of the matrix pressure source explains the discontinuous pressure drop shown by the fracture phase in their Fig. 1. Additionally, removal of the fracture pressure sink explains the nonphysical pressure excitation shown by the matrix phase in their Fig. 1. Lastly, from Eq. (3.51) we can see $P_\alpha \propto E^{-1}$. Underestimated pressures therefore explain the over estimated strain in the current work when taking $Q^{-1} = 0$.

In contrast, Eq. (3.21) shows that although $A_{23} = 0$, $Q^{-1} \neq 0$. The pressures in each continuum therefore remain poroelastically coupled with respect to the

mixed compliance setting. This coupling explains why we still observe good matches when $A_{23} = 0$ versus the reference.

(a) Pressure

(b) Vertical strain, E_{yy}

Figure 3.5: Matrix ('M') and fracture ('F') pressure (a), and vertical strain (b) evolutions for the dual-continuum Mandel problem whilst considering macroscale assumptions $Q^{-1} = 0$ and $A_{23} = (A_{32}) = 0$. Results are referenced against the set of coefficient models from Khalili and Valliappan (1996) for which no assumptions have been made.

The current results suggest that assuming $A_{23} = 0$ is a reasonable implicit assumption to make. However, we advise caution when interpreting this result. Based on the results in this section it would be easy, and incorrect, to use them as a justification for assumptions made at the microscale. In Section 3.4 it was shown that explicit assumptions affect all of the constitutive coefficients due to bounds on bulk moduli. The remainder of this results section aims at qualitatively supporting these findings.

3.6.3 Case 3: Explicit decoupling - isostrain

Fig. 3.6 gives the results for the first isostrain test case. Specifically, we compare results between models parameterised by calculating K^* with the Voigt average (isostrain), the HS upper bound and an arbitrary value. Fig. 3.6a shows in the isostrain and HS upper bound cases, matrix pressure evolutions appear to be almost identical. However, for the case using $K^{*,†}$, the fracture pressures are significantly higher. Further, for this case the matrix pressures are slightly higher at early to middle times relative to the aforementioned upper bound cases. The contrast in fracture pressures is most pronounced between the isostrain and arbitrary effective bulk modulus cases. For the induced problem, different values of K^*, which go on to affect constitutive coefficient calculations, explain the differences in pressure by way of Eq. (3.52).

An alternative, heuristic approach to explaining the pressure distributions in Fig. 3.6a can be achieved by considering the required geometry that would be necessary to give a K^* that is lower than the Voigt average. Departure from this upper bound occurs when inclusions are arranged so as to weaken the host material. These inclusions then take on a greater portion of the distributed stress. As a result, we observe a greater induced fracture pressure when using a lower value of K^* compared to the Voigt bound, due to the proportionality between stress and pressure.

The early time vertical strains in Fig. 3.6b can be explained by way of Eq. (3.51) or through the heuristic argument. With the latter, towards the upper bounds of K^* the matrix supports the majority of deformation. Since the matrix is stiff, deformation is low. In contrast, when fractures are arranged such that they have a greater weakening effect on the host material, deformation is high.

At later times, vertical strain between both the upper bound and the $K^{*,\dagger}$ cases diverge. Towards the upper bounds for K^*, $B_f < B_m$. In the case of isostrain this fact is easily seen from the relations in Eqs. (3.33) to (3.34). The magnitude of B_m means that deformation is more strongly coupled to differences in matrix pressure relative to fracture pressure by way of momentum balance Eq. (3.48). This explains the growth in vertical strain separation at later times shown in Fig. 3.6b. Of further interest, considering these both represent upper bounds on the effective bulk modulus, is the difference in early time fracture pressures between the isostrain and HS upper bound cases. The early time fracture pressure associated with the HS upper bound is over double that of the isostrain case. This highlights the need for caution before making assumptions on the distribution of strain between constituents.

Fig. 3.7a displays the results for the incompressible grain isostrain investigation. For the case of coefficient models from Khalili and Valliappan (1996), the induced matrix pressure is significantly larger than the induced fracture pressure. Conversely, when using coefficient models from Borja and Koliji (2009) with the assumption $\partial\psi_\alpha/\partial t \approx 0$, induced matrix and fracture pressures are equal. This can be explained by considering Eq. (3.51) which allows us to equate induced variations in matrix and fracture pressures such that

$$
\left(\frac{1}{M_m} - \frac{M_f}{(Q)^2}\right)\left(\frac{M_f B_f}{Q} - B_m\right)^{-1} P_m
$$
$$
= \left(\frac{1}{M_f} - \frac{M_m}{(Q)^2}\right)\left(\frac{M_m B_m}{Q} - B_f\right)^{-1} P_f.
$$

(3.55)

(a) Pressure (b) Vertical strain, E_{yy}
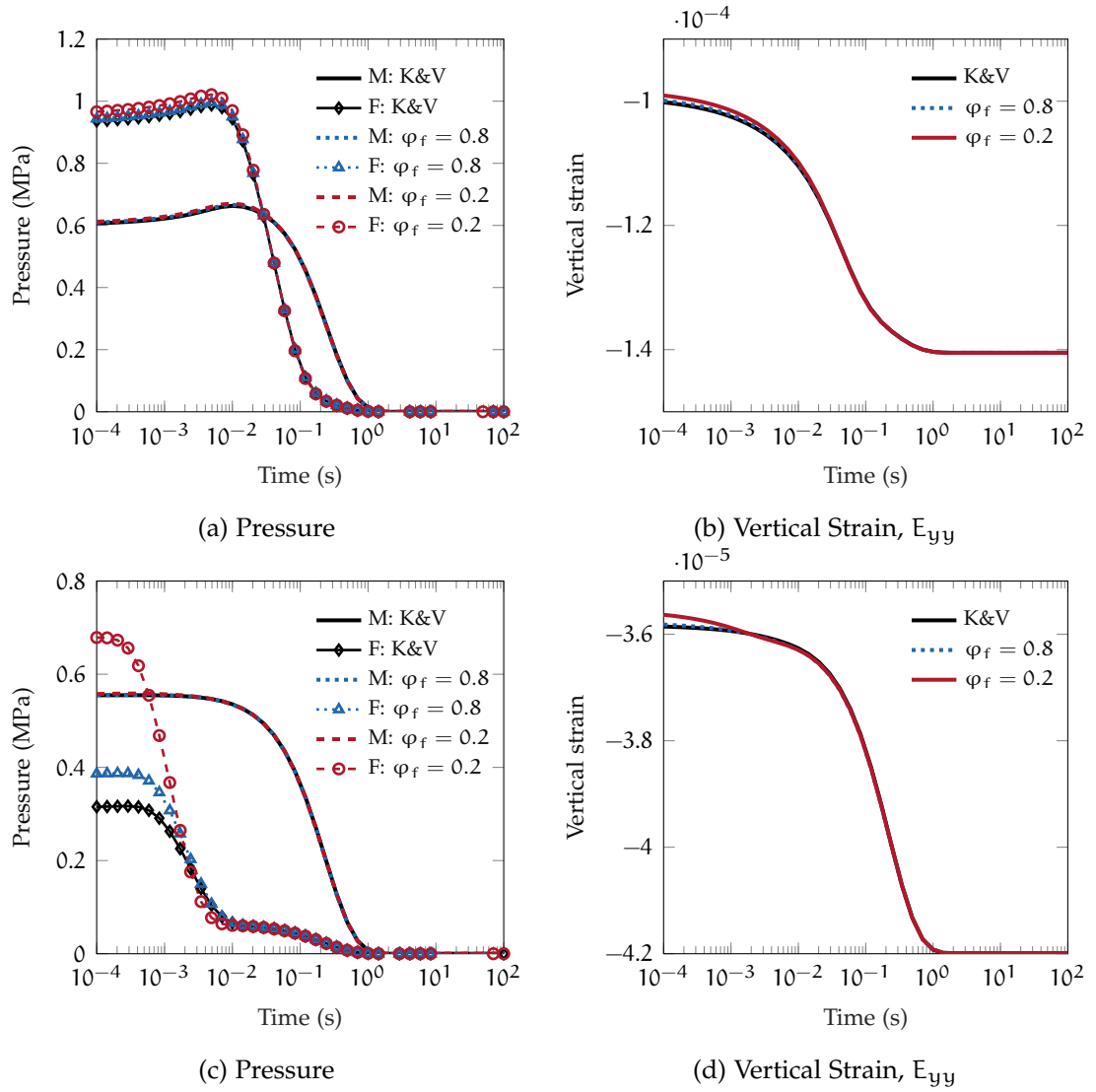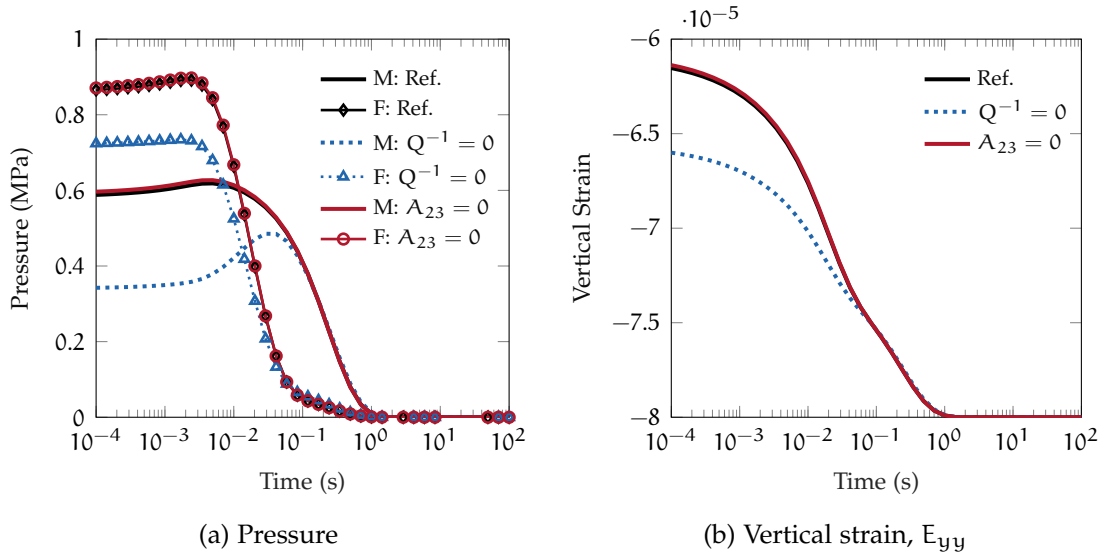
Figure 3.6: Matrix ('M') and fracture ('F') pressure (a), and vertical strain (b) evolutions for the dual-continuum Mandel problem considering isostrain. '$K^{\mathcal{V}}$' denotes coefficient models for which isostrain is assumed ($K^{\mathcal{V}} = 19.8$ GPa). '$K^{\mathcal{H}+}$' are models calculated using the upper Hashin-Shtrikman bound for $K^{\mathcal{H}+}$ (19.5 GPa). '$K^{*,\dagger}$' are coefficient models calculated with an arbitrary bulk modulus of 10 GPa.

Assuming $\partial\psi_\alpha/\partial t \approx 0$ together with the effective Biot coefficient expressions from Borja and Koliji (2009) (Table 3.1), Eq. (3.55) reduces to

$$\left(\frac{\phi_m^0}{K_l}\frac{1-\phi_s}{\phi_m^0}\right) P_m = \left(\frac{\phi_f^0}{K_l}\frac{1-\phi_s}{\phi_f^0}\right) P_f, \tag{3.56}$$

from which it is easy to see that $P_m = P_f$.

Under isostrain, we would expect the distribution of stress required to maintain strain uniformity between matrix and fractures to lead to disparate matrix and fracture pressures. The result $P_m = P_f$ therefore suggests that the closure condition $\partial\psi_\alpha/\partial t \approx 0$ may be an even stronger assumption than incompressible grain isostrain alone.

Fig. 3.7b shows vertical strain is lower at early times when using coefficient models from Khalili and Valliappan (1996) under incompressible grain isostrain. This can be explained by Eq. (3.51), which is affected by differences in B_α arising from each set of coefficient models.

In light of the discussions in Section 3.4.2 and the results presented herein, assuming $\partial\psi_\alpha/\partial t \approx 0$ appears to be a strong closure assumption to make. Thus, we suggest further development of a constitutive model for variations in ψ_α, along with its relationship to the constitutive model shown in Eqs. (3.5) to (3.7).

(a) Pressure

(b) Vertical strain, E_{yy}

Figure 3.7: Matrix ('M') and fracture ('F') pressure (a), and vertical strain (b) evolutions for the dual-continuum Mandel problem considering incompressible grain isostrain. 'K&V' and 'B&K' denote coefficient models associated with Khalili and Valliappan (1996) and Borja and Koliji (2009) respectively. The latter includes the assumption $\partial \psi_\alpha / \partial t \approx 0$. This allows us to map the effective stress model from Borja and Koliji (2009) onto the constitutive model Eqs. (3.5) to (3.7).

3.6.4 Case 4: Explicit decoupling - isostress

Fig. 3.8 gives the results for the isostress test case. From Fig. 3.8a, we see up-scaling methods leading to a stiffer homogenised bulk modulus lead to a lower induced fracture pressure. Subsequently, pressure diffusion occurs earlier in the same continuum. This is the case when using the arithmetic mean of the HS bounds. Non-monotonic rises in matrix and fracture pressures are more pronounced for more compliant heterogeneous materials. This is the case when assuming isotress (Reuss average) and the HS lower bound. Additionally, more compliant materials exhibit a faster decrease in matrix pressure at later times when compared to the stiffer modulus case.

Non-monotonic pressure rises are often referred to as the Mandel-Cryer effect within literature (Wang 2000; Cheng 2016). We predict that such rises lead to greater pressure differentials at middle to late times between the matrix and fracture domains. This would explain the higher rate of matrix pressure diffusion in the compliant material cases.

Fig. 3.8b shows pronounced distinctions in vertical strain for the three different upscaling cases. As expected, the (stiffer) arithmetic mean of the HS bounds shows the lowest deformation. Of more interest, considering that they both correspond to lower bounds, are the difference in strains between the cases of isostress and HS lower bound. Vertical strain at late times is approximately 75% larger when assuming isostress compared to when using the HS lower bound.
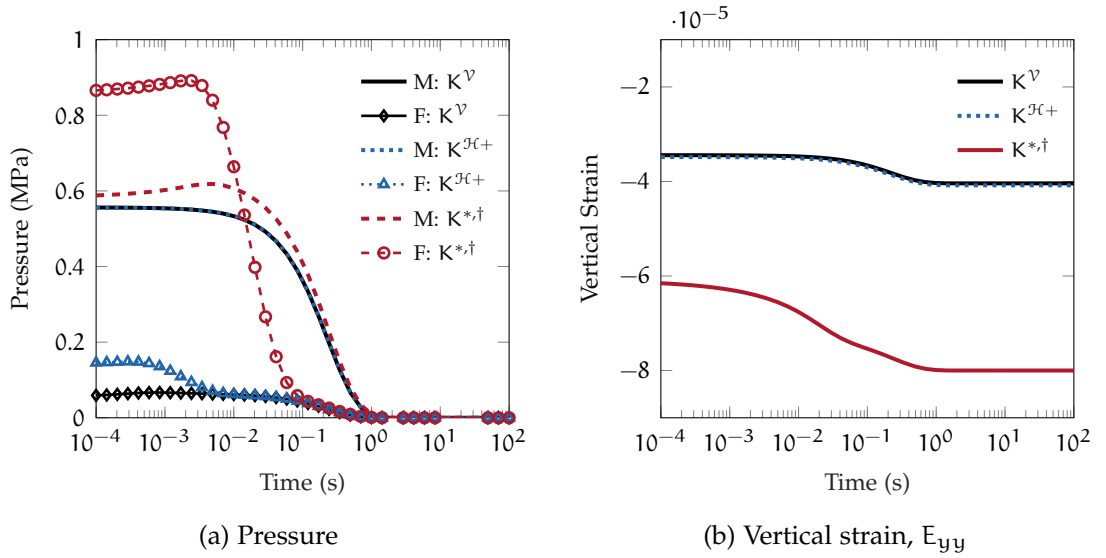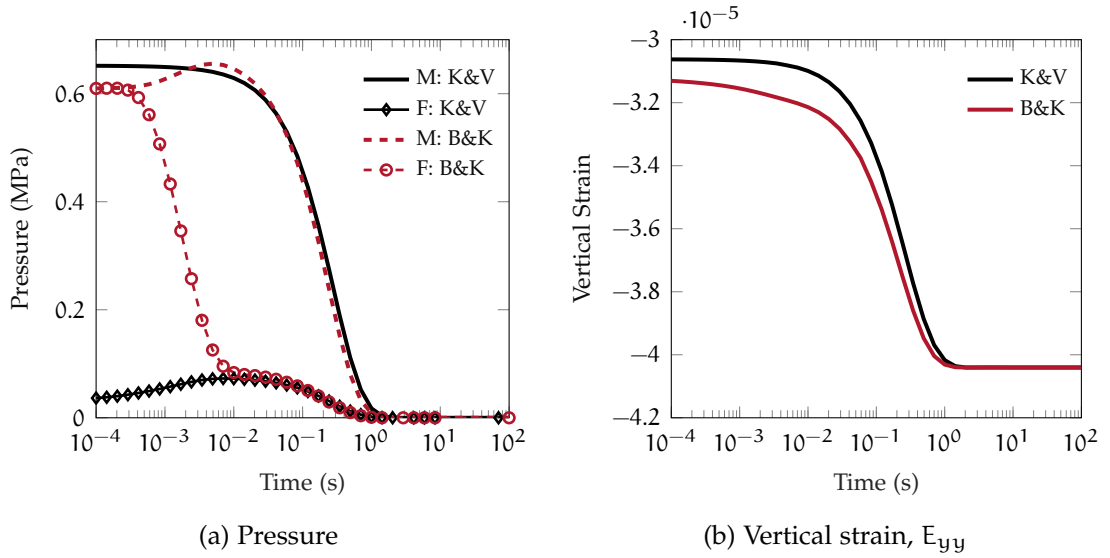
(a) Pressure · (b) Vertical strain, E_{yy}
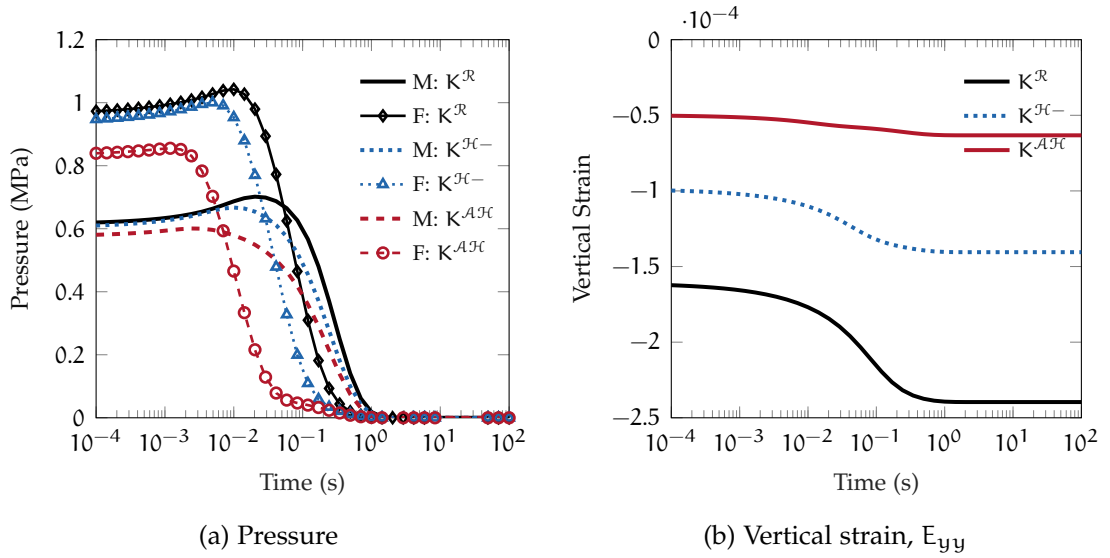
Figure 3.8: Matrix ('M') and fracture ('F') pressure (a), and vertical strain (b) evolutions for the dual-continuum Mandel problem whilst considering isostress (Reuss average) and other upscaling approaches. '$K^{\mathcal{R}}$' denotes coefficient models for which isostress is assumed ($K^{\mathcal{R}} = 3.3$ GPa). Notation '$K^{\mathcal{H}-}$' and '$K^{\mathcal{AH}}$' are models calculated using the lower Hashin-Shtrikman bound and the arimthmetic mean of the Hashin-Shtrikman bounds for K^* respectively (5.7 GPa and 12.7 GPa respectively).

The cause of the difference in vertical strains between the isostress and HS lower bound cases can be explained using similar discussions as to those used in Sections 3.6.2 and 3.6.3. First, using the heuristic argument the HS lower bound is higher than the Reuss bound suggesting that the matrix is capable of supporting a greater distribution of strain. This explains the difference in vertical strain at early times. Late time differences can be explained by the differences in fracture pressure. In contrast to Section 3.6.3, towards the lower bounds for K^*, $B_f > B_m$. The magnitude of B_f means that deformation is more strongly coupled to differences in fracture pressure relative to matrix pressure by way of momentum balance Eq. (3.48).

With a view toward multi-continuum generalisations, based on the results in Section 3.4.3 and the qualitative results herein we recommend care before assuming isostress. This stress distribution has strong geometrical implications that, without experimental substantiation to prove otherwise, would seem unlikely to hold within a multi-continuum material.

3.7 Conclusions

This chapter investigated the relationships between previously introduced constitutive models and the impacts of various methods of decoupling used within the literature. In summary, we identified three main modelling approaches. These approaches differ in the quantities, and/or modelling assumptions, used for the

calculation of the effective constitutive coefficients. The quantities and modelling assumptions used in these approaches are summarised as follows:

1. Constituent mechanical properties; assuming the high permeability, low storage continuum is all void space (no intrinsic fracture properties),

2. Constituent pore fractions; assuming the high permeability, low storage continuum is all void space,

3. Constituent mechanical properties, including intrinsic fracture properties.

With respect to 1. and 3. above, we showed how these previously introduced constitutive models are special cases of the one derived in Chapter 2.

Based on the findings in this chapter we recommend further work on algebraic closure conditions for models built using continuum pore fractions (type 2. models). Comparing coefficient models 1. and 3. we found the effects of intrinsic fracture properties become measurable when there are significant deviations from the intrinsic poroelastic constitutive coefficients of a void space fracture continuum. In this case $\varphi_f < 1$ and $K_f \lll K_s^f$, and it is advisable to use coefficient models where intrinsic fracture properties are naturally incorporated. We envisage the aforementioned conditions, and thus real benefit of using models type 3. models, to be observed when considering nonlinear poromechanics, where the internal structure of the high permeability, low storage continuum is evolving (e.g. fracture closure) thus leading to cases where $\varphi_f < 1$ and $K_f \lll K_s^f$. However, in the linear case, our results show models of type 1. give very good matches to models of type 3. even when $\varphi_f < 1$, provided $K_f \ll K_s^f$. Therefore as a first approach we recommend the use of type 1. models for poroelastic dual-continuum modelling given that we expect the high permeability, low storage continuum to be mechanically weaker than solid grains.

The second set of recommendations is formed on the basis of our investigations into implicit and explicit decoupling assumptions. In both cases mechanical coupling between continuum pressures is neglected. In the former we showed that implicit assumptions can lead to the removal of pressure sources leading to physically unreliable results. We therefore recommend the use of a full constitutive system where possible.

Even with a full constitutive system, explicit assumptions have been made as a passage to simplifying relations between effective and constituent moduli without considering the physical implications of their use. In this case we showed that explicit decoupling assumptions are coincident with bounds on effective moduli that arise naturally under end-member states of isostrain and isostress. However, for isotropic heterogeneous materials it is well known that the bounds obtained under isostrain and isostress can be loose, and that tighter

bounds using similar quantities are readily available within literature. Our qualitative investigations showed clear differences in poroelastic behaviour when using these different bounds.

To conclude, bounds arising from isostrain and isostress states, which are concurrent with explicit decoupling assumptions, can provide a useful means for guiding our intuition into multiscale poroelastic behaviour, given their ease of computation. However, for practical subsurface applications, we recommend against the use of explicit decoupling assumptions. Specifically, these assumptions have physical and geometrical implications that are unlikely to be justified within isotropic multiscale materials.

Part II

Numerical modelling

Numerical modelling framework

In this chapter we provide the details of the framework used for the numerical modelling of poroelastic dual-continua. In Section 4.1, starting from equations introduced in the first chapter, we give the discrete set of equations that encompass the numerical framework used herein. In doing, we introduce the various discretisation and solution strategies necessary for our numerical approach. In Section 4.2, we benchmark our code against the analytical solutions for the poroelastic model problem introduced in the third chapter. In Section 4.3, we then demonstrate the flexibility of the modelling approach on a non-conforming geological grid. In Section 4.4, we summarise this chapter whilst offering recommendations for future work. The contents of this chapter are based on work done in Ashworth and Doster (2019a) and Ashworth and Doster (2020). Finally, the framework in this chapter has been written as a module for the open-source MATLAB *Reservoir Simulation Toolbox (Lie 2019). The contents of the module can be found in:*

`https://bitbucket.org/mashworth92/dual-continuum-mech`

4.1 Numerical framework

Within the reservoir simulation community, the numerical modelling of coupled flow and deformation processes is generally done using dedicated software for each subproblem. For flow, the finite-volume method (FVM) is typically used, and for deformation (mechanics) the finite-element method (FEM). The former guarantees local mass conservation whilst the latter is naturally suited for the discretisation of the self-adjoint mechanical problem. For flow problems the mass conservation property is attractive. In particular, for highly permeable media such as a fractures there is significant potential for discontinuities at sharp pressure interfaces (e.g. a drainage boundary) (Yoon and Kim 2018). Coupling different software is an important consideration and is the goal behind sequential coupling strategies (Kim et al. 2009). Alternatively, provided we have easy access to the full multiphysics system of equations, we can solve the system monolithically (fully coupled). To date, the vast majority of poroelastically coupled dual-continuum implementations have been fully coupled finite-element codes

(Lewis and Ghafouri 1997; Bai et al. 1999; Khalili et al. 2000; Pao and Lewis 2002; Fornells et al. 2007; Choo and Borja 2015; Choo et al. 2016).

The heterogeneous nature of subsurface geology makes the use of unstructured grids desirable to honour complex features such as faults and explicitly defined fractures (Karimi-Fard et al. (2003); Prévost et al. (2005)). However, in FEM the user is limited by the availability of basis functions, which for general polyhedral cells are restricted to certain geometries or require costly computation (Chi et al. 2017). A generalisation of FEM to general polygonal and polyhedral cells called the Virtual Element Method (VEM) has been introduced (Beirão da Veiga et al. 2013, 2014). In this, the basis functions are never explicitly called. Instead the method is understood entirely through its degrees of freedom, which are well defined. This feature makes VEM an attractive discretisation for mechanical problems on grids which would otherwise challenge the basis function requirements in FEM.

With the benefits of FVM for flow and VEM for mechanical problems on complex grids, a hybrid FVM-VEM framework has been previously introduced by Andersen et al. (2017a,b), for single-porosity materials. In this chapter we extend this framework to dual-continuum materials. Accordingly, we introduce the key components of the framework therein, benchmark it against analytical solutions, and test it on a geological grid.

4.1.1 Strong form

To start, we consider the conservation statements Eqs. (2.2) to (2.4) introduced in Section 2.2. Introducing the constitutive relations from the remainder of Chapter 2 into these balance laws, whilst also maintaining the assumptions introduced in Section 2.2, leads to the following set of equations

$$\nabla \cdot (\mathbb{C}^* : \mathbf{E} - \mathbf{B}_m P_m - \mathbf{B}_f P_f) = 0, \tag{4.1}$$

$$\frac{\partial}{\partial t} \left(\mathbf{B}_m : \mathbf{E} + \frac{P_m}{M_m} + \frac{P_f}{Q} \right) - \nabla \cdot \left(\frac{\mathbf{K}_m}{\mu_l} \cdot \nabla P_m \right) = \frac{\varkappa k'}{\mu_l}(P_f - P_m) + \Psi_m, \tag{4.2}$$

$$\frac{\partial}{\partial t} \left(\mathbf{B}_f : \mathbf{E} + \frac{P_m}{Q} + \frac{P_f}{M_f} \right) - \nabla \cdot \left(\frac{\mathbf{K}_f}{\mu_l} \cdot \nabla P_f \right) = \frac{\varkappa k'}{\mu_l}(P_m - P_f) + \Psi_f, \tag{4.3}$$

where we have included volumetric source terms Ψ_α for continuum α and assume isotropy of the underlying matrix material.

We consider the conservation equations over a domain, $\Omega^{\mathcal{D}} \subset \mathbb{R}^d$ bounded by $\partial\Omega^{\mathcal{D}}$. The domain boundary is separated into disjoint boundary segments corresponding to Dirichlet and Neumann boundary conditions for the mechanical and flow problems. For the mechanical problem this implies displacement (Γ^u) and traction (Γ^t) boundary conditions. To ensure well-posedness $\Gamma^u \cup \Gamma^t = \partial\Omega^{\mathcal{D}}$

and $\Gamma^u \cap \Gamma^t = \varnothing$. For the flow problem the boundary conditions for a given continuum are pressure (Γ^p_α) and flux (Γ^q_α). Again, for a well-posed problem we have $\Gamma^p_\alpha \cup \Gamma^q_\alpha = \partial \Omega^{\mathcal{D}}$ and $\Gamma^p_\alpha \cap \Gamma^q_\alpha = \varnothing$.

The strong form is finally defined as: Find $\mathbf{U}$, P_m and P_f that satisfy Eqs. (4.1) to (4.3) subject to boundary conditions:

$$\mathbf{U} = \hat{\mathbf{U}} \quad \text{on } \Gamma^u, \tag{4.4}$$

$$\boldsymbol{\Sigma} \cdot \mathbf{n} = \hat{\mathbf{T}} \quad \text{on } \Gamma^t, \tag{4.5}$$

$$P_m = \hat{P}_m \quad \text{on } \Gamma^p_m, \tag{4.6}$$

$$\mathbf{q}_m \cdot \mathbf{n} = \hat{q}_m \quad \text{on } \Gamma^q_m, \tag{4.7}$$

$$P_f = \hat{P}_f \quad \text{on } \Gamma^p_f, \tag{4.8}$$

$$\mathbf{q}_f \cdot \mathbf{n} = \hat{q}_f \quad \text{on } \Gamma^q_f, \tag{4.9}$$

with initial conditions

$$\mathbf{U} = \mathbf{U}^0, \quad P_m = P^0_m, \quad P_f = P^0_f, \tag{4.10}$$

for all $(\mathbf{X}, t) \in (\Omega^{\mathcal{D}} \times t = 0)$.

The single-porosity linear poroelastic model can be recovered from Eqs. (4.1) to (4.10) under the assumption $P = P_m = P_f$ and combining Eq. (4.2) and Eq. (4.3).

4.1.2 Weak form

The weak formulation of the strong form introduced previously requires the definition of the appropriate function spaces. Accordingly, solution spaces for continuum pressure and the displacements are $\mathcal{S}_{P_\alpha} = L^2(\Omega^{\mathcal{D}})$ and $\mathcal{S}_{\mathbf{U}} = \{\mathbf{U} \in H^1(\Omega^{\mathcal{D}})^d : \mathbf{U} = \hat{\mathbf{U}} \text{ on } \Gamma^u\}$ respectively, where L^2 and H^1 are the typical square integrable and first-order Sobolev function spaces. Weighting function spaces are then defined as $\mathcal{W}_{P_\alpha} = L^2(\Omega^{\mathcal{D}})$ and $\mathcal{W}_{\mathbf{U}} = \{\boldsymbol{\eta} \in H^1(\Omega^{\mathcal{D}})^d : \boldsymbol{\eta} = 0 \text{ on } \Gamma^u\}$.

To progress, we compare trial functions against weight functions, leading to the weak form defined as: Find $(\mathbf{U}, P_m, P_f) \in (\mathcal{S}_{\mathbf{U}} \times \mathcal{S}_{P_m} \times \mathcal{S}_{P_f})$ such that for all $(\boldsymbol{\eta}, \omega_m, \omega_f) \in (\mathcal{W}_{\mathbf{U}} \times \mathcal{W}_{P_m} \times \mathcal{W}_{P_f})$

$$g(\boldsymbol{\eta}, \mathbf{U}) - \int_{\Omega^{\mathcal{D}}} (\nabla \boldsymbol{\eta}) \cdot \mathbf{B}_m P_m \, dV - \int_{\Omega^{\mathcal{D}}} (\nabla \boldsymbol{\eta}) \cdot \mathbf{B}_f P_f \, dV$$

$$= \int_{\Gamma^t} \boldsymbol{\eta} \cdot \hat{\mathbf{T}} \, dS, \tag{4.11}$$

$$\int_{\Omega^{\mathcal{D}}} \frac{\partial}{\partial t} \omega_m \left(\mathbf{B}_m : \underline{\nabla} \mathbf{U} + \frac{P_m}{M_m} + \frac{P_f}{Q} \right) \, dV$$

$$-\int_{\Omega^{\mathcal{D}}} \omega_m \nabla \cdot \left(\frac{\mathbf{K}_m}{\mu_l} \cdot \nabla P_m \right) \, dV = \int_{\Omega^{\mathcal{D}}} \omega_m \frac{\varkappa k'}{\mu_l} (P_f - P_m) + \omega_m \Psi_m \, dV,$$

$$\tag{4.12}$$

$$\int_{\Omega^{\mathcal{D}}} \frac{\partial}{\partial t} \omega_f \left(\mathbf{B}_f : \underline{\nabla} \mathbf{U} + \frac{P_m}{Q} + \frac{P_f}{M_f} \right) \, dV$$

$$-\int_{\Omega^{\mathcal{D}}} \omega_f \nabla \cdot \left(\frac{\mathbf{K}_f}{\mu_l} \cdot \nabla P_f \right) \, dV = \int_{\Omega^{\mathcal{D}}} \omega_f \frac{\varkappa k'}{\mu_l} (P_m - P_f) + \omega_f \Psi_f \, dV. \tag{4.13}$$

The bilinear form $g(\cdot, \cdot)$ in Eq. (4.11) is given by

$$g(\boldsymbol{\eta}, \mathbf{U}) = \int_{\Omega^{\mathcal{D}}} \underline{\nabla} \boldsymbol{\eta} : \boldsymbol{\Sigma}'(\mathbf{U}) \, dV, \tag{4.14}$$

where $\boldsymbol{\Sigma}'(\mathbf{U}) = \mathbf{C}^* : \underline{\nabla} \mathbf{U}$.

4.1.3 Discrete block matrix form

The discrete counterpart to Eqs. (4.11) to (4.13) is formulated using FVM for flow, VEM for mechanics, and the backward Euler method for time. This hybrid FVM-VEM numerical approach to poroelasticity was originally developed using the MATLAB Reservoir Simulation Toolbox (MRST) (Lie et al. 2012; Lie 2019), by Andersen et al. (2017a,b) for single-continuum materials. Here we expand the work by these latter authors to dual-continuum materials.

We partition our domain into disjoint elements (or cells). Subsequently, for the DC problem $\Omega^{\mathcal{D}} = \cup_{j=1}^{n_{elem}} \Omega_j^{\mathcal{D}}$, where n_{elem} is the number of elements. Notation $\Omega_j^{\mathcal{D}}$ denotes the dual-continuum element for which there are *two* pressure degrees of freedom, corresponding to each continuum.

We define the following discrete solution spaces for the DC problem as $\mathcal{S}_{P_\alpha}^h \subset \mathcal{S}_{P_\alpha}$ and $\mathcal{S}_U^h \subset \mathcal{S}_U$. Discrete weighting spaces are given as $\mathcal{W}_{P_\alpha}^h \subset \mathcal{W}_{P_\alpha}$ and $\mathcal{W}_U^h \subset \mathcal{W}_U$. Discrete continuum pressure fields $P_\alpha^h \in \mathcal{S}_{P_\alpha}^h$ and discrete displacement fields $\mathbf{U}^h \in \mathcal{S}_U^h$ are given according to the following interpolation relations respectively

$$P_\alpha^h = \sum_{j=1}^{n_{elem}} \mathcal{J}^j \tilde{P}_\alpha^j, \tag{4.15}$$

$$\mathbf{U}^h = \sum_{b=1}^{n_{node}} \mathcal{N}^b \tilde{U}^b, \tag{4.16}$$

where n_{node} denotes the total number of vertices associated to element j. Notations $\tilde{P}_\alpha^j$ and $\tilde{U}^b$ are pressure and displacement degrees of freedom respectively, with the corresponding basis functions denoted by $\mathcal{J}^j$ and $\mathcal{N}^b$.

In FVM we consider $\tilde{P}_\alpha^j$ to be cell-centred quantities. Notation $\mathbb{J}^j$ is then an indicator function for continuum α given as

$$\mathbb{J}^j(\mathbf{X}) = \begin{cases} 1 & \text{if } \mathbf{X} \text{ in } \Omega_j^{\mathcal{D}} \\ 0 & \text{otherwise} \end{cases}, \tag{4.17}$$

Further, we replace discrete pressure weight functions $\omega_\alpha^h \in \mathcal{W}_{P_\alpha}^h$ by the indicator function whilst also using Eq. (4.15) such that Eqs. (4.12) to (4.13) can be interpreted as element-wise conservation statements. Using Gauss's theorem, element-wise divergence of flux volume integrals in Eqs. (4.12) to (4.13), are turned into face-wise surface integrals. In this work we use the two-point flux approximation to calculate these face-wise flux integrals (see Lie (2019) for further details).

The nodal basis function matrix $\mathcal{N}^b$ takes the identity matrix $\mathbf{1}$ when located at node b and $\mathbf{0}$ at all other nodes. Next, we introduce the following relation between global and element-wise bilinear forms as is customary for finite-element procedures

$$g(\boldsymbol{\eta}^h, \mathbf{U}^h) = \sum_{j=1}^{n_{elem}} g_j(\boldsymbol{\eta}^h, \mathbf{U}^h). \tag{4.18}$$

On regular grids one can compute $g_j(\boldsymbol{\eta}^h, \mathbf{U}^h)$ exactly for first-order finite-element methods, since basis functions used to interpolate the solution are known. However, on general grids, such basis functions are limited in their availability, and are in general, non-polynomial functions (Gain et al. 2014). This can make using quadrature formulas prohibitively expensive. In contrast, for VEM the basis functions are never explicitly defined, and thus $g_j(\boldsymbol{\eta}^h, \mathbf{U}^h)$ is never explicitly computed. Due to the former, VEM can be interpreted as a generalisation of the finite-element method to arbitrary polygonal and polyhedral meshes. Such a property is desirable for subsurface modelling, where degenerate cells and hanging nodes are encountered (Andersen et al. 2017b). Instead the idea is to approximate $g_j(\boldsymbol{\eta}^h, \mathbf{U}^h) \approx g_j^h(\boldsymbol{\eta}^h, \mathbf{U}^h)$, whilst ensuring the order of accuracy is maintained. To go into the details of VEM is beyond the scope of this work. For more details the interested reader is directed towards the works of Beirão da Veiga et al. (2013, 2014), and for elasticity Gain et al. (2014) and Andersen et al. (2017b). Nonetheless, it is useful to gain some insight into the method. Accordingly, we give an heuristic interpretation of VEM for which we consider only piecewise linear fields over each element. We define the following expression for the construction of $g_j^h(\boldsymbol{\eta}^h, \mathbf{U}^h)$ by way of VEM,

$$g_j^h(\boldsymbol{\eta}^h, \mathbf{U}^h) = g_j(\boldsymbol{\pi}\boldsymbol{\eta}^h, \boldsymbol{\pi}\mathbf{U}^h) + s_j[(\boldsymbol{\eta}^h - \boldsymbol{\pi}\boldsymbol{\eta}^h), (\mathbf{U}^h - \boldsymbol{\pi}\mathbf{U}^h)], \tag{4.19}$$

where $\boldsymbol{\pi}$ is a local projection operator. The use of a projection operator is fundamental to VEM. Next, we define the following local virtual element space

$$\mathcal{V}_j^h = \{\mathbf{V} \in H^1(\Omega_j^{\mathcal{D}})^d : \nabla^2 \mathbf{V} = 0 \text{ in } \Omega_j^{\mathcal{D}}, \ \mathbf{V}|_\Gamma \in \mathcal{P}(\Gamma)_1^d \ \forall \Gamma \in \partial\Omega_j^{\mathcal{D}}\}, \qquad (4.20)$$

where $\mathcal{P}(\Gamma)_1^d$ is the space of linear displacements on the edge Γ. Further, $\mathbf{U}^h \in \mathcal{V}_j^h$. The projection operator then acts to extract the linear displacements over an element, belonging to the subspace $\mathcal{P}(\Gamma)_1^d \subset \mathcal{V}_j^h$ from the virtual element space $\mathcal{V}_j^h$. This operation is exactly what is defined when computing the projection in $g_j(\boldsymbol{\pi}\boldsymbol{\eta}^h, \boldsymbol{\pi}\mathbf{U}^h)$. The first term on the right hand side of Eq. (4.19) therefore ensures that the polynomial consistency of the method is fulfilled with respect to linear fields. In engineering literature, methods that are consistent with the desired degree of accuracy imply satisfaction of the patch test (Taylor et al. 1986). In extracting first-order terms from the displacement field we 'leave behind' higher-order and/or non-polynomial terms. The second term in Eq. (4.19), i.e. $s_j(\cdot, \cdot)$, ensures the stability of the method with respect to these terms. Specifically, that the discrete problem inherits the coercivity of the continuous problem. In Beirão da Veiga et al. (2013) and Gain et al. (2014) it is noted that $s_j(\cdot, \cdot)$ need only be approximated to ensure stability.

Computation of the element-wise bilinear forms $g_j(\boldsymbol{\pi}\boldsymbol{\eta}^h, \boldsymbol{\pi}\mathbf{U}^h)$ and $s_j[(\boldsymbol{\eta}^h - \boldsymbol{\pi}\boldsymbol{\eta}^h), (\mathbf{U}^h - \boldsymbol{\pi}\mathbf{U}^h)]$ can be found in Gain et al. (2014) and Andersen et al. (2017b). Finally, as part of the VEM assembly, the constitutive relation Eq. (4.14) need only be computed once, similar to a one-point quadrature finite-element scheme (Da Veiga et al. 2015).

Replacing solutions and weighting functions with their discrete counterparts, and using the time discretisation, the discrete residual equations from Eqs. (4.11) to (4.13) are

$$\mathbf{R}_U^a = g^h(\mathcal{N}^a, \mathbf{U}^{h,t+1}) - \int_{\Omega^{\mathcal{D}}} (\nabla \mathcal{N}^a) \cdot \mathbf{B}_m P_m^{h,t+1} \ dV$$

$$- \int_{\Omega^{\mathcal{D}}} (\nabla \mathcal{N}^a) \cdot \mathbf{B}_f P_f^{h,t+1} \ dV - \int_{\Gamma^t} \mathcal{N}^a \cdot \hat{\mathbf{T}} \ dS$$

$$= 0, \quad \forall a = 1, ..., n_{node}, \qquad (4.21)$$

$$R_{P_m}^i = \int_{\Omega_i^{\mathcal{D}}} \mathbf{B}_m \cdot \Delta(\underline{\nabla}\mathbf{U}^{h,t+1}) + \frac{1}{M_m}\Delta P_m^{h,t+1} + \frac{1}{Q}\Delta P_f^{h,t+1} \ dV$$

$$- \Delta t \int_{\partial\Omega_i^{\mathcal{D}}} \left(\frac{\mathbf{K}_m}{\mu_l} \cdot \nabla P_m^{h,t+1}\right) \cdot \mathbf{n}_i \ dS$$

$$- \Delta t \int_{\Omega_i^{\mathcal{D}}} \frac{\varkappa k'}{\mu_l}(P_f^{h,t+1} - P_m^{h,t+1}) + \Psi_m \ dV$$

$$= 0, \quad \forall i = 1, ..., n_{elem}, \qquad (4.22)$$

$$R^i_{P_f} = \int_{\Omega^{\mathcal{D}}_i} \mathbf{B}_f \cdot \Delta(\underline{\nabla}\mathbf{U}^{h,t+1}) + \frac{1}{Q}\Delta P^{h,t+1}_m + \frac{1}{M_f}\Delta P^{h,t+1}_f \ dV$$

$$- \Delta t \int_{\partial\Omega^{\mathcal{D}}_i} \left(\frac{\mathbf{K}_f}{\mu_l} \cdot \nabla P^{h,t+1}_f\right) \cdot \mathbf{n}_i \ dS$$

$$- \Delta t \int_{\Omega^{\mathcal{D}}_i} \frac{\varkappa k'}{\mu_l}(P^{h,t+1}_m - P^{h,t+1}_f) + \Psi_f \ dV$$

$$= 0, \quad \forall i = 1, ..., n_{elem}, \tag{4.23}$$

where we make use of Voigt notation for tensor representation. Notation $\Delta z^{t+1} = z^{t+1} - z^t$. Details of the VEM calculations for the boundary and gradient terms involving $\mathcal{N}^a$ in Eq. (4.21) can be found in Andersen et al. (2017b). To compute the flux terms in Eqs. (4.22) to (4.23), the surface integrals are computed as a face-wise summations such that

$$\int_{\partial\Omega^{\mathcal{D}}_i} \left(\frac{\mathbf{K}_m}{\mu_l} \cdot \nabla P^{h,t+1}_\alpha\right) \cdot \mathbf{n}_i \ dS = \sum_{j=1}^{n_{face}} \int_{\Gamma_{ij}} \left(\frac{\mathbf{K}_m}{\mu_l} \cdot \nabla P^{h,t+1}_\alpha\right) \cdot \mathbf{n}_i \ dS, \tag{4.24}$$

where n_{face} denotes the total number of faces associated to element i. The face-wise summation in Eq. (4.24) can then be computed according to various flux approximation schemes such as the two-point or multipoint flux approximations (Lie 2019).

Even though we assume linearity in the current work, poroelastic problems are generally nonlinear due to material and geometric nonlinearities. For example, one common example of the former nonlinearity type is stress-dependent permeability. To provide a general numerical framework we therefore present the discrete equations describing the DC problem following application of Newton's method. In MRST this is handled naturally using an automatic differentiation framework to generate the Jacobian. We give the discrete system of equations in block matrix form as

$$\begin{bmatrix} \mathbf{K} & -\mathbf{L}^\top_m & -\mathbf{L}^\top_f \\ \mathbf{L}_m & \mathbf{F}_m & \mathbf{G}_m \\ \mathbf{L}_f & \mathbf{G}_f & \mathbf{F}_f \end{bmatrix}^{(k)} \begin{bmatrix} \delta\tilde{\mathbf{U}} \\ \delta\tilde{\mathbf{P}}_m \\ \delta\tilde{\mathbf{P}}_f \end{bmatrix}^{t+1,(k+1)} = - \begin{bmatrix} \mathbf{R}_U \\ \mathbf{R}_{P_m} \\ \mathbf{R}_{P_f} \end{bmatrix}^{t+1,(k)}, \tag{4.25}$$

where $\mathbf{R}_U = [\mathbf{R}^1_U, ..., \mathbf{R}^{n_{node}}_U]^\top$ and $\mathbf{R}_{P_\alpha} = [\mathbf{R}^1_{P_\alpha}, ..., \mathbf{R}^{n_{elem}}_{P_\alpha}]^\top$. Notations δ and k denote the change in solution and current iteration levels respectively. Further,

$\tilde{\mathbf{U}} = [\tilde{\mathbf{U}}^1, ..., \tilde{\mathbf{U}}^{n_{node}}]^\top$ and $\tilde{\mathbf{P}}_\alpha = [\tilde{\mathbf{P}}_\alpha^1, ..., \tilde{\mathbf{P}}_\alpha^{n_{elem}}]^\top$ with the solution at level k re-related to the solution at k + 1 by the change in solution as

$$\begin{bmatrix} \tilde{\mathbf{U}} \\ \tilde{\mathbf{P}}_m \\ \tilde{\mathbf{P}}_f \end{bmatrix}^{t+1,(k)} + \begin{bmatrix} \delta\tilde{\mathbf{U}} \\ \delta\tilde{\mathbf{P}}_m \\ \delta\tilde{\mathbf{P}}_f \end{bmatrix}^{t+1,(k+1)} \longrightarrow \begin{bmatrix} \tilde{\mathbf{U}} \\ \tilde{\mathbf{P}}_m \\ \tilde{\mathbf{P}}_f \end{bmatrix}^{t+1,(k+1)} . \tag{4.26}$$

Finally, the individual matrices comprising the Jacobian in Eq. (4.25) are given as

$$\mathbf{K}_{ab} = \frac{\partial \mathbf{R}_{\tilde{U}}^a}{\partial \tilde{\mathbf{U}}^b} = g^h(\mathbf{N}^a, \mathbf{N}^b), \tag{4.27}$$

$$\mathbf{L}_{ib,\alpha} = \frac{\partial R_{P_\alpha}^i}{\partial \tilde{\mathbf{U}}^b} = \int_{\Omega^\mathcal{D}} \mathcal{I}^i(\mathbf{X}_i) \mathbf{B}_\alpha \cdot \nabla \mathbf{N}^b \, dV, \tag{4.28}$$

$$\mathbf{G}_{ij,\alpha} = \frac{\partial R_{P_\alpha}^i}{\partial \tilde{P}_\beta^j} = \int_{\Omega^\mathcal{D}} \mathcal{I}^i(\mathbf{X}_i) \frac{1}{Q} \mathcal{I}^j(\mathbf{X}_i) \, dV$$

$$- \Delta t \int_{\Omega^\mathcal{D}} \mathcal{I}^i(\mathbf{X}_i) \frac{\varkappa k'}{\mu_l} \mathcal{I}^j(\mathbf{X}_i) \, dV, \tag{4.29}$$

$$\mathbf{F}_{ij,\alpha} = \frac{\partial R_{P_\alpha}^i}{\partial \tilde{P}_\alpha^j} = \int_{\Omega^\mathcal{D}} \mathcal{I}^i(\mathbf{X}_i) \frac{1}{M_\alpha} \mathcal{I}^j(\mathbf{X}_i) \, dV$$

$$+ \Delta t \int_{\Omega^\mathcal{D}} \mathcal{I}^i(\mathbf{X}_i) \frac{\varkappa k'}{\mu_l} \mathcal{I}^j(\mathbf{X}_i) \, dV + \Delta t \mathbf{T}_{ij,\alpha}, \tag{4.30}$$

where $\mathbf{X}_i$ denotes the centroid of element $\Omega_i^\mathcal{D}$. Notation $\mathbf{T}_{ij,\alpha}$ is the transmissibility matrix for continuum α arising from the two-point flux approximation (Lie 2019), such that we obtain the following discrete relation

$$\sum_{j=1}^{n_{face}} \int_{\Gamma_{ij}} \left(\frac{\mathbf{K}_m}{\mu_l} \cdot \nabla P_\alpha^{h,t+1} \right) \cdot \mathbf{n}_i \, dS = \mathbf{T}_{ij,\alpha}(\tilde{P}_\alpha^i - \tilde{P}_\alpha^j). \tag{4.31}$$

4.1.4 Solution

We solve Eq. (4.25) using a fully coupled approach (Lewis and Schrefler 1998), although extensions to sequential solution strategies for DC materials have been shown in Kim et al. (2012).

4.2 Analytical benchmark

For single-continuum poroelastic codes the Mandel problem is the canonical method of code verification (e.g. Kim et al. 2009; Jha and Juanes 2014). Accord-

ingly, we validate our framework against the dual-continuum Mandel problem introduced in the previous chapter.

4.2.1 Problem setup and data

The problem geometry is as described in Section 3.5.1. Specifically, we consider a quarter of $2\,\text{m} \times 2\,\text{m}$ domain subjected to a constant top boundary force of $-2\,\text{MPa}\cdot\text{m}$ on this quarter (Fig. 3.3).

We consider isotropy at the macroscopic scale, as well as void-space fractures. Consequently, the poroelastic constitutive model introduced in Chapter 2 reduces to the Khalili and Valliappan (1996) constitutive model introduced in Chapter 3. Next, we assume dual-porosity materials meaning the macroscopic matrix permeability is zero with (macroscopic) transport taking place solely through the fractures. The fluid properties are given as $\rho_l^0 = 1000\,\text{kgm}^{-3}$, $\mu_l = 1\,\text{cp}$, and $K_l = 2.5\,\text{GPa}$. Matrix properties are given as $\phi_m^0 = 0.1$, $\nu_m = 0.995$, $k_m = k' = 0.01\,\text{md}$. Fracture properties are given as $\phi_f^0 = 5 \times 10^{-3}$, $\phi_f^0 = 5 \times 10^{-3}$, $\ell = 0.03\,\text{m}$, and $K_f = 1000\,\text{md}$. Finally, mechanical properties are assigned as $K_m = 20\,\text{GPa}$, $K_s = 70\,\text{GPa}$, and $\nu^* = 0.2$. K^* is chosen arbitrarily as $K^* = 10\,\text{GPa}$.

For the numerical domain we use a 20×20 Cartesian mesh. The observation point for the solutions is then located in the first grid cell, with cell ordering progressing from left to right, bottom to top.

One of the challenges when verifying code against the Mandel problem is ensuring the boundary conditions in the numerical problem are consistent with the rigid boundary conditions specified in the analytical solution. Instead of imposing a rigid plate directly within the numerical domain, we do this implicitly. Specifically, we use analytical solutions for the vertical stress along Γ_N (Appendix B). Accordingly, the vertical stresses are calculated at every spatial point corresponding to the locations of the vertices along this top boundary. At each time-step we then update the boundary conditions corresponding to Γ_N with the corresponding nodal stresses coming from the analytical solution. We then compare numerical continuum pressure and vertical strain results to those coming from the analytical solutions.

We note that under plane strain, the stiffness tensor written in Voigt notation is given as

$$\mathbb{C} = \frac{E}{(1+\nu)(1-2\nu)} \begin{bmatrix} 1-\nu & \nu & 0 \\ & 1-\nu & 0 \\ \text{sym} & & G \end{bmatrix} \tag{4.32}$$

where the shear modulus $G = E/(2(1+\nu))$, in which E is the Young's modulus. From Eq. (4.32) it follows

$$4K = \mathbf{1} : \mathbb{C} : \mathbf{1} = \frac{2E}{(1+\nu)(1-2\nu)}. \tag{4.33}$$

4.2.2 Results

Fig. 4.1 shows the pressure and vertical strain results for the analytical benchmark problem described above. The numerical results are taken from the first grid cell in the discretised domain. In Fig. 4.1a, we see the induced fracture pressure is significantly higher than the induced matrix pressure. Following a slight rise from early to middle times (Mandel-Cryer effect), fracture pressure decreases rapidly. This rapid diffusion is followed by a steady decrease of matrix pressure. In Fig. 4.1b, we see a steep increase in vertical strain associated with the drainage of the fractures. This period is followed by a steadier increase in strain due to the drainage of the (stiffer) matrix.

Importantly, Fig. 4.1 shows there is a good match between the analytical and numerical solutions. Slight discrepancies between the two can be observed in the pressure and vertical strain results between middle to late times. This could be caused by numerical errors or due to not using enough Fourier series terms in the analytical solution (Appendix B). Nonetheless, the quality of match between the analytical and numerical solutions is good enough for us to proceed.

(a) Pressure

(b) Vertical strain, E_{yy}
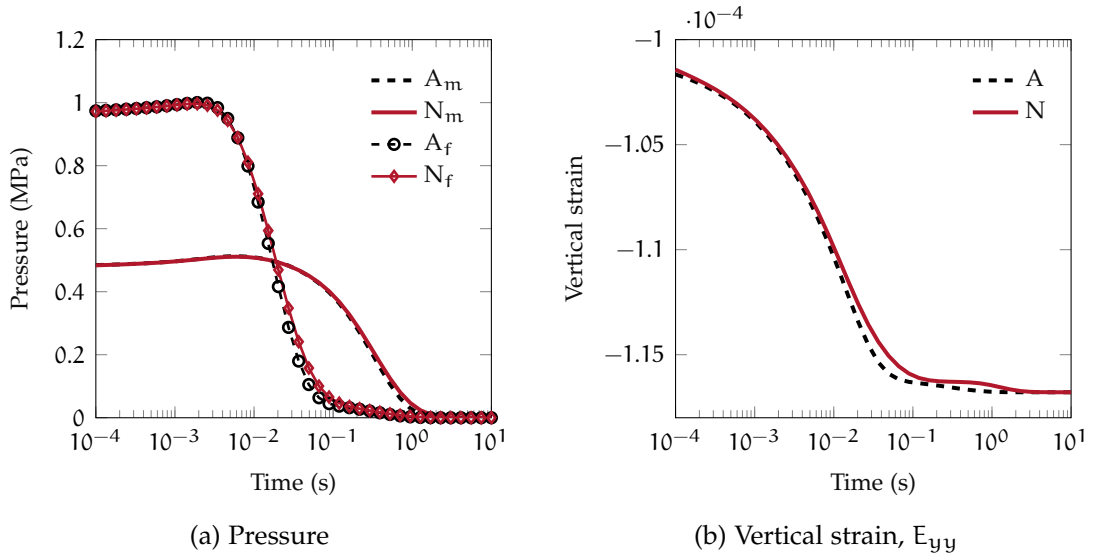
Figure 4.1: Pressure (a) and vertical strain (b) results for the analytical benchmark. 'A' and 'N' denote analytical and numerical solutions respectively.

4.3 Modelling on a geological grid

Here we test the numerical framework on a geological grid taken from Open Porous Media Initiative (2015) (Fig. 4.2). The domain is constructed using corner point gridding to account for complex structural features therein. As a result, the grid is a non-conforming mesh containing hanging nodes (Fig. 4.2). In classical FEM based approaches, such a grid would be challenging due to the difficulty in defining explicit basis functions for the non-conforming elements.
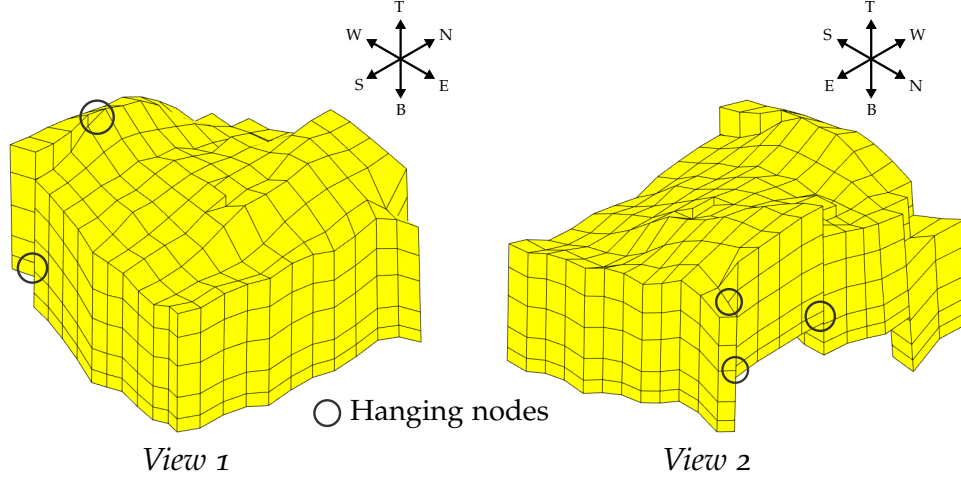
Figure 4.2: Geological grid used in the numerical study. Examples of hanging nodes are circled.

4.3.1 Problem setup and data

In addition to the north, south, east and west boundaries, we also have top and bottom boundaries, Γ_T and Γ_B respectively (Fig. 4.2). We apply a compressive stress of $\mathbf{\Sigma} \cdot \mathbf{n} = -50$ MPa along Γ_T. We constrain horizontal displacements and fix the bottom boundary. The remaining boundaries are then free to displace vertically. Initialisation is done by allowing the applied load to induce the matrix and fracture pressures. However, contrary to previous examples we allow the continuum pressures to equilibrate. At the point of equilibration, drainage is then supplied by a vertical well located at the center of the domain. The well is maintained with a bottom hole pressure of 10 KPa.

As per the analytical benchmark we consider isotropy at the macroscopic scale, as well as void-space fractures and dual-porosity materials. The fluid properties are given as $\rho_l^0 = 850$ kgm^{-3}, $\mu_l = 5$ cp, and $K_l = 0.5$ GPa. Matrix properties are given as $\phi_m^0 = 0.1$, $\nu_m = 0.99$, $k_m = k' = 1 \times 10^{-3}$ md. Fracture properties are given as $\phi_f^0 = 0.01$, $\nu_f = 0.01$, $\ell = 1$ m, and $K_f = 10$ d. Finally, mechanical properties are assigned as $K_m = 1$ GPa, $K_s = \infty$, and $\nu^* = 0.2$. The effective bulk modulus is chosen arbitrarily as $K^* = 0.1$ GPa.

4.3.2 Results

Figs. 4.3 to 4.5 show continuum pressure and volumetric strain results at $t = 0, 1, 5$ and 40 days for the geological grid test case described above. To start, Fig. 4.3 shows the matrix pressure change across the aforementioned time interval. We can see a slight pressure change over the first day at the producer, but very little away from this point. A similar trend is observed at $t = 5$ days with a noticeable pressure change across the domain by $t = 40$ days.

Next, Fig. 4.4 shows fracture pressure over $t = 0, 1, 5$ and 40 days. Contrast to Fig. 4.3 at $t = 0$, Fig. 4.4 shows the fracture pressure at the producer is several MPa lower than the matrix pressure. This is due to the high fracture permeability. From $t = 1$ day to $t = 5$ days there is a noticeable change in the overall pressure across the domain, again due to the high fracture transmissivity. Past day five, the matrix and fracture continua begin to equilibrate with pressure differences between the two becoming harder to differentiate (see $t = 40$ days).
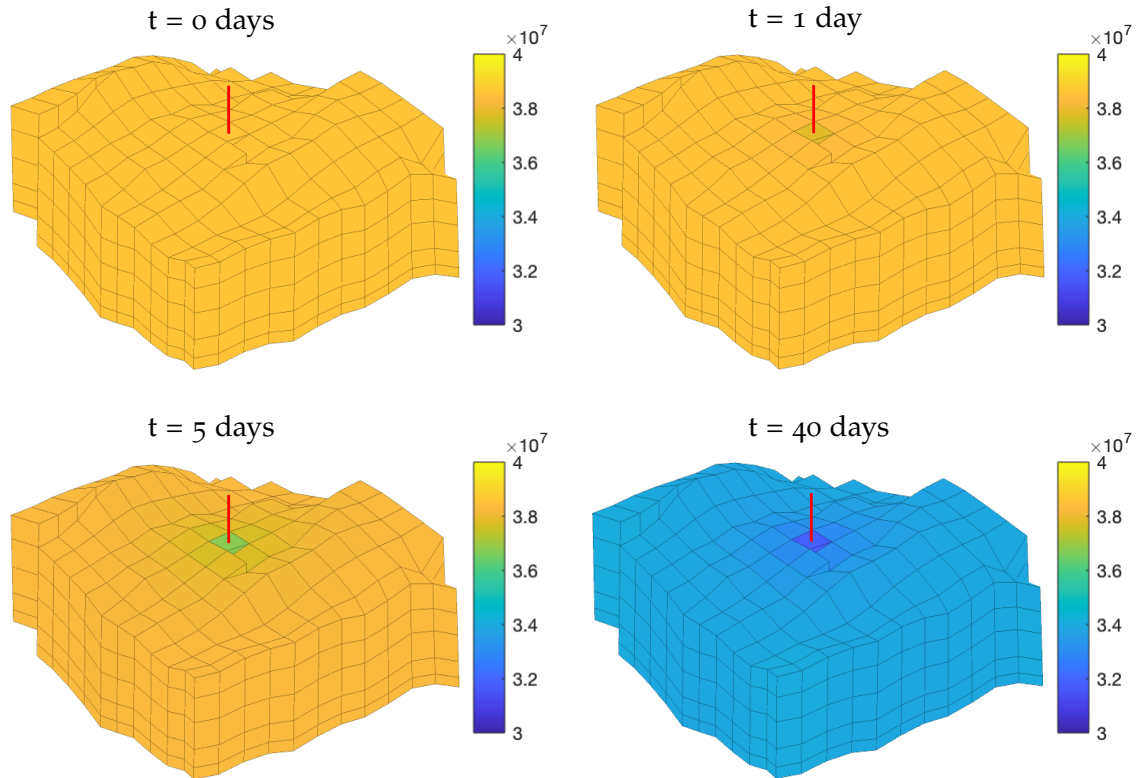
Figure 4.3: Matrix pressure results on the geological model. The red line represents the producer.

Finally, Fig. 4.5 shows the volumetric strain results over the same time interval considered previously. At $t = 0$ we can see high strains at the edges of the grid and lower strains toward the center. The high edge strains seem to be a result of the cell geometry and elevation with respect to the top load. At $t = 1$ day there is a subtle change in colour at the central cells associated with contraction due to depletion from the producer. The plots corresponding to $t = 5$ and 40 days show
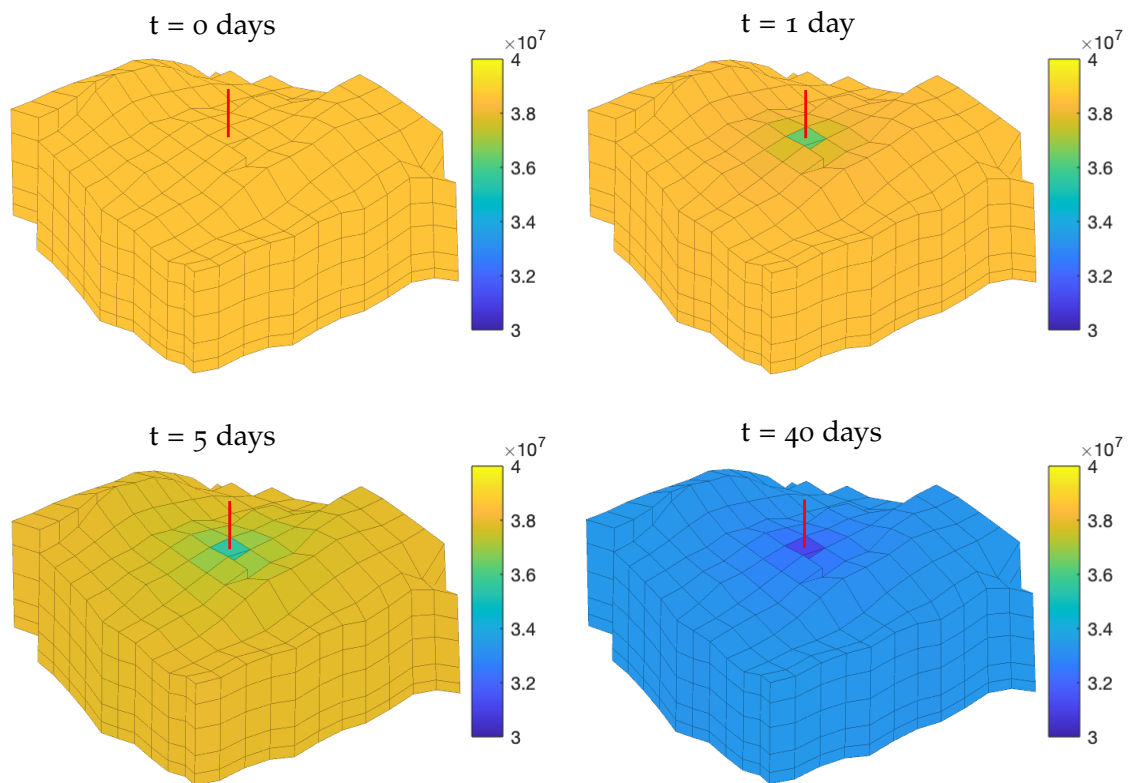
Figure 4.4: Fracture pressure results on the geological model. The red line represents the producer.

increasing contraction associated with depletion of the pressure support across the whole domain. In summary, despite the complexity of the grid, the volumetric strains are physically reasonable. In particular, looking at the cells with non-neighbouring connections, the strains across adjacent cells seem consistent.
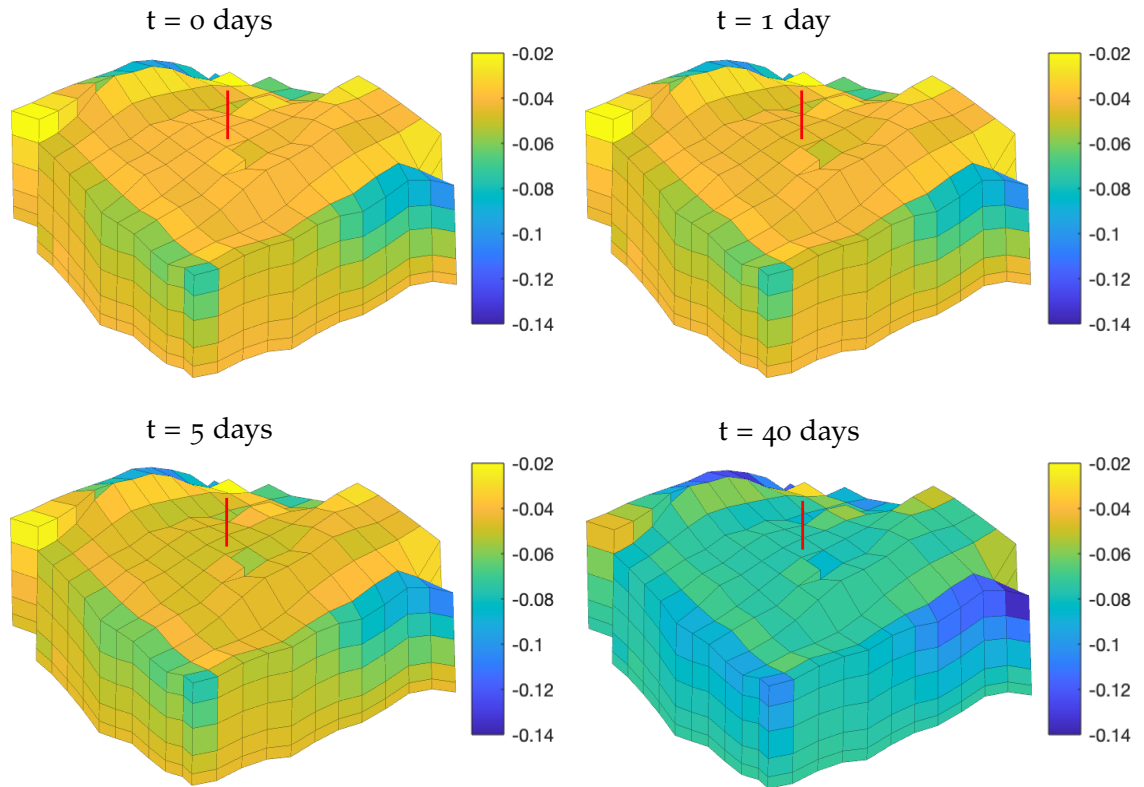
Figure 4.5: Volumetric strain results on the geological model. The red line represents the producer.

4.4 Conclusions

In this chapter, we introduced the numerical framework used for the (macroscopic) modelling of poroelastic dual-continua. The features of the framework are that it is locally mass conservative with respect to the flow problem and flexible with respect to gridding. This latter property owes to the virtual-element discretisation used for mechanics, which when used with the finite-volume method for flow allows for simulation on unstructured polygonal grids. We tested the resulting framework on an analytical benchmark and a 'challenging' geological grid. In the former we achieved a good match to the analytical solution. In the latter our results were physically reasonable.

For future work, the FVM-VEM approach could be an interesting tool for concurrent multiscale approaches. In this, nonhomogenisable features such as faults or other discontinuities could be modelled explicitly, leveraging the flexibility of VEM, whilst homogenisable materials could be represented using the continuum framework presented here. Examples of this type of work can be found in Moinfar et al. (2013), Vernerey and Kabiri (2014) and Jiang et al. (2016).

5

Application to a micro-macro study

In this chapter we use the numerical framework introduced in Chapter 4 to further study the relations between poroelastic microscopic and dual-continuum models, given material and modelling assumptions made at the former. In Section 5.1, we introduce the tests studied in this chapter. Our tests increase in complexity from an uncoupled isotropic case to several anisotropic poroelastic cases. In Section 5.2, we introduce the various modelling considerations that enable a meaningful comparison between the micro and macroscales. In Section 5.3 we present and discuss the results for the considered tests. Finally, we finish the chapter with the conclusions and recommendations for future work in Section 5.4. The contents of this chapter are based on work done in Ashworth and Doster (2020).

5.1   Test cases

Following Section 1.3, work has gone into testing and validating the DC concept for the flow problem. However, little has been done to asses validity of the poroelastically coupled DC approach, particularly whilst considering various assumptions made at the microscale.

   With the numerical framework in-hand, in this chapter we present and conduct several numerical tests to investigate whether the macroscopic dual-continuum poroelastic model can capture global flow and deformation behaviours of a microscale model (MS). We do this study given the modelling assumptions made as part of the homogenisation procedure in Chapter 2, and considering various material assumptions at the microscale. For this work, the latter concerns anisotropic effects. Further, we review several considerations in order to ensure meaningful result comparisons between modelling scales.

   To start, we introduce the four numerical experiments used to carry out our tests in light of various microscopic modelling and material assumptions. In each case we consider an idealised representation of a naturally fractured rock sample. Our idealisation comes in that we assume the fracture fabric to be periodic. To start we consider an undeformable isotropic material to understand the physics

of the flow problem. We progress by introducing mechanics to the isotropic system, and then adding complexity by considering anisotropic material cases.

In every case we consider the dimension of the domain to be 1 m × 1 m. Each experiment then represents a thin 2D slice taken from a 3D sample such that, in the case of the mechanical problem, the plane stress assumption applies.

5.1.1 Case 1: Undeformable isotropic

For this test we study an (isotropic) undeformable matrix permeated by an isotropic undeformable fracture network. The test is setup as a uniaxial drainage problem, such that the north boundary is open to flow, $\hat{P}_m = \hat{P}_f = 0$, whilst the east, west and south boundaries are zero flux boundaries (Fig. 5.1a). Initial pressures for the continua are set at $P_m^0 = P_f^0 = 2$ MPa. Volume fractions for matrix and fracture material are $\nu_m = 0.998$ and $\nu_f = 0.002$ respectively, given a fracture spacing $\ell = 0.1$ m. Local porosities for the two continua are then prescribed as $\varphi_m = 0.1$ and $\varphi_f = 0.9$, where the volume fractions link the global and local Lagrangian porosities so that $\phi_\alpha = \nu_\alpha \varphi_\alpha$. Intrinsic matrix permeability k_m is taken as 0.01 md, whilst individual fracture permeability k_f is calculated using the parallel plate model with a fracture aperture of $a_f \approx 1.05 \times 10^{-4}$ m (Witherspoon et al. 1980). The resulting permeability is 950 d for each fracture. Fluid properties are $\rho_l^0 = 1000$ kgm^{-3}, $\mu_l = 1$ cp, and $K_l = 2.5$ GPa. Upscaling individual fracture permeability to a continuum permeability for use in the DC model is done using the cubic law (Witherspoon et al. 1980). The resulting isotropic fracture continuum permeabitity is $K_f \approx 1000$ md. Finally, due to the dissociation by the fracture network, the macroscopic matrix permeability is zero.

(a)   (b)
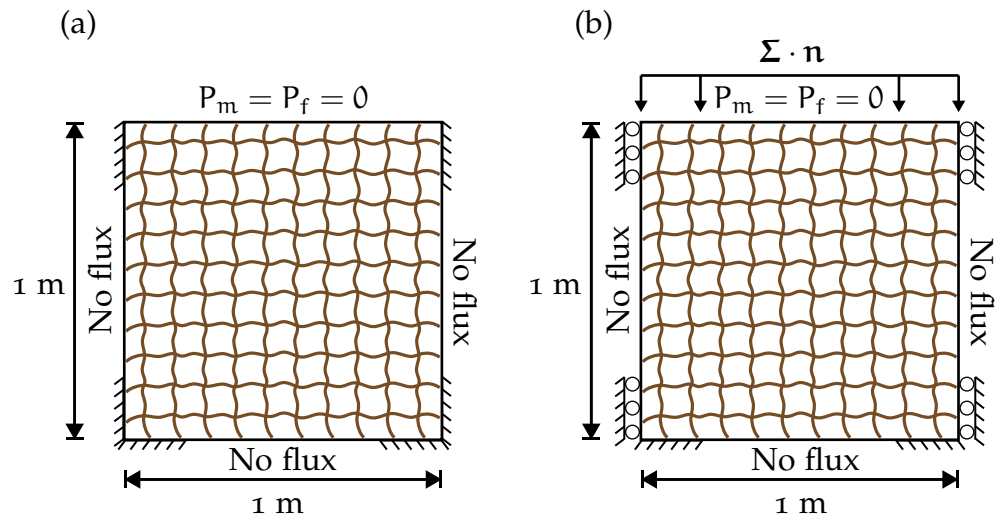
Figure 5.1: Test case setup for the undeformable isotropic problem (a) and the deformable isotropic problem (b).

5.1.2 Case 2: Deformable isotropic

We now consider a deformable counterpart to the experiment described in Section 5.1.1 (Fig. 5.1b). Accordingly, the Young's moduli for the matrix and fracture materials are $E_m = 36$ GPa and $E_f = 36$ MPa respectively. The latter is chosen for illustrative purposes as $E_f = E_m/1000$. Both continua are assigned a Poisson's ratio of $\nu = 0.2$. For an isotropic medium under the plane stress assumption, the stiffness tensor written with Voigt notation is given as

$$\mathbb{C} = \begin{bmatrix} \dfrac{E}{1-\nu^2} & \dfrac{\nu E}{1-\nu^2} & 0 \\[2ex] & \dfrac{E}{1-\nu^2} & 0 \\[2ex] \text{sym} & & G \end{bmatrix} \tag{5.1}$$

Entries for $\mathbb{C}_m$ and $\mathbb{C}_f$ can be calculated with Eq. (5.1) and the defined intrinsic parameter values.

For $\mathbb{C}^*$, parameters must be calculated by homogenisation. In Section 3.4.4 we suggested using the Hashin-Shtrikman lower bounds, as an initial homogenisation approach for the estimation of the mechanical properties of densely fractured rock. The lower HS bound for the bulk modulus is given in Eq. (3.40), whilst the shear modulus is given here as

$$G^{\mathcal{H}-} = G_f + \frac{\nu_m}{[(G_m - G_f)^{-1} + 6\nu_f(K_f + 2G_f)(5G_f(3K_f + 4G_f))^{-1}]}, \tag{5.2}$$

We map between the 3D bulk modulus calculated in Eq. (3.40) and the 2D homogenised bulk modulus under plane stress using the following relation (e.g. Torquato 2002),

$$K^* = \frac{9K^{\mathcal{H}-}G^{\mathcal{H}-}}{3K^{\mathcal{H}-} + 4G^{\mathcal{H}-}}. \tag{5.3}$$

The Poissons ratio for the composite dual-continuum under plane stress is given by

$$\nu^* = \frac{K^* - G^{\mathcal{H}-}}{K^* + G^{\mathcal{H}-}}. \tag{5.4}$$

Finally, the homogenised Young's modulus E^* can be recovered from

$$4K^* = \mathbf{1} : \mathbb{C}^* : \mathbf{1} = \frac{2E^*}{(1-\nu^*)}. \tag{5.5}$$

With Eqs. (5.4) to (5.5) the homogenised parameters are $\nu^* = 0.2$ and $E^* = 18.0$ GPa.

We assume the matrix and fracture skeletons to be made up of the same solid material. We then assign a solid modulus K_s of 70 GPa for both continua.

For the coupled mechanics and flow problem, initialisation is done by letting the applied load induce the continuum pressures. Accordingly, we define the starting point for the experiment to be the undrained, loaded configuration, P_m^{0+}, P_f^{0+}, U^{0+}. The load is prescribed as $-\Sigma \cdot n = -2$ MPa on the north boundary. The domain is horizontally constrained at the boundaries, but remains free to move along the vertical axis apart from at the south boundary where the sample is fixed. The parameters for flow are as defined in Section 5.1.1

5.1.3 Case 3: Geometry-induced anisotropy - explicit computation of $\mathbb{C}^*$

The third experiment is concerned with an anisotropic deformable material. Anisotropy has recently been studied in poroelastic DC materials in the context of flow properties (Zhang et al. 2019). However, here we consider the directional dependence of *both* mechanical and flow properties. Accordingly, anisotropy in this example is introduced geometrically by considering just a single vertical fracture set which is aligned with the second principal axis (Fig. 5.2a). The 2D domain is then orthotropic. Whilst anisotropy exists at the macroscale, the intrinsic mechanical parameters remain isotropic for each continuum and are as described in Section 5.1.2. The plane stress stiffness tensor for an orthotropic material is given by

$$
\mathbb{C} = \begin{bmatrix} \dfrac{E_1}{1-\nu_{12}\nu_{21}} & \dfrac{\nu_{21}E_1}{1-\nu_{12}\nu_{21}} & 0 \\[2ex] & \dfrac{E_2}{1-\nu_{12}\nu_{21}} & 0 \\[2ex] \text{sym} & & G_{12} \end{bmatrix},
\tag{5.6}
$$

Parameters of the homogenised stiffness tensor may be approximated explicitly for this geometry, using the Reuss and Voigt mixture theory rules introduced in Section 3.4. Subsequently, for the Young's moduli

$$
E_1^* = \left(\frac{\nu_m}{E_m} + \frac{\nu_f}{E_f} \right)^{-1}, \quad E_2^* = \nu_m E_m + \nu_f E_f,
\tag{5.7}
$$

where having removed a fracture set, the volume fraction of the fracture continuum is now $\nu_f = 0.001$ (resp. $\nu_m = 0.999$). For the homogenised Poisson's ratio ν_{21}^* and shear modulus G_{12}^* mixture theory gives

$$
\nu_{21}^* = \nu_m \nu_m + \nu_f \nu_f, \quad G_{12}^* = \left(\frac{\nu_m}{G_m} + \frac{\nu_f}{G_f} \right)^{-1}.
\tag{5.8}
$$

The other Poisson's ratio ν_{12}^* is readily determined by the symmetry in Eq. (5.6) which requires $\nu_{12}E_2 = \nu_{21}E_1$. From Eqs. (5.7) to (5.8) and the aforementioned symmetry relation, the mechanical parameters are given as $E_1^* = 18.0$ GPa, $E_2^* = 36.0$ GPa, $\nu_{21}^* = 0.200$, $\nu_{12}^* = 0.100$ and $G_{12}^* = 7.50$ GPa.

The anisotropic fracture continuum leads to an anistropic permeability tensor so that permeability in the x and y directions are $K_{f,x} = 0$ and $K_{f,y} \approx 1000$ md respectively. For the matrix, the macroscopic permeability is also anisotropic with $K_{m,x} = 0$ and $K_{m,y} \approx 0.01$ md. The remaining flow parameters, boundary conditions and initialisation are as described in Sections 5.1.1 and 5.1.2.
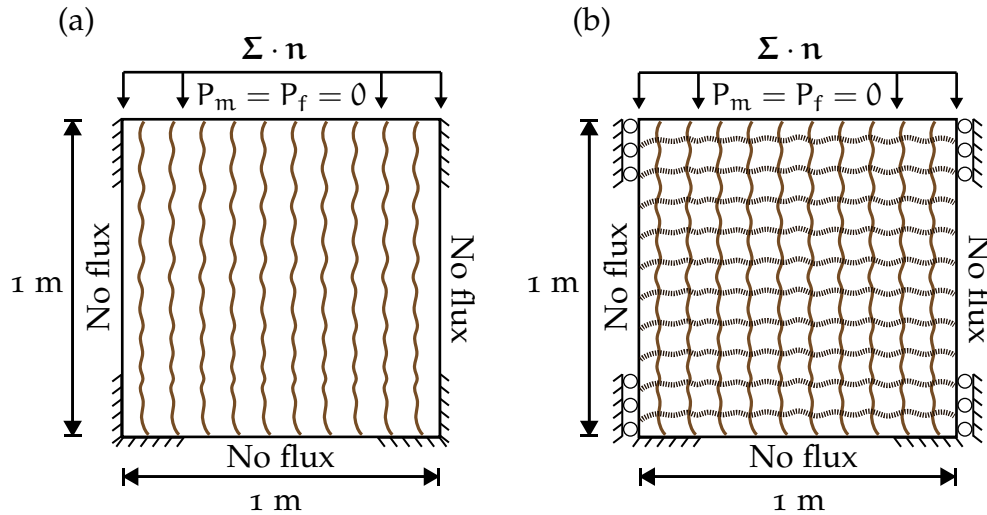
Figure 5.2: Test case setup for the anisotropic problem with one fracture set (and explicit computation of $\mathbb{C}^*$) (a) and the anisotropic problem with two fracture sets (and numerical computation of $\mathbb{C}^*$) (b).

5.1.4 Case 4: Material-induced anisotropy - numerical computation of $\mathbb{C}^*$

The final experiment is on an anisotropic material with two fracture sets aligned with each of the principal axes (Fig. 5.2b). Anisotropy is now introduced through the fracture material, with each fracture set having different intrinsic mechanical and flow properties. These property differences are in analogy to fractures containing different amounts of infill material. To represent this conceptually within the model we assign different intrinsic porosities to the individual fracture sets. Further, we separate the intrinsic Young's moduli and permeabilities of each fracture set by two orders of magnitude. For the horizontal fracture set we assign $\varphi_{f,x} = 0.9$, $E_{f,x} = 3.6$ MPa and an intrinsic fracture permeability of 950 d. For the vertical fracture set we assign $\varphi_{f,y} = 0.4$, $E_{f,y} = 360$ MPa and an intrinsic permeability of 9.5 d. Upscaling the fracture permeability remains trivial, with $K_{f,x} \approx 1000$ md and $K_{f,y} \approx 10$ md. However, homogenistion for the parameters in the homogenised stiffness tensor now cannot be done by explicit approximation. Instead we use a deformation-driven computational homogenisation approach:

We generate unit strains for a sequence of linear displacement boundary conditions, and in doing, determine the entries of $\mathbb{C}^*$ (Daniel et al. 1994). Linear displacements are chosen as they produce better estimates for effective stiffness tensors for materials with a stiff matrix and weaker inclusion material (Pecullan et al. 1999), as is the case here.

With the computational homogenisation approach, the mechanical parameters in $\mathbb{C}^*$ are calculated as $E_1^* = 32.7$ GPa, $E_2^* = 3.40$ GPa, $\nu_{21}^* = 0.019$, $\nu_{12}^* = 0.173$ and $G_{12}^* = 1.28$ GPa.

The overall volume fraction for the fracture continuum is the same as in experiment two. However, the intrinsic Lagrangian fracture porosity is now the arithmetic average of the two intrinsic fracture set porosities ($\varphi_f = 0.65$). Fluid and matrix properties remain the same as those for the other experiments. Boundary conditions and initialisation are the same as in experiments two and three.

5.2 Modelling considerations

Here we review several considerations to enable the interpretation of the test results to follow.

5.2.1 On the REV

Our periodic assumption of the underlying microstructure eases the requirements on our definition for an REV. In this periodic case, all the necessary geometrical and physical process information is captured within an elementary cell that is the size of the heterogeneity (ℓ) (Royer et al. 2002; Dormieux et al. 2006). Accordingly, the separation of scales is now defined as $\ell \ll L$. The elementary cell definition of our REV will be useful for interpreting the discretisation choice of the DC problem.

5.2.2 Meshing

For the four tests we discretise the microscale problem with a 200×200 Cartesian mesh, that is locally refined around the fractures (Fig. 5.3). For the dual-continuum problem we discretise the domain using a 10×10 Cartesian mesh. In the latter case, each element then coincides with an elementary cell (in the geometrical sense) (Fig. 5.3).

Microscale and dual-continuum fields are compared at an observation point at the base of our samples. At this point we assume that our pressure solutions are sufficiently smooth, thus satisfying the physical process scale separation requirement. Further, the observation point coincides with the macroscopic material point, in this case the element centroid (Fig. 5.3).
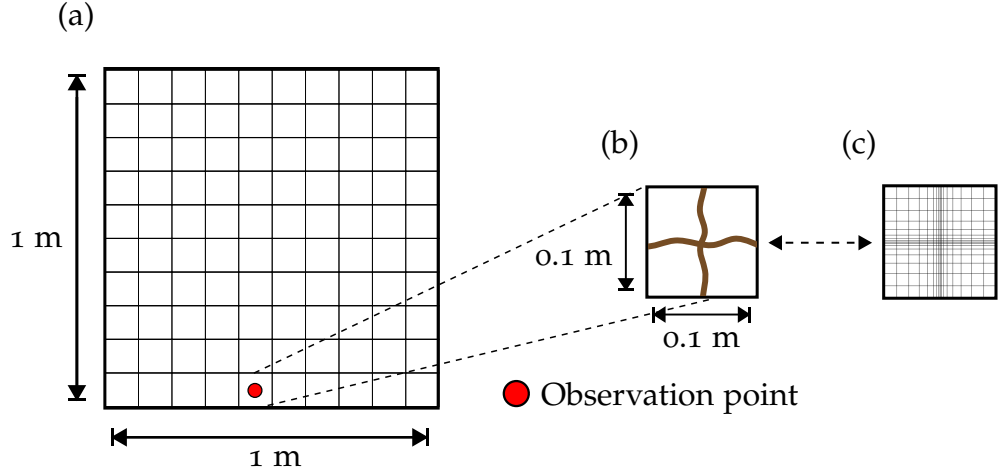
Figure 5.3: Representations of the isotropic test problem: (a) the dual-continuum grid containing the observation point where the two modelling approaches are compared, (b) an elementary cell and (c) an equivalent microscale representation of the elementary cell.

5.2.3 Quantities of interest

At the observation point for each test we consider the element-wise total and continuum volumetric strains, and continuum pressures. Element-wise total and continuum volumetric strains are defined as $E_j = tr(\mathbf{E}_j) = \Delta|\Omega_j^{\mathcal{D}}|/|\Omega_j^{\mathcal{D},0}|$, and $E_{j,\alpha} = \Delta|\Omega_{j,\alpha}^{\mathcal{D}}|/|\Omega_{j,\alpha}^{\mathcal{D},0}|$, respectively. We compare averaged results over the micro-scale to element level results from the dual-continuum. To enable the former, we define the following discrete counterpart to Eq. (2.36)

$$\bar{z}_{j,\alpha}^{\mathcal{D}} = \frac{1}{|\Omega_{j,\alpha}^{\mathcal{D},0}|} \int_{\Omega_{j,\alpha}^{\mathcal{D}}} z^h(\mathbf{x}) \, dV, \tag{5.9}$$

Continuum averaged pressures and volumetric strains can then be recovered using Eq. (5.9) with discrete microscopic fields p^h or ϵ^h in place of z^h. Total volumetric strain is likewise obtained using Eq. (5.9) by replacing $|\Omega_{j,\alpha}^{\mathcal{D}}|$ with $|\Omega_j^{\mathcal{D}}|$.

For the DC problem, pressures and element-wise total volumetric strain are recovered naturally from the element centroid (Andersen et al. 2017a). To get continuum strains, however, we must take a different approach. Starting with the matrix continuum, and comparing a volume averaged change in local porosity Eq. (2.67) to the effective change in matrix porosity given by Eq. (2.23), such that $d\phi_m = v_m d\varphi_m$, allows us to derive the following expression for the volumetric matrix strain

$$E_m = \mathbf{1} : \bar{\epsilon}_m = \frac{1}{b_m} \left[\frac{1}{v_m} \left(B_m \mathbf{1} : \mathbf{E} + \frac{P_m}{N_m} + \frac{P_f}{Q} \right) - \frac{P_m}{n_m} \right]. \tag{5.10}$$

88

We note the expression for E_m in Eq. (5.10) is only possible for an isotropic matrix as the inverse contraction map involving $\mathbf{b}_m$ is otherwise ill-posed. With E and E_m we can recover the fracture volumetric strain E_f for the DC model using Eq. (2.34).

5.3 Results and discussion

Here we present the results and analyses for the numerical test cases described in Section 5.1 under the modelling considerations described in Section 5.2. All results are given from observation points such as that shown in Fig. 5.3.

5.3.1 Case 1: Undeformable isotropic

Fig. 5.4 shows the element averaged pressure evolutions from both microscale and dual-continuum simulations for the undeformable isotropic material case. Both models show a rapid decrease in fracture pressure within the first millisecond followed by a delayed pressure response in the matrix. These general patterns can be attributed to the contrast in continuum permeabilities. Whilst both models show general decreasing trends, the rate of MS fracture pressure change begins to smooth out at middle times. Coupled to this smoothing is the onset of microscale matrix pressure diffusion. In contrast, matrix pressure diffusion occurs later in the DC model. Further, compared to the microscale case, the DC matrix diffusion process occurs more rapidly (indicated by a steeper gradient).
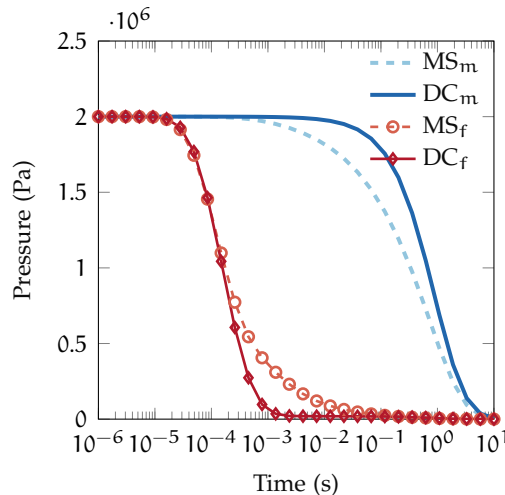
Figure 5.4: Matrix and fracture continuum element averaged pressure evolutions for the undeformable isotropic test case. 'MS$_\alpha$' and 'DC$_\alpha$' denote quantities related to microscale and dual-continuum models for continuum α respectively.

The disparities in matrix and fracture pressure diffusion between the two modelling approaches arise from the first-order transfer term Eq. (2.7) used by

the dual-continuum model. In using a linear mass transfer model one implicitly places a pseudosteady-state diffusion assumption on the communication between matrix and fracture continua. As a result, transient matrix drainage effects are neglected by the DC approach. Neglecting transient effects leads to the delay in DC matrix pressure diffusion we see in Fig. 5.4, and the loss of pressure support in the fractures.

Shortcomings of using simplified transfer concepts have been well documented in literature (e.g. Berkowitz et al. 1988; Lemonnier and Bourbiaux 2010). Previous works have thus sought to improve on the linear inter-continuum flow coupling term by including transient effects (Zimmerman et al. 1993; Sarma et al. 2004; March et al. 2016; Zhou et al. 2017). In the next chapter, we use a data-driven approach to alleviate the problems posed by a linear transfer model. However, in the current chapter, we acknowledge the shortcomings of the transfer term used herein, with the focus being on understanding the coupled poroelastic behaviour.

5.3.2 Case 2: Deformable isotropic

Pressure and total element volumetric strain results for the deformable isotropic case are shown in Fig. 5.5. In Fig. 5.5a both modelling approaches predict higher induced initial pressures in the fracture than in the matrix. Further, both approaches show rapid decreases in fracture pressure and gradual decreases in matrix pressure. In Fig. 5.5b the MS and DC models show increasing volumetric strain evolution behaviours. However, for both pressure and strain, specific differences of the variable fields between the two modelling approaches may be observed at both early and late times. The disparity in late-time matrix pressure evolution (Fig. 5.5a), is again due to the first-order inter-continuum transfer model (see Section 5.3.1). Over the same late-time period, we also observe a difference in volumetric strain (Fig. 5.5b).

Of more interest in Fig. 5.5 are the early-time results for continuum pressures. In Fig. 5.5a both microscale matrix and fracture pressures exhibit non-monotonic behaviour, known as the Mandel-Cryer effect. These pressure rises are not seen in the dual-continuum pressure responses. A similar observation was also made in the work of Zhang et al. (2019), albeit for a different problem.

Fig. 5.6 shows individual continuum volumetric strain evolutions. In Fig. 5.6b both modelling approaches show similar increasing strain behaviour with time. However in Fig. 5.6a, we observe the MS matrix strain shows early-time non-monotonic behaviour, contrary to DC matrix strain.

The early non-monotonic differences in pressure and matrix strain between the two modelling approaches result from the underlying pressure assumption made for the DC model. In the derivation of the constitutive model in Section

(a) Pressure

(b) Volumetric strain, E

Figure 5.5: Matrix and fracture continuum element averaged pressure (a) and total element volumetric strain (b) evolutions for the deformable isotropic test case. 'MS$_\alpha$' and 'DC$_\alpha$' denote quantities related to microscale and dual-continuum models for continuum α respectively.

(a) Matrix vol. strain, E$_m$

(b) Fracture vol. strain, E$_f$

Figure 5.6: Matrix (a) and fracture (b) volumetric strain evolutions for the deformable isotropic test case. 'MS' and 'DC' denote quantities related to microscale and dual-continuum models.

2.4 we assumed a local equilibrium of pressure within each continuum over an REV. The induced response predicted in by the DC model is thus for a system in mechanical and hydrostatic equilibrium. Instead, the microscale model makes no such pressure assumption. To understand the specific impacts of the latter it is interesting to look at the local flow and deformation behaviours shown at the microscale.

Fig. 5.7 shows the MS pressure and volumetric strain responses within the first 100 microseconds at the observation point. At t_{0+} in Fig. 5.7a, we observe pressure in the horizontal fracture is higher than the vertical fracture. This dis-

equilibrium is concurrent with the negative and positive fracture strains for the horizontal and vertical fractures respectively (Fig. 5.7b). From t_{0+} to t_1, Fig. 5.7a shows, away from the fracture intersection, horizontal fracture pressure drops slightly. However, vertical fracture pressure increases. These pressure changes occur with further contraction and expansion respectively (Fig. 5.7b). Over the same time period matrix strain increases (Fig. 5.7c). From t_1 to t_5 the pressure in both fractures is increasing (Fig. 5.7a), with matrix and fracture deformations following the same evolution paths described previously. Finally, at t_{10} the fractures reach a pressure equilibrium (Fig. 5.7a).
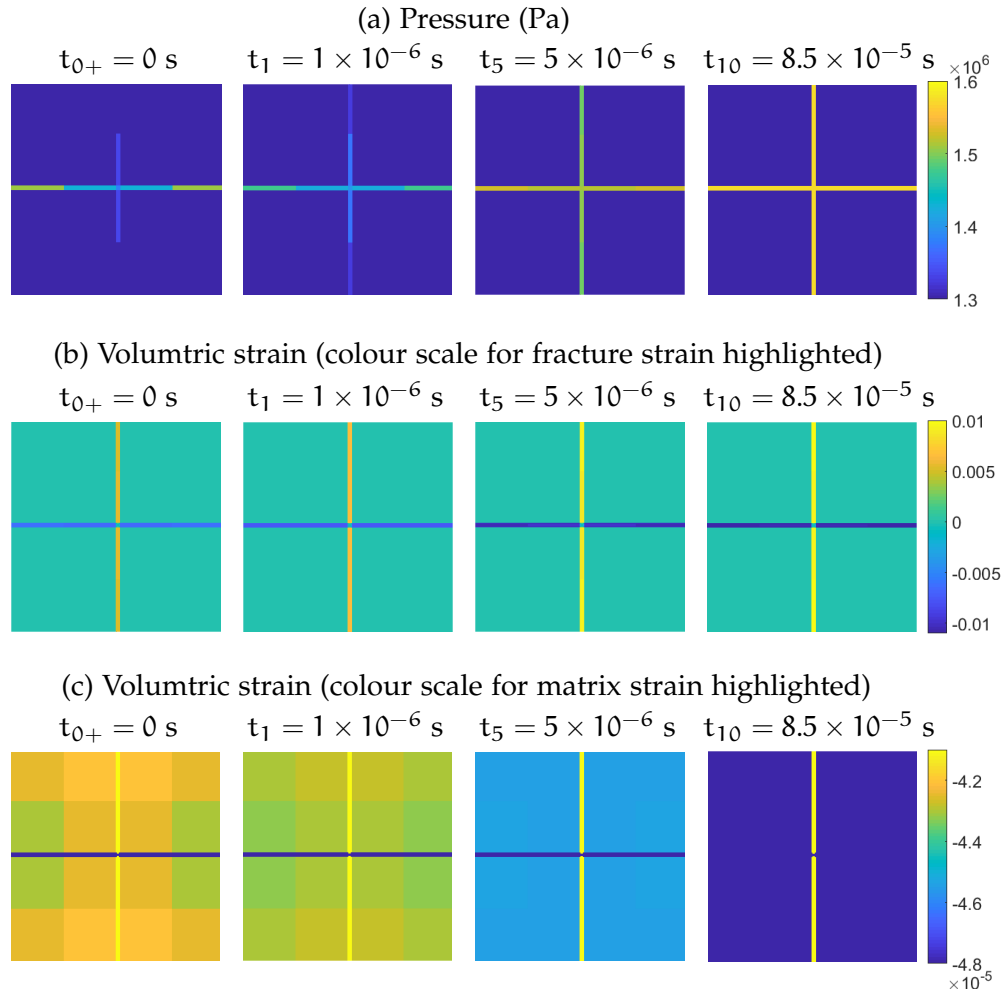
Figure 5.7: Pressure (a) and volumetric strain (highlighted for fractures and matrix, (b) and (c) respectively) fields at different time levels t_i for the MS representation of the deformable isotropic material. Each field plot is 5 mm × 5 mm and is located at the observation point. Subscript $0+$ denotes the time level corresponding to the undrained, loaded configuration.

We can now explain the early-time non-monotonic behaviours in Fig. 5.5a and Fig. 5.6a with the description of the local processes shown in Fig. 5.7. Following t_{0+}, intra-fracture flow is driven by the pressure disequilibrium between the horizontal and vertical fractures. Between t_{0+} and t_1, horizontal fracture contraction occurs primarily due to the dissipation of the fluid pressure support.

Vertical fracture expansion follows due to poroelastic coupling to accommodate incoming fluid from the horizontal fracture. As the vertical fracture expands it forces the contraction of the matrix, and thus the increasing matrix strain shown in Fig. 5.6a and Fig. 5.7. After t_1, deformation drives the horizontal fracture pressure increase due to fluid compressibility. The overall fracture continuum pressure increases (Fig. 5.5a), with strain generating pressure in the horizontal fracture, whilst the pressure change associated with vertical fracture expansion slows. The latter occurs due to the low matrix permeability which prohibits dissipation of excess matrix pressure, until later times. As a result, the undrained matrix stiffness increases with its progressive contraction, slowing vertical fracture expansion until a mechanical equilibrium is reached. The overall fracture continuum pressure rise finally stops when the fractures have reached mechanical equilibrium with the matrix and an internal hydrostatic equilibrium.

The local processes shown by the MS model are not captured by the DC model due to the underlying modelling assumptions made at the microscale as part of the homogenisation procedure for the latter. However, Figs. 5.5 to 5.6 do show that, aside from the local equilibration processes, the DC model can capture the global poroelastic behaviours of the MS model.

5.3.3 Case 3: Geometry-induced anisotropy - explicit computation of $\mathbb{C}^*$

Here we show the results for the geometry-induced (single-fracture set) anisotropy case. Pressure and total volumetric strain are given in Fig. 5.8, whilst Fig. 5.9 shows the individual continuum volumetric strains.
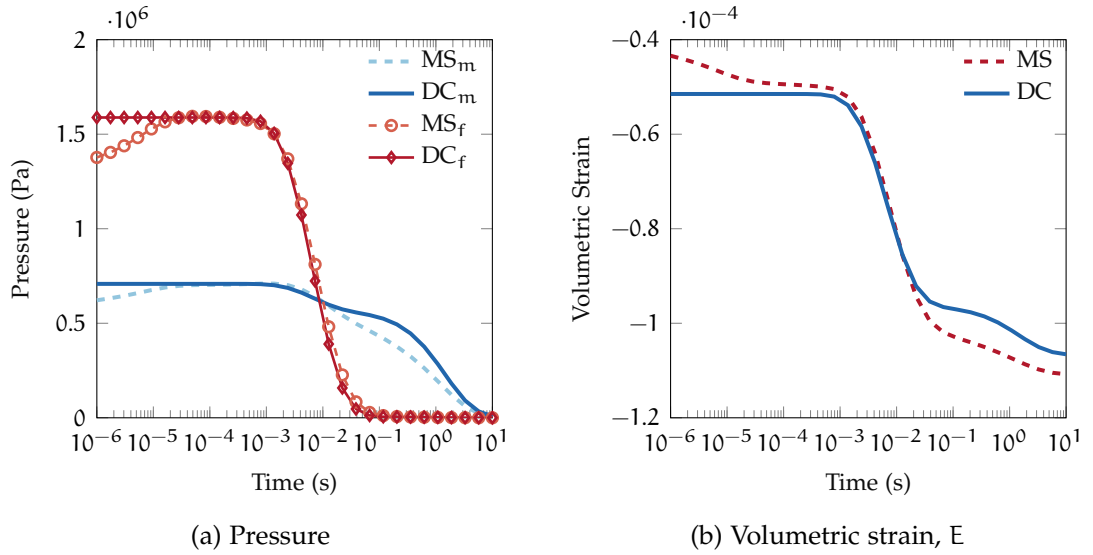

(a) Pressure

(b) Volumetric strain, E

Figure 5.8: Matrix and fracture continuum element averaged pressure (a) and total element volumetric strain (b) evolutions for the geometry-induced anisotropy test case. 'MS$_\alpha$' and 'DC$_\alpha$' denote quantities related to microscale and dual-continuum models for continuum α respectively.
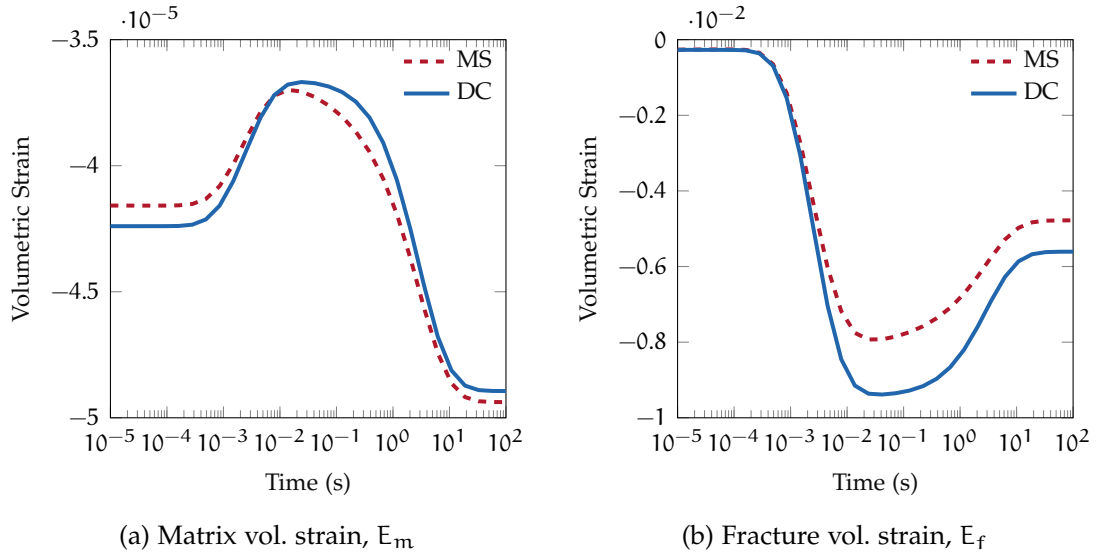
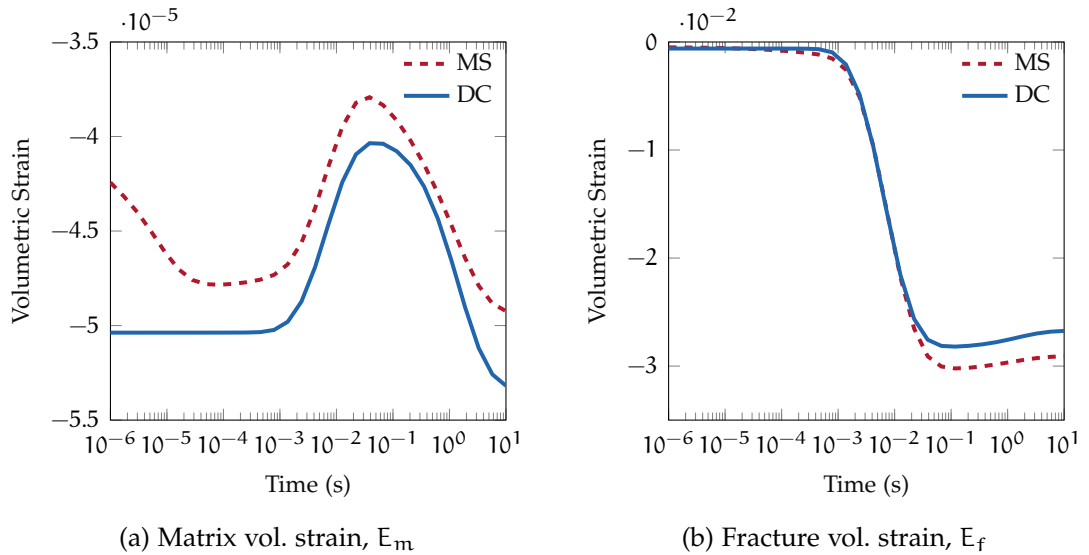Figure 5.9: Matrix (a) and fracture (b) volumetric strain evolutions for the geometry-induced anisotropy test case. 'MS' and 'DC' denote quantities related to microscale and dual-continuum models.

In Fig. 5.8a, both models show a smaller difference between the initial matrix and fracture pressures compared to the previous cases. Now, the average fracture pressure is only slightly higher than the corresponding matrix pressure. Further, we do not observe the early-time Mandel-Cryer effect seen previously in the MS model. However, beyond early-time pressures, the general trends we see in Fig. 5.5a can still be observed in Fig. 5.8a. Specifically, a rapid decrease in fracture pressure followed by a smoother matrix pressure decrease. As expected, the late-time differences in matrix pressure observed previously are present in the current test. For both modelling approaches there is a good agreement in matrix and fracture pressure evolutions. The total element volumetric strain evolutions are also similar between the two modelling approaches, with an overall increase in strain as the material compacts.

The similarity in total volumetric strain between the two approaches is reflected in the individual continuum strains (Fig. 5.9). The matrix shows early-time expansion behaviour followed by contraction. Fracture deformation is coupled to matrix deformation (and vice versa). Fracture contraction is therefore followed by a period of expansion as the matrix drains and contracts.

The small difference between initial matrix and fractures pressures shown by both models in Fig. 5.8a is explained by considering the geometry of the fractures in this anisotropic case. With the fracture set being aligned with the direction of loading (Fig. 5.2a), the stiffer matrix acts like a series of columns, supporting a significant portion of the applied load. Through the coupling between stress and pressure, the low portion of stress 'seen' by the fracture phase leads to the low induced fracture pressure shown in Fig. 5.8a. Finally, the absence of the Mandel-Cryer effect in the current case is due to the pressure being at equi-

librium within the single-fracture set. As a result local processes do not drive early-time poroelastic intra and inter-continuum pressure generation.

5.3.4 Case 4: Material-induced anisotropy - numerical computation of $\mathbb{C}^*$

Fig. 5.10 and Fig. 5.11 show pressure and total strain, and individual continuum strain results respectively, for the material-induced anisotropy case. Both models in Fig. 5.10a show a strong difference in the early-time magnitudes of matrix and fracture pressures. The MS model shows similar early-time Mandel-Cryer fracture pressure behaviour to what we observed in Fig. 5.5a. In contrast, the early-time MS matrix non-monotinicity is negligible in Fig. 5.10a compared to the isotropic case. However, at later times we see a significant non-montonic evolution in matrix pressure that is shown by *both* modelling approaches. This non-monotonic matrix pressure rise starts earlier in the MS model than the DC model. Finally, we observe in both models fracture diffusion due to the boundary is delayed, compared to previous cases. Instead, matrix and fracture diffusion start at similar times, indicating a single-continuum response. Coupled to the delayed fracture diffusion response is the delayed increase in total volumetric strain (Fig. 5.10b).

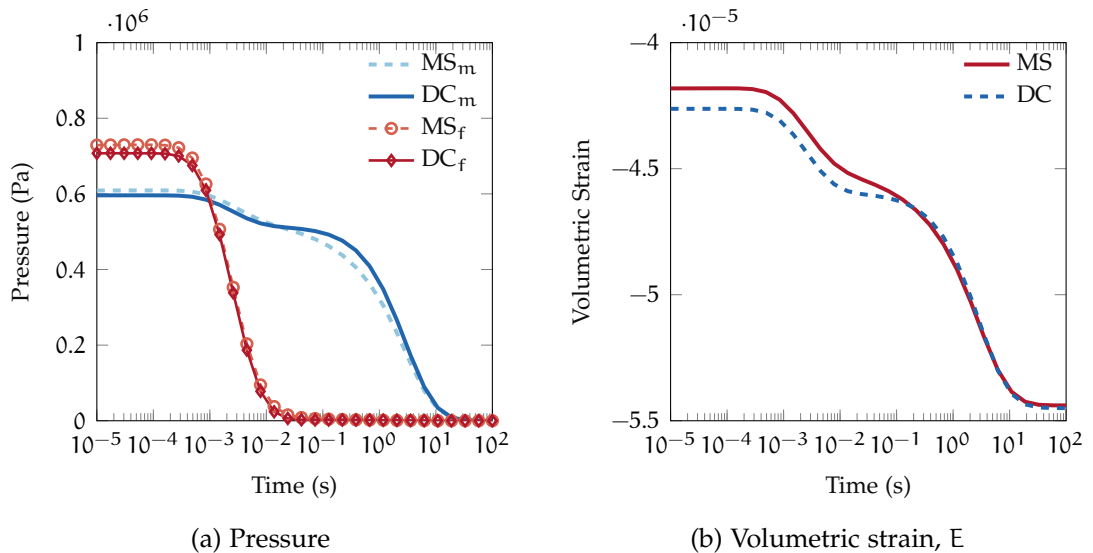(a) Pressure   (b) Volumetric strain, $\mathbb{E}$
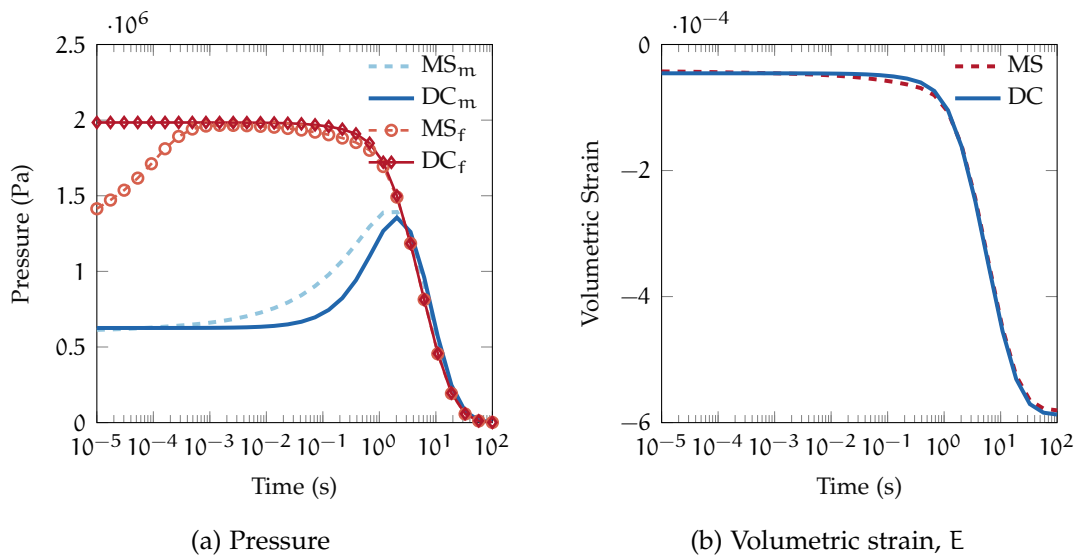
Figure 5.10: Matrix and fracture continuum element averaged pressure (a) and total element volumetric strain (b) evolutions for the material-induced anisotropy test case. 'MS$_\alpha$' and 'DC$_\alpha$' denote quantities related to microscale and dual-continuum models for continuum α respectively.

In Fig. 5.11 both modelling approaches give similar continuum strain evolutions. Similar to Fig. 5.6a, Fig. 5.11a shows the DC approach misses the early-time matrix strain non-monotinicity displayed by the MS approach. However, contrast to Fig. 5.6a, Fig. 5.11a shows a smoother early-time MS matrix strain

(a) Matrix vol. strain, E_m (b) Fracture vol. strain, E_f
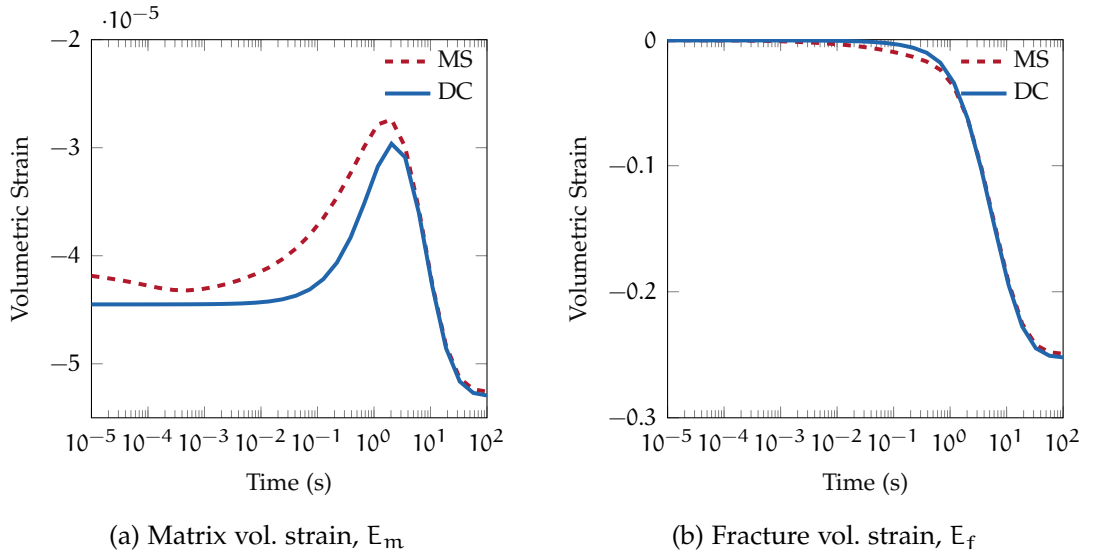
Figure 5.11: Matrix (a) and fracture (b) volumetric strain evolutions for the the material-induced anisotropy test case. 'MS' and 'DC' denote quantities related to microscale and dual-continuum models.

non-monotinicity, whilst the late-time matrix strain non-monotinicity for both approaches is much sharper.

Results in Figs. 5.10 to 5.11 can be explained by considering the material anisotropy in the fracture continuum. The smoother early-time non-monotinicity in MS matrix strain occurs because the vertical fractures are stiffer. These fractures then expand less with incoming fluid, reducing poroelastic coupling (and thus deformation) with the matrix compared to the isotropic case. As a result, since MS matrix pressure does not change significantly, the initial matrix pressures for the two modelling approaches are similar. This result suggests mechanical anisotropy can noticeably affect the degree of inter-continuum coupling. The delay in fracture pressure diffusion occurs due to the low vertical fracture permeability. Accordingly, we see the non-monotonic rise in matrix pressure with local inter-continuum equilibration processes occuring at similar timescales to macroscopic fracture flow. Further, the pseudosteady-state mass transfer assumption leads to the delayed response of this non-monotinicity in the DC model. The influx of fluid from the fractures into the matrix is accompanied by expansion of the matrix material, followed by contraction as fluid drains out (Fig. 5.11a).

The results in the current test show again how the DC model misses early-time effects due to local equilibration processes. Neglecting these local processes is implicit due to the microscopic steady-state pressure assumption made during homogenisation. However, once local equilibration is reached, the DC model does predict the general poroleastic behaviours of the MS model.

5.4 Conclusions

In this chapter, we used the numerical framework introduced in Chapter 4 to further study the links between micrscopic and dual-continuum models, given various modelling and material assumptions made on the former. We considered several tests, starting with a study on isotropic materials. Subsequently, we progressed to anisotropic cases where anisotropy was introduced at the microscale either geometrically or through property variations within the underlying material itself.

Overall, we observed that anisotropy can have measurable impacts on flow and deformation behaviour. However, we showed the DC approach is capable of capturing the global poroelastic behaviours for both isotropic and anisotropic MS equivalents. Discrepancies between the two model representations arise when local equilibration processes not accounted for in the homogenisation approach, are significant.

Following on from the discussions and numerical framework in Chapter 2 and Chapter 4 respectively, a natural extension to this work is to look at nonlinear behaviours. In particular, material nonlinearities arising from geometric nonlinearities at the microscale. Analytical methods such as those used here could provide a first approach to deriving such nonlinear effective constitutive models in simple cases. However, when such methods prove intractable, computational multiscale methods become attractive. Sequential multiscale strategies have been applied to single-continuum materials in Frey et al. (2013) and Van den Eijnden et al. (2016), and dual-continuum materials in Wang and Sun (2016, 2018, 2019). However, in these works the discretisation of choice is the finite-element method. Given the complexity of geological microstructures, it is interesting to leverage the capabilities of VEM (e.g. Rivarola et al. 2019). Further, to the best of the author's knowledge, little work has been done in applying sequential multiscale methods to frameworks involving mixed discretisations. Given the propensity for using dedicated software for the different subproblems it would be interesting to apply multiscale methods in these settings, exploring the various challenges and considerations therein.

Part III

Data-driven modelling

<div style="text-align: right; font-size: 3em; font-weight: bold; color: gray;">6</div>

Machine learning-based multiscale constitutive modelling

In this chapter we introduce and apply a machine learning-based approach to a hierarchical multiscale modelling problem. In Section 6.1, we start by providing the contextual motivation behind the work done in this chapter. In Section 6.2, we subsequently introduce the machine learning-based multiscale constitutive modelling framework. In doing, we describe the key components and considerations therein. We then apply this framework to a model problem. Accordingly, in Section 6.3 we introduce our problem of interest (modelling inter-continuum mass transfer). In Section 6.4, given the model problem we generate the data that will be used for training and testing the subsequent machine learning algorithms. In Section 6.5, we then introduce the learning algorithms used in this work. In Section 6.6, we show how we couple our data-driven model to a physics-based model for use in simulation, and demonstrate the resulting hybrid approach on several test cases. In Section 6.7, we finish with conclusions and recommendations for future work. The work done in this chapter can be found in:

<div style="text-align: center;">

`https://github.com/mashworth11/ML-MM`

</div>

6.1 Background

Throughout this thesis we have considered hierarchical multiscale problems. In these situations constitutive relations are needed at the macroscale to provide closure and information about the material in question. However, often these constitutive models are based on empiricism using simple considerations such as linearity (Weinan 2011). Whilst useful, these models can therefore be overly simple in many applications. This deficiency motivates the multiscale approaches reviewed in Chapter 1.

In situations where analytical methods are impractical or intractable, it is desirable instead to use multiscale algorithms (Matouš et al. 2017). Following on from the discussions in Chapter 1, machine learning offers exciting opportunities for further developments of computational multiscale approaches. For example,

in Alber et al. (2019) and Peng et al. (2020), the authors suggest the use of ML methods in multiscale domains for managing ill-posed problems, identifying missing information, quantifying uncertainty and as a means to bridge between scales. In this chapter we focus on the latter point, where ML is used to construct surrogate constitutive models to be used in sequential multiscale algorithms. In this context, we are interested in systems for which formulating a constitutive model is nontrivial. Examples of cases where we may meet such challenges are with systems exhibiting high-degrees of nonlinearity and/or time-dependence.

Data-driven approaches to generating surrogate constitutive models can be traced back several decades. For example, in the pioneering work of Ghaboussi et al. (1991) the authors used so-called neural networks to represent the constitutive behaviour of concrete under various loading conditions. From this and other similar early works (e.g. Goh 1995; Ghaboussi et al. 1998), users have incorporated data-driven surrogate models within multiscale modelling strategies for a variety of applications (e.g. Unger and Könke 2009; Hambli et al. 2011; Asproulis and Drikakis 2013). More recently, work has been done for modelling hysteretic constitutive information using so-called recurrent neural networks (Wang and Sun 2018; Ghavamian and Simone 2019). Despite the success of these recurrent algorithms for sequential modelling, they can be challenging to implement and to understand (Pascanu et al. 2013; Bai et al. 2018). Recently, Bai et al. 2018 showed that autoregressive algorithms can lead to superior performance compared to recurrent structures for a wide variety of sequence modelling tasks. Given the variety of multiscale problems and machine learning methods it would be useful to have a framework detailing the key questions and considerations for the generation and use of surrogate constitutive models within sequential multiscale approaches.

In the next part of this chapter we introduce and describe an ML-based multiscale modelling framework for hierarchical multiscale problems. We subsequently apply this framework to a model problem in which the widely adopted constitutive model is based on linearity of the quantities involved. More precisely, we look to address the problem of modelling inter-continuum mass transfer within dual-continuum models. The explicit time dependence of this process makes its implementation challenging in simulation. Subsequently, it is common to remove explicit time by modelling this process as a linear relation Eq. (2.7). Instead, in this chapter, we take a different and novel approach to representing this time-dependent process. Specifically, we model this process using machine learning. Accordingly, we remove explicit time-dependence by treating the problem as an autoregressive learning problem. Consequently, time-dependence is captured implicitly using quantities from previous timesteps that are readily available during simulation. Then, having learnt a surrogate constitutive model, we in-

corporate it within an uncoupled (flow only) version of the macroscopic numerical framework introduced in Chapter 4. We compare the resulting hybrid ML-physics model approach to the traditional physics-based approach using the linear constitutive model on several test cases.

6.2 Machine learning-based multiscale constitutive modelling framework

Here we introduce the ML-based multiscale constitutive modelling framework and the key concepts therein. The framework itself can be broken into three key components: Data generation, surrogate constitutive model learning and ML and physics model coupling (Fig. 6.1). However, we stress that these components are all interrelated and should be understood in parallel rather than in series.
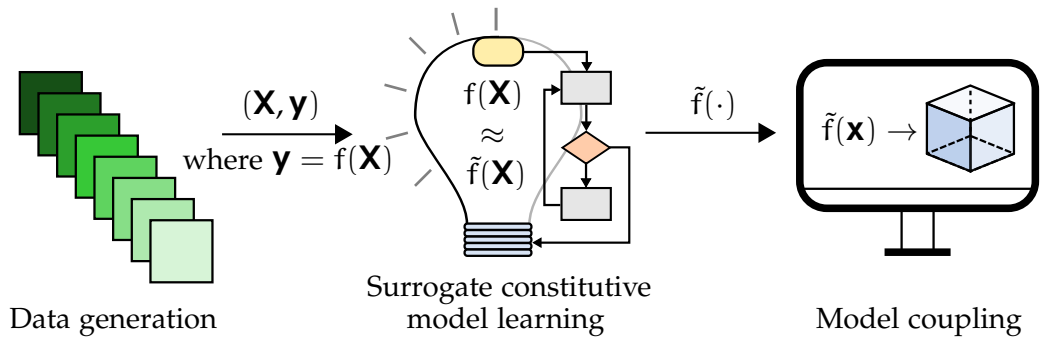
Figure 6.1: The machine learning-based multiscale constitutive modelling framework.

6.2.1 Data generation

Data generation is concerned with the question: How will we generate sample data for our learning algorithm? Microscale results can be expensive when numerically derived due to limited computational resources and/or high problem dimensionality. Managing this trade-off to ensure the dataset (sample set) is as informative as possible is referred to as experimental design (or design of experiments) (Razavi et al. 2012). Traditional approaches to experimental design involve the use of various sampling strategies (e.g. Monte Carlo, Latin hypercube, quasi-Monte Carlo methods) to build the dataset prior to learning. However, these so-called one-shot strategies can either contain too few samples for an accurate surrogate (undersampling) or more samples than we need, thus wasting precious resources (oversampling) (Xiao et al. 2018). An alternative to one-shot approaches is to use feedback from the ML training process to find samples that provide the maximum information gain when labelled and used to update the model. These so-called active learning (or sequential sampling) approaches can address the under/oversampling trade-off described previously (Crombecq 2011).

In addition to data-driven ML approaches, recent advances have seen the development of theory-driven ML approaches. Here the idea is to use physics such as partial differential equations, initial and boundary condition information, and symmetry or invariance properties (Ling et al. 2016; Wang and Sun 2018; Raissi et al. 2019; Zhu et al. 2019) to constrain the learning process. Accordingly, we can supplement missing or difficult to obtain data. Further, theory-driven approaches also act to regularise the learning process and ensure the physical consistency of our model. However, in this work we consider purely data-driven methods and save the incorporation of theory into the learning process for future studies.

6.2.2 Surrogate constitutive model learning

Surrogate constitutive model learning is concerned with the question: Given the properties of our data, the type of prediction problem and the end use for the resulting ML model, what is the most appropriate learning strategy to use? Training ML algorithms can be expensive from both data and computational points of view. If our sample set is poor, complex algorithms run the risk of failing to generalise when given new data (overfitting). Conversely, if our model is too simple we risk failing to extract meaningful relationships from our data (underfitting). Besides addressing underfitting and overfitting, we may also want algorithms that are intrinsically interpretable and quick to retrain in light of new data (e.g. linear regression, tree-based methods); give us an insight into aleatoric (data) and/or epistemic (model) uncertainties (e.g. Gaussian processes, Bayesian learning); and provide an embedded approach to feature (input) engineering in light of complex and/or high dimensional data (e.g. deep learning). Ultimately, within the context of multiscale modelling, the choice of learning method should be guided by considering the interdependence between data quality and availability, ML model accuracy and practicality, and the model's end use in physics-based simulation.

6.2.3 Model coupling

Model coupling is concerned with the question: How will we use our learnt constitutive model in our macroscopic physics simulator? Ideally, the ML model can be implemented within a numerical solver without significant intrusion. Accordingly, important considerations at this stage may be the accessibility of data during simulation to pass to the ML model; the time taken to predict by the ML model; how these predictions will be inputted into the numerical model; and in the case of nonlinear materials, how we extract state-dependent material properties such as permeability and stiffness from our surrogate constitutive

model. These latter points will depend on whether the constitutive model is to be used in an explicit or implicit manner. We describe the former, as those predictions made using previously observed and converged quantities. Subsequently, in a nonlinear solver the resulting surrogate constitutive model will only appear in the residual. Alternatively, if the prediction also depends on quantities at the current iteration level, parameters from the surrogate associated with these quantities will be needed in the Jacobian. For example, in Hashash et al. (2004) the authors consider nonlinear deformation problems and derive a closed-form expression for calculating the tangent stiffness tensor from a neural network. Accordingly, the authors provide consistent Jacobian entries for use in a Newton-Raphson scheme. For this work, our surrogate will be explicitly coupled due to the nature of the constitutive relation being injected. Nonetheless, the example above highlights the type of considerations we need to make in order to embed ML models within traditional physics-based simulations.

6.3 Multiscale problem setting: double-porosity mass transfer

Here we introduce an example of the type of multiscale problem that we wish to address with the framework described above. Subsequently, our model problem is that of inter-continuum mass transfer. In Section 5.3, we saw how the use of the linear constitutive model Eq. (2.7) can lead to the underprediction of matrix flux. As a result, we observe measurable errors in the flow behaviour when compared to a microscale simulation (Fig. 5.4). In the remainder of this section, we outline this problem in more detail.

6.3.1 Problem setup

Our model problem considers a two-dimensional domain, bounded on the east and west by a single fracture set. The north and south boundaries remain undrained (Fig. 6.2a). Initially, at time t_0 the matrix and fracture continua are in hydrostatic equilibrium (Fig. 6.2b). At a time t_{0+} we introduce an instantaneous step in the fracture pressure and let the matrix equilibrate due to inter-continuum mass transfer (Fig. 6.2b). Our goal is to see if we can capture these dynamics using a machine learnt surrogate constitutive model, and if it is an improvement over traditional linear transfer approximations (e.g. Warren and Root 1963).

The field equations are for the uncoupled dual-continuum mass balance equations introduced in Section 2.2.1, under the dual-porosity assumption. Accord-

(a) Problem geometry
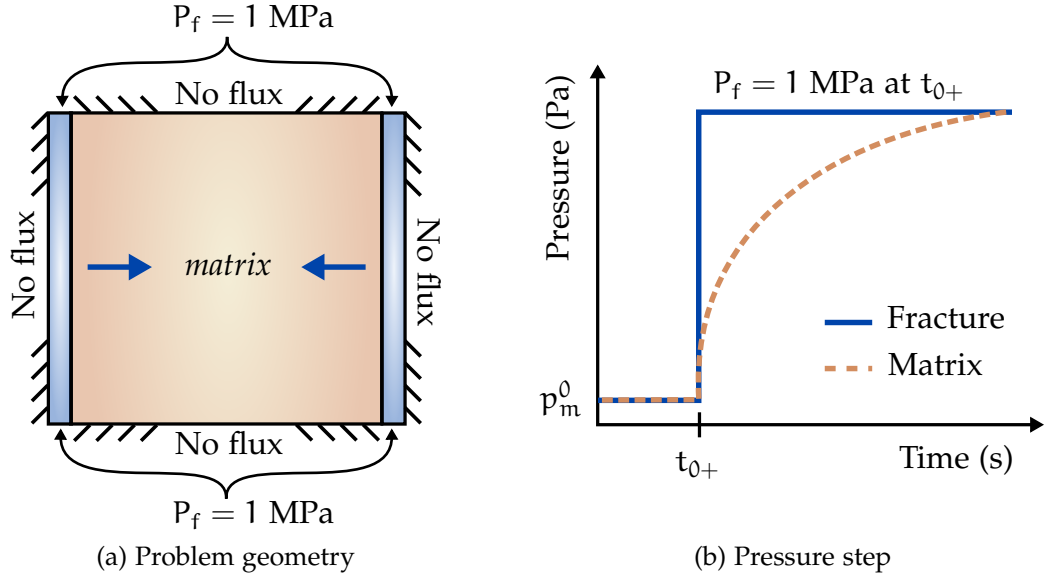
(b) Pressure step

Figure 6.2: Model problem setup including geometry (a) and the pressure step (b).

ingly, using Darcy's law, and the fluid and porosity compressibility relations in Eq. (2.9) and Eq. (2.11) respectively we recover the following

$$\phi_m^0 c_m \frac{\partial P_m(\mathbf{X}, t)}{\partial t} = \gamma_m(\mathbf{X}, t), \tag{6.1}$$

$$\phi_f^0 c_f \frac{\partial P_f(\mathbf{X}, t)}{\partial t} - \nabla \cdot \left(\frac{\mathbf{K}_f}{\mu_l} \cdot \nabla P_f(\mathbf{X}, t) \right) = -\gamma_m(\mathbf{X}, t), \tag{6.2}$$

where $c_\alpha = K_l^{-1} + K_{\phi,\alpha}^{-1}$.

The inter-continuum mass transfer term $\gamma_m(\mathbf{X}, t)$ is linked to the microscale according to the local matrix pressure diffusion given as

$$\varphi_m^0 c_m \frac{\partial p_m(\mathbf{x}, t)}{\partial t} = \nabla \cdot \left(\frac{k_m}{\mu_l} \nabla p_m(\mathbf{x}, t) \right), \tag{6.3}$$

assuming isotropic matrix material. We assume a separation of scales between the matrix, fracture and macroscopic scales (Royer et al. 1996), and thus consider an REV (or elementary cell) over our domain. We now link between micro and macroscales using the volume averaging operation, as done throughout this thesis. Applying Eq. (2.36) to Eq. (6.3) then leads to

$$\phi_m^0 c_m \frac{\partial \overline{p}_m(\mathbf{X}, t)}{\partial t} = \frac{1}{|\Omega^0|} \int_{\Omega_m} \nabla \cdot \left(\frac{k_m}{\mu_l} \nabla p_m(\mathbf{x}, t) \right) \, dV, \tag{6.4}$$

where we note $\overline{p}_m = P_m$. Following Eq. (6.4), $\gamma_m(\mathbf{X}, t)$ is defined as (Zimmerman et al. 1993),

$$\gamma_m(\mathbf{X}, t) = \phi_m^0 c_m \frac{\partial \overline{p}_m(\mathbf{X}, t)}{\partial t} = \frac{1}{|\Omega^0|} \int_{\partial \Omega_m} \left(\frac{k_m}{\mu_l} \nabla p_m(\mathbf{x}, t) \right) \cdot \mathbf{n} \, dS, \tag{6.5}$$

where we have used Gauss's theorem in defining Eq. (6.5). From Eq. (6.5), provided we can calculate the flux across the matrix we can calculate γ_m. This calculation could be done using numerical models. However, in this work we take a different approach: We find the analytical solution to Eq. (6.3), average this solution over our REV and insert the result in Eq. (6.5).

6.3.2 Analytical solution

To derive the analytical solution, we consider a 2D matrix block such as that shown in Fig. 6.2a subject to the following boundary and initial conditions:

$$p_m = \hat{p}_m \quad \text{on } \Gamma_m^p, \tag{6.6}$$

$$\mathbf{q}_m \cdot \mathbf{n} = \hat{q}_m \quad \text{on } \Gamma_m^q, \tag{6.7}$$

$$p_m(\mathbf{x}, t = 0) = p_m^0(\mathbf{x}) \quad \text{in } \Omega. \tag{6.8}$$

We consider a 1D diffusion problem such that $\hat{p}_m = P_f$ on the east and west boundaries, and $\hat{q}_m = 0$ on the north and south boundaries. Accordingly, the analytical solution to the described 1D diffusion problem is found in Crank (1979), and following averaging over the REV is given as

$$\overline{p}_m = p_m^0 + (P_f - p_m^0) \left\{ 1 - \sum_{n=0}^{\infty} \frac{8}{(2n+1)^2 \pi^2} \exp\left[\frac{-(2n+1)^2 \pi^2 k_m t}{\phi_m^0 \mu_l c_m \ell^2} \right] \right\}. \tag{6.9}$$

Differentiating Eq. (6.9) with respect to time leads to

$$\frac{\partial \overline{p}_m}{\partial t} = (p_m^0 - P_f) \sum_{n=0}^{\infty} \frac{8k_m}{\phi_m^0 \mu_l c_m \ell^2} \exp\left[\frac{-(2n+1)^2 \pi^2 k_m t}{\phi_m^0 \mu_l c_m \ell^2} \right], \tag{6.10}$$

with substitution of Eq. (6.10) into Eq. (6.5) giving γ_m. However, the resulting mass transfer expression is unsuitable for simulation purposes given the presence of explicit time and the infinite series. To alleviate these dependencies we can recover a first-order approximation to Eq. (6.10). Accordingly, taking the first term from Eq. (6.10) and eliminating t using the first term from Eq. (6.9) gives

$$\frac{\partial \overline{p}_m}{\partial t} = \frac{\pi^2 k_m}{\phi_m^0 \mu_l c_m \ell^2} (P_f - \overline{p}_m). \tag{6.11}$$

Substitution of Eq. (6.11) leads to the mass transfer model and shape factor shown in Eqs. (2.7) to (2.8) respectively. However, as shown in Section 5.3.1, use of this linear constitutive model can lead to measurable errors in flow behaviour. One common way to alleviate these inaccuracies is to use multi-rate transfer models (Haggerty and Gorelick 1995; Geiger et al. 2013). However, in this work

we treat the problem differently. The novelty here is to encode the complex, time-dependent function in Eq. (6.10) into a machine-learning model. The ML model is formulated without explicit time, using quantities directly available during simulation. Accordingly, our ML model is used as part of a sequential multiscale modelling strategy with machine learning to bridge the scales in the form of a surrogate constitutive model.

6.4 Application of the framework: data generation

We use machine learning to learn a mapping from quantities available during simulation to an output aligned with our constitutive property. To do so we consider a dataset $\mathcal{D}$ of n samples, $\mathcal{D} = \{(\mathbf{x}_i, y_i) \mid i = 1, ..., n\}$, where $\mathbf{x}_i \in \mathbb{R}^{d_{in}}$ is a vector of inputs and $y_i \in \mathbb{R}$ is a quantity derived from the microscale. Learning a mapping between inputs and outputs then equates to learning a function of the form

$$y_i = f(\mathbf{x}_i) \approx \tilde{f}(\mathbf{x}_i). \tag{6.12}$$

As a result, we can incorporate local scale physics, such as those coming from the analytical solution, or numerical simulations, within macroscopic models without having to formulate explicit phenomenological expressions.

We frame our learning problem considering the physics of the process, inputs coming from simulation and an output that is aligned with the discrete structure of the numerical problem. For the latter, we specify our output as the discrete equivalent to the continuous rate of change according to a backward Euler method commonly used for time discretisation in numerical modelling. Specifically

$$\frac{\partial \overline{p}_m}{\partial t} \approx \Delta_t \overline{p}_m(t+1) = \frac{\overline{p}_m(t+1) - \overline{p}_m(t)}{\Delta t} = y_i(t+1). \tag{6.13}$$

Our learning problem is formulated on the basis of time-series calculated using Eq. (6.9) and Eq. (6.13). Each individual time-series corresponds to a different initial matrix pressure p_m^0. We take 120 different p_m^0, sampled with logarithmic spacing from the interval of $[1, 1 \times 10^6]$ Pa. Every series starts from 0 and finishes at 100 s with a uniform stepping interval of 0.1 s. The remaining parameters in Eq. (6.9) are fixed as $k_m = 1$ md, $\phi_m^0 = 0.2$, $c_m = 1.4$ GPa^{-1}, $\mu_l = 1$ cp, $\ell = 1$ m and following the step in P_f at t_{0+}, $P_f = 1$ MPa. A plot of each series s as time vs $\mathbf{y}^s$ is shown in Fig. 6.3a. Further, Fig. 6.3b shows how this time-series data is split into training and testing data using a 2/3 : 1/3 split respectively. Accordingly, every third sequence corresponds to a test series. In the following section we describe how these series data are organised into $\mathcal{D}$. Specifically, how

we structure $\mathcal{D}$ will depend on our learning method of choice, as well as the need for any engineered features.

(a) Time-series data

(b) Train and test data split
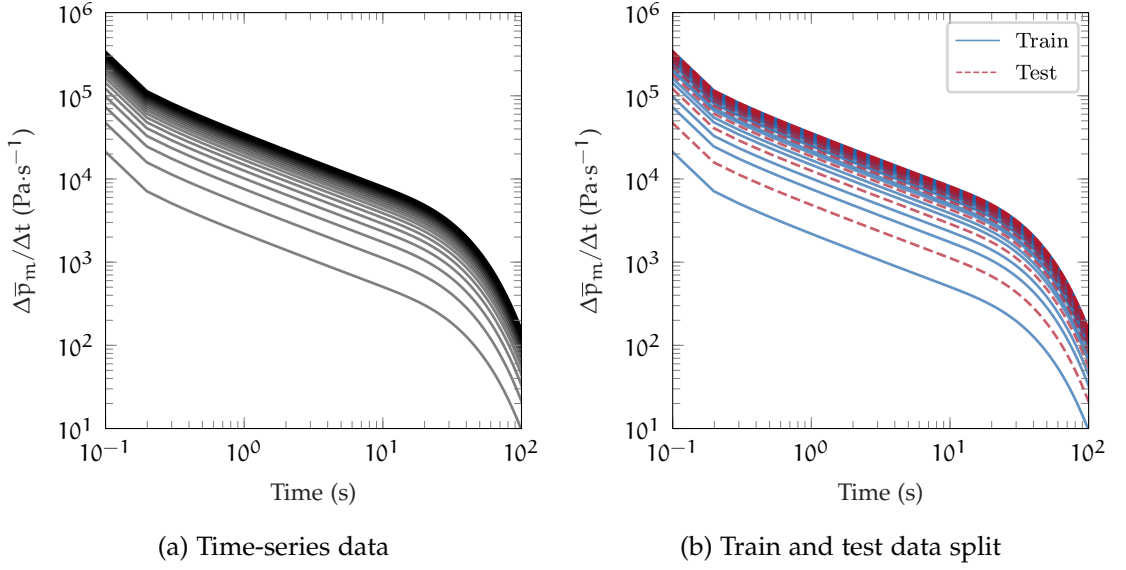
Figure 6.3: Time-series data (a) and training and test data split (b) for the learning problem.

6.5 Application of the framework: surrogate constitutive model learning

In the following we review the learning methods used to generate our surrogate constitutive model.

6.5.1 Autoregressive approaches

To account for the series nature of our data, we need a learning approach equipped to handle sequential dependencies. In the works of Wang and Sun (2018) and Ghavamian and Simone (2019), the authors used recurrent neural networks (RNN). Specifically, the authors use a variant of the RNN called a Long short-term memory (LSTM) network. The latter was developed to combat the difficulties in training conventional RNNs in the face of long-term sequential dependencies within series data. Further, LSTMs have been shown to give a state-of-the-art results for a variety of sequence modelling tasks (Chung et al. 2014; Jozefowicz et al. 2015). However, more recently, authors have found autoregressive approaches to be competitive and even outperform LSTMs for a variety of sequence modelling benchmarks (Lea et al. 2017; Bai et al. 2018). In a (multivariable) autoregressive setting $\tilde{f}(\cdot)$ uses previous series outputs to predict the next output in the series. Accordingly, for a two variable autoregressive model

$$\tilde{y}_i(t+1) = \tilde{f}[\mathbf{x}_i(t)] = \tilde{f}[\tilde{y}_i(t), ..., \tilde{y}_i(t-d_y+1), u_i(t), ..., u_i(t-d_u+1)], \quad (6.14)$$

where u denotes an external series, and d_y and d_u denote the number of sequence terms, or dependency length, for the internal and external series variables respectively. Here our external series is given as the difference between the boundary pressure P_f and $\overline{p}_m$ such that $u(t) = \Delta_p \overline{p}_m(t) = P_f - \overline{p}_m(t)$. The pressure difference acts as a driver for mass exchange, and at time t, indicates when a step in boundary pressure has occurred. Accordingly, we can learn to differentiate between early and late-time dynamics.

Following above, Gers et al. (2002) recommend autoregressive approaches using only short-term dependencies as a good starting point to time-series modelling. Accordingly, in the section to follow we consider two popular ML algorithms for autoregressive modelling given short histories. Specifically, polynomial regression (PR) and a fully-connected neural network (FC-NN). If longer histories are needed then more complex autoregressive architectures such as the convolutional neural network implemented by Bai et al. (2018), or the (recurrent) LTSM, can be used.

To train our algorithms we treat the training task as a *single-step ahead* prediction problem. In this strategy, the idea is to create $\mathcal{D}$ a-priori using lagged ground truths (targets) y in place of the predicted values $\tilde{y}$ in Eq. (6.14). Testing is then treated according to how the ML model will be used when coupled to the (macroscopic) simulator. That is, as a *multi-step ahead* prediction problem. Accordingly, predictions $\tilde{y}$ will be fed back into the algorithm to predict the next timestep, as per Eq. (6.14). This training and testing strategy can work provided the training error is sufficiently small such that accumulated errors do not explode when using the model as a multi-step ahead predictor.

Finally, under the autoregressive framework we express $\mathcal{D}$ as $\mathcal{D} = (\mathbf{X}, \mathbf{y})$ where $\mathbf{X} = [\mathbf{x}_1^1, \mathbf{x}_2^1, ..., \mathbf{x}_{1000}^S]^\top$ and $\mathbf{y} = [y_1^1, y_2^1, ..., y_{1000}^S]^\top$. Superscripts then denote the time-series label, with $S(= 120)$ being the total number of series, whilst subscripts denote the timestep within a given series.

6.5.2 Polynomial regression

Here we introduce the polynomial regression algorithm. These aglorithms are attractive because they are easy to understand and fast to train. The downside to these methods is the curse of dimensionality for large input vectors. Nonetheless, PR algorithms are a good place to start for many regression tasks, and serve as a good baseline model. Accordingly, under PR $\tilde{f}(\cdot)$ is formulated as

$$\tilde{y} = \tilde{f}(\mathbf{x}_i) = \mathbf{w}^\top \theta(\mathbf{x}_i), \tag{6.15}$$

where $\theta = [\theta_1, ..., \theta_{n_p}]$ is the vector of polynomial basis functions acting on $\mathbf{x}_i$ and $\mathbf{w} \in \mathbb{R}^{n_p}$ is a vector of weights (parameters) of the model. In this work we

use a second order polynomial transformation, which comes as a standard tool in many machine/statistical learning packages.

Whilst the inputs are polynomial (following a transformation) in Eq. (6.15), the weights remain linear. Finding $\mathbf{w}$ is simply then a linear regression problem and is the goal of training. In supervised learning problems, training corresponds to minimising a loss function $\mathcal{L}(\cdot)$ that represents the error in approximating $f(\cdot)$ by $\tilde{f}(\cdot)$ on our data. For the regression problem we use a squared loss such that

$$\mathcal{L}(\mathbf{w}) = \frac{1}{n}\|\mathbf{y} - \tilde{f}(\mathbf{\Theta}; \mathbf{w})\|_2^2, \tag{6.16}$$

where $\mathbf{\Theta} = [\theta(\mathbf{x}_1), \theta(\mathbf{x}_2), ..., \theta(\mathbf{x}_n)]^\top$. Finding the optimal set of weights that minimise Eq. (6.16) is defined formally as

$$\underset{\mathbf{w}}{\arg\min}\, \mathcal{L}(\mathbf{w}) = \underset{\mathbf{w}}{\arg\min}\, \frac{1}{n}\|\mathbf{y} - \tilde{f}(\mathbf{\Theta}; \mathbf{w})\|_2^2. \tag{6.17}$$

The squared loss in linear regression is a convex function which admits a global minimum in $\mathbf{w}$ at the point $\nabla \mathcal{L} = 0$. Accordingly

$$\mathbf{\Theta}^\top \mathbf{\Theta} \mathbf{w} = \mathbf{\Theta}^\top \mathbf{y}, \tag{6.18}$$

leading to

$$\mathbf{w} = \mathbf{\Theta}^\dagger \mathbf{y}, \tag{6.19}$$

where $\mathbf{\Theta}^\dagger = (\mathbf{\Theta}^\top \mathbf{\Theta})^{-1} \mathbf{\Theta}^\top$.

PR is well known to suffer from high degrees of multicollinearity (Dalal and Zickar 2012). As a result, $\mathbf{\Theta}^\top \mathbf{\Theta}$ is ill-conditioned and the solution in Eq. (6.19) is non-unique. For prediction problems such ill-conditioning is generally not a concern (Dormann et al. 2013), since new data comes from the same population as the training data. However, for problems of extrapolation such as multi-step ahead prediction, collinearity between inputs can change due to accumulating errors. Such changes can affect predictions on models arising from ill-conditioned matrices and should be addressed (Dormann et al. 2013). We therefore address multicollinearity between inputs using regularisation, which aims to restrict the space of viable models that fit our data (e.g. in the face of ill-conditioning). There are various forms of regularisation, however in this work we use pivoted QR factorisation (Strang 2019). This method is implemented as standard in MATLAB's linear solver. The benefits of the pivoted QR approach are that it yields parsimonious models and is relatively cheap to compute (Strang 2019). Note, we also found ridge regression (an L2 norm penalty on the weights) to work equally well, but chose the pivoted QR method purely for convenience.

6.5.3 Fully-connected neural networks

Here we introduce the fully-connected neural network model. Aside from the FC-NN considered here, neural networks more generally have become a popular choice for surrogate modelling due to their great flexibility, scalability and significant advancement within research communities. Further, contrary to the polynomial regression where the feature transforms are defined a-priori, in neural networks these transformations are implicit within the algorithm and learnt from the data.

To proceed, within an FC-NN information is fed forward from an input layer ($l = 0$) through hidden layers ($l = 1, ..., L-1$) finishing at an output layer ($l = L$). Accordingly, under an FC-NN $\tilde{f}(\cdot)$ is formulated as

$$\tilde{y} = \tilde{f}(\mathbf{x}_i) = s^{[L]}\left(s^{[L-1]}\left(...\left(s^{[1]}(\mathbf{x}_i)\right)...\right)\right). \tag{6.20}$$

For a given layer $0 < j$, $s^{[j]}$ is given as an affine transformation followed by an element-wise nonlinear function such that

$$s^{[j]}(\mathbf{x}) = h^{[j]}\left(\mathbf{W}^{[j]\top}\mathbf{x} + \mathbf{b}^{[j]}\right), \tag{6.21}$$

where $\mathbf{W}^{[j]} \in \mathbb{R}^{n_{j-1} \times n_j}$ and $\mathbf{b}^{[j]} \in \mathbb{R}^{n_j}$ are the weight matrix and bias parameter vector associated with layer j respectively. Evidently, for the univariate prediction considered herein, the weight matrix for the last layer will be a weight vector $\mathbf{W}^{[L]} = \mathbf{w}^{[L]}$. Notation $h(\cdot)$ is the nonlinear function referred to as an activation function. In this work, we take $h^{[L]}$ as a linear activation and all others as so-called rectified linear units. In training the FC-NN our objective is to minimise a squared loss of the form

$$\mathcal{L}(\lambda) = \frac{1}{n}\|\mathbf{y} - \tilde{f}(\mathbf{X}; \lambda)\|_2^2, \tag{6.22}$$

where $\lambda = [\mathbf{W}^{[1]}; \mathbf{b}^{[1]}, ..., \mathbf{W}^{[L]}; \mathbf{b}^{[L]}]$. However, unlike Eq. (6.17), with neural networks the loss function is non-convex. As a result, weights and biases are updated iteratively using a chosen optimiser together with the backpropogation algorithm. In this work, we found stochastic gradient descent with Nesterov momentum to work the best. Finally, we implement the FC-NN using the Keras API.

6.5.4 Training and testing

In the following we present further details and results for the single-step ahead (training) and multi-step ahead (testing) prediction problems.

Considerations

To train our models we consider a dependency length of $d_y = 2$ in order for our problem to be well-defined. With $d_y = 2$, we use $d_u = 3$ given that three pressure steps make up the two difference steps $\Delta_t \overline{p}_m$. Although not studied in detail here, d_y (resp. d_u) is a hyperparameter that can be tuned according to the trade-off between gain in accuracy and complexity.

For the polynomial regression, to highlight the effects of multicollinearity, we present results both with and without regularisation. For the FC-NN we trained our model using a batch size of 64 over 500 epochs. We experimented with various model depths and widths, and found the best results came using a simple single hidden layer FC-NN with 20 hidden units. Additionally, with this architecture there was little overfitting, and hence no need for regularisation. Finally, to evaluate between the different models we consider one minus the normalised root-mean-square error given as

$$1 - \text{NRMSE} = 1 - \frac{\text{RMSE}}{\text{SD}} = \frac{\sqrt{(n)^{-1} \sum_{i=1}^{n} (y_i - \tilde{y})^2}}{\sqrt{(n-1)^{-1} \sum_{i=1}^{n} (y_i - \overline{y})^2}}, \qquad (6.23)$$

where SD and $\overline{y}$ represent the sample standard deviation and mean of the target set respectively. From Eq. (6.23) the closer the value to one, the more accurate the algorithm.

Results

Fig. 6.4 shows the train and test results using the unregularised polynomial regression algorithm. From Fig. 6.4a we can see there is a good match when training as a single-step ahead prediction problem. The quality of this match is corroborated by the high evaluation metric (and low RMSE respectively) shown in Table 6.1. However, Fig. 6.4b shows for lower initial rates of change (associated to higher initial pressures) the prediction is extremely poor giving rise to large positive and negative values. Accordingly, the evaluation metric for this test is unbounded resulting in the missing entry shown in Table 6.1. Even for higher initial rates of pressure change, the early-time results in Fig. 6.4b show the unregularised PR begins to underpredict the rates of change after a few timesteps. Interestingly however, the prediction seems to recover from mid to late times. We hypothesised these errors to be caused by the multicollineriaty existing between the transformed features, as described in Section 6.5.2. Accordingly, to address this problem we introduced a regularised PR by way of a pivoted QR factorisation.

Results for the regularised PR are shown in Fig. 6.5 and Table 6.1. The training results shown in Fig. 6.5a are identical to those shown in Fig. 6.4a for the unreg-

(a) Single-step ahead (train) (b) Multi-step ahead (test)
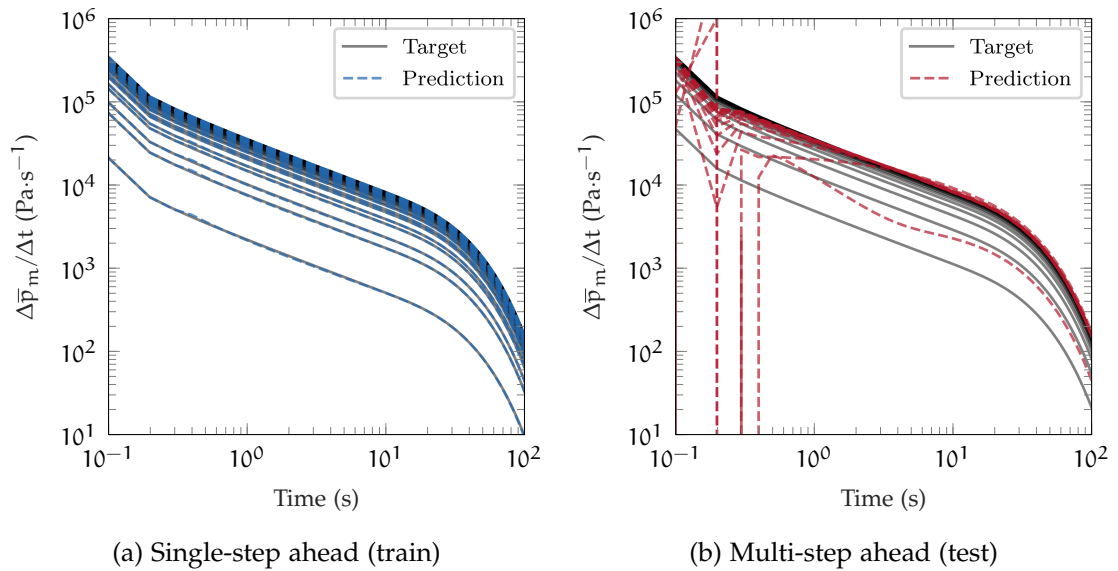
Figure 6.4: Single-step ahead training (a) and multi-step ahead testing (b) using unregularised polynomial regression.

(a) Single-step ahead (train) (b) Multi-step ahead (test)
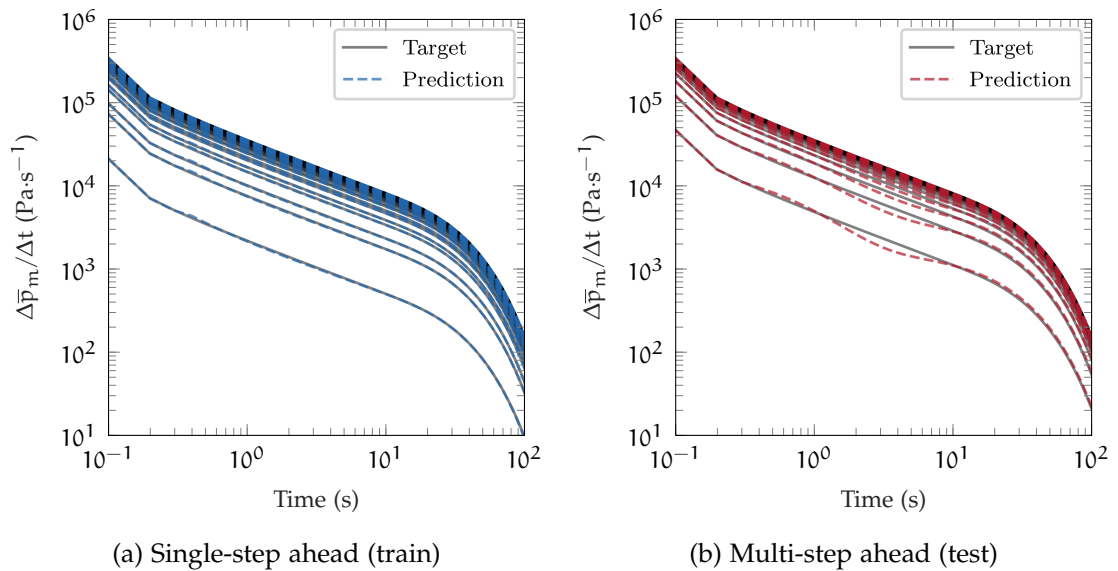
Figure 6.5: Single-step ahead training (a) and multi-step ahead testing (b) using regularised polynomial regression.

ularised PR case (Table 6.1). However, we can observe significant differences on the multi-steap ahead test between the two polynomial regression models. From Fig. 6.5b we see that the regularised PR predictions are very close to the targets. We see slight discrepancies observable at middle times, in particular for those series corresponding to low initial rates of pressure change. However, these discrepancies diminish toward late times as the predictions converge back to the target. We hypothesise that it will be possible to remove these small discrepancies altogether using even longer dependencies (and possibly more complex algorithms) than those considered currently.

Lastly, Fig. 6.6 and Table 6.1 show the train and test results using the FC-NN. From Fig. 6.6a we see a good match between the training predictions and target.

(a) Single-step ahead (train) (b) Multi-step ahead (test)
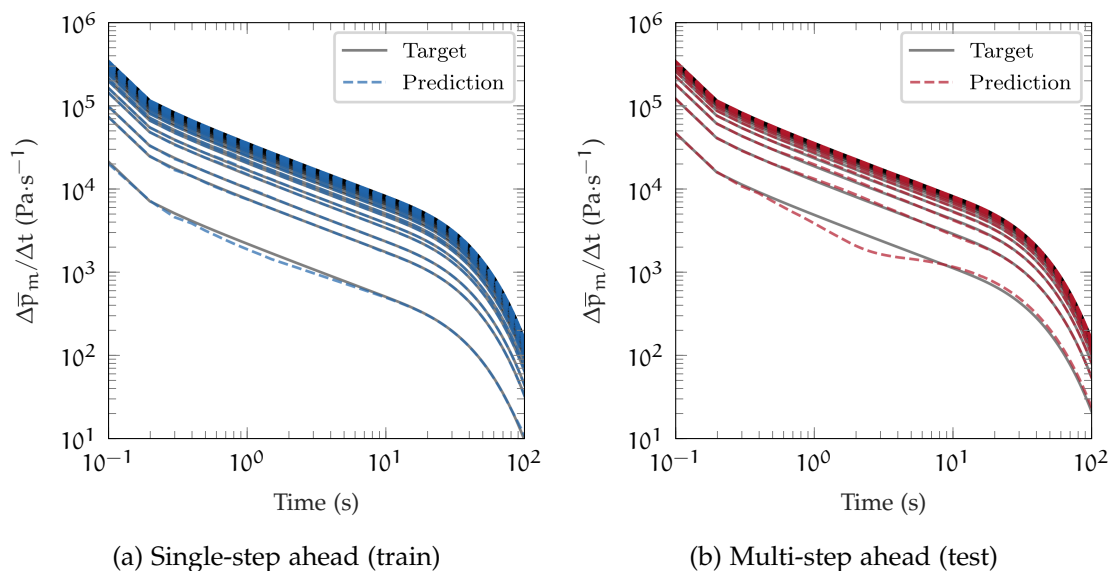
Figure 6.6: Single-step ahead training (a) and multi-step ahead testing (b) using the fully-connected neural network.

However, for the time-series corresponding to the lowest initial rate of change we can see a slight discrepancy in the match during middle-times. Fig. 6.6b shows this discrepancy to lead to a noticeable mismatch between the predictions and the target for this test series during the multi-step ahead test. However, despite the observed discrepancy, Table 6.1 shows the overall performance of the FC-NN to be superior to the regularised PR during testing, as indicated by the higher evaluation metric (and lower RMSE respectively). This result, whilst also comparing Fig. 6.6b to Fig. 6.5a, suggests the performance of the FC-NN in regions of higher data density to be superior to that of PR. For our dataset, regions of higher data density correspond to series with high initial rates of change. In these regions, we expect the errors of the linear transfer to be high compared to when the initial rate of change is small (initial matrix pressure is close to the fracture pressure). Accordingly, the accuracy of the FC-NN compared to PR in modelling otherwise challenging regions for the linear transfer model, makes it preferable for use in the next step of the multiscale framework.

Algorithm	$(RMSE)_{train}$	$(1 - NRMSE)_{train}$	$(RMSE)_{test}$	$(1 - NRMSE)_{test}$
UPR	21.4	0.999	–	–
RPR	21.4	0.999	152	0.991
FC-NN	28.1	0.998	99.7	0.994

Table 6.1: Train and test evaluations for the different learning algorithms. UPR, RPR and FC-NN denote the unregularised and regularised polynomial regression, and fully-connected neural network respectively. The missing entry for UPR on the test is due to the unbounded predictions.

To summarise, for multi-step ahead prediction problems we need to be wary of accumulating errors introduced during simulation. This problem was shown

to be bad for a PR model suffering from high multicollinearity. Accordingly, for PR we had to address this problem explicitly using regularisation. However, for the FC-NN, multicollinearity seemed to be handled implicitly by the model. Further, the FC-NN was shown to perform better than PR in the regions where we would expect to have the highest error when using a linear transfer model. Given the performance of the FC-NN herein, its robustness within the multi-step ahead setting, and the general flexibility of neural network architectures for further extensions (e.g. theory-driven ML), we choose this model as our surrogate constitutive model for further use.

6.6 Application of the framework: model coupling

Here we couple our trained surrogate constitutive model to a macroscopic physics-based model. We test the subsequent hybrid ML-physics against a traditional physics-based model using the linear transfer and a microscale model, for a variety of different test cases.

6.6.1 Hybrid ML-physics model

With the trained ML model we now look to couple it to a physics-based model. Given the propensity for nonlinear phenomena in a variety of physics settings including subsurface flow it is common to use nonlinear solvers. Accordingly, following Eq. (4.24) we give Eqs. (6.1) to (6.2) in discrete block matrix as

$$
\begin{bmatrix} \mathbf{F}_m & \mathbf{G}_m \\ \mathbf{G}_f & \mathbf{F}_f \end{bmatrix}^{(k)} \begin{bmatrix} \delta \tilde{\mathbf{P}}_m \\ \delta \tilde{\mathbf{P}}_f \end{bmatrix}^{t+1,(k+1)} = - \begin{bmatrix} \mathbf{R}_m \\ \mathbf{R}_f \end{bmatrix}^{t+1,(k)}. \tag{6.24}
$$

Without mechanics the flow matrix for continuum α is $\mathbf{F}_\alpha = \mathbf{Q}_\alpha + \Delta t \mathbf{T}_\alpha$, where $\mathbf{Q}_\alpha$ is the compressibility matrix and $\mathbf{T}_\alpha$ is the transmissibility matrix (see Lie 2019 for details). For the matrix material in the dual-porosity setting, the transmissibility matrix has zero entries. Matrix $\mathbf{G}_\alpha$ is the coupling matrix arising from an inter-porosity flow expression such as the linear approximation in Eq. (2.7). Notation $\delta \tilde{\mathbf{P}}_\alpha^{t+1,(k+1)}$ are as described in Eq. (4.25). Lastly, $\mathbf{R}_\alpha^{t+1,(k)}$ is the residual vector such as that in Eqs. (4.22) to (4.23). Intuitively, $\mathbf{R}_\alpha^{t+1,(k)}$ provides the difference between the rate of change of fluid mass within a volume to that generated by sources and/or fluid movement through its boundaries at iteration level k. Finally, we inject our machine learning model into Eq. (6.24) through an explicit approach. As a result, following a Newton iteration the coupling matrices $\mathbf{G}_\alpha$ in Eq. (6.24) are zero entries, whilst the prediction for γ_m appears in the residuals.

6.6.2 Tests

To test the hybrid ML-physics model we consider several realisations of the 1D diffusion problem described in Section 6.3.1. For these realisations, we test our framework on initial and boundary conditions not used for training our model. Further, we also consider an application of the framework to a geological model. For the former, we compare the hybrid approach against a microscale model and a physics-based model using the first-order mass transfer constitutive relation. For brevity in the remainder of this section, we refer to the latter method as the 'traditional' approach to dual-continuum modelling. Lastly, for the geological model case, we compare only the hybrid and traditional dual-continuum approaches.

For the 1D problem test cases we discretise the DC problem using a single element. For the microscale model we resolve the matrix using 40 elements along the first principal axis. Within the DC model we initialise the fracture pressure as $P_f^0 = 1$ MPa. Further, to mimic the fracture boundary within the DC model, we set fracture permeability to 10 d. As a result, the fracture pressure equilibrates almost instantaneously with the external boundary in response to changes induced by inter-continuum flow. The remaining properties are as described in Section 6.4. Specifically, $\phi_f^0 = 1 \times 10^{-3}$, $c_f = c_m = 1.4$ GPa^{-1}, $\phi_m^0 = 0.2$, $\mu_l = 1$ cp, $N_f = 1$, $\ell = 1$ m and $k_m = k' = 1$ md . With respect to ϕ_f^0 and c_f these are chosen somewhat arbitrarily since we do not consider fracture dynamics for the problems herein. Lastly, to interpret micro and macro matrix pressure results we make use of the considerations and averaging operation introduction in Section 5.2.

For the geological model, we use the same model as considered in Chapter 4. Accordingly, each REV now corresponds to a 3D domain involving three orthogonal fracture sets leading to a 3D diffusion problem within the matrix. As a result, the analytical solution used to generate data is slightly different to Eq. (6.9). Further details of this solution, and the parameterisations used for this test, are described below.

Case 1: $p_m^0 \in [1, 1 \times 10^6]$ Pa

For the first set of tests we consider two initial pressures not used when constructing $\mathcal{D}$, but coming from $[1, 1 \times 10^6]$ Pa. Specifically, we sample the initial pressures such that $p_m^{0,I} < 10$ Pa and 0.1 MPa $< p_m^{0,II}$, where superscripts I and II correspond to the two tests respectively. The boundary pressure is fixed as $P_f = 1$ MPa.

Case 2: $P_f \in \{2, 8\}$ MPa

Here we consider tests where we extrapolate outside of the training set by using different conditions to those used during training. In this case we are interested in cases with boundary pressures $P_f > 1$ MPa. Accordingly, we consider two tests where we set $P_f = 2$ MPa and $P_f = 8$ MPa. The initial matrix pressure is set as $p_m^0 = 1$ Pa, whilst the rock and fluid properties are as described for the other 1D diffusion test cases.

Case 3: Application to a geological model

Following Eqs. (6.6) to (6.8), the 3D diffusion problem is described such that $\hat{p}_m = P_f$ on all the boundaries of a 3D matrix block. In this case the analytical solution for the resulting diffusion problem is given as (Lim and Aziz 1995),

$$\overline{p}_m = p_m^0 + (P_f - p_m^0) \left\{ 1 - \sum_{n=0}^{\infty} \frac{(8/\pi^2)^3}{(2n+1)} \exp\left[\frac{-3(2n+1)^2\pi^2 k_m t}{\phi_m^0 \mu_l c_m \ell^2} \right] \right\}, \quad (6.25)$$

where we parameterise Eq. (6.25) using $P_f = 1$ MPa, $c_m = 3$ GPa^{-1}, $\phi_m^0 = 0.2$, $\mu_l = 5$ cp, $\ell = 1$ m and $k_m = 1 \times 10^{-4}$ md. As before, we take 120 different p_m^0 sampled from the interval $[1, 1 \times 10^6]$ Pa. Further, we generate a series corresponding to 100 hours where $t_{0+} = 0$ and $\Delta t = 1$ hour. Finally, we train and test on the resulting data using an FC-NN, which is subsequently injected into our physics-based simulator.

For the geological model, we initialise the fracture pressure as $P_f^0 = 1$ MPa and specify the permeability as 10 d. The boundaries of the model are then specified as pressure boundaries set at 1 MPa. Accordingly, the high fracture permeability and initial conditions ensures our test problem is consistent with our learning problem. We initialise the matrix as $p_m^0 = 1$ Pa. Finally, to complete the DC model we assign $\phi_f^0 = 1 \times 10^{-3}$ and $c_f = 3$ GPa^{-1}.

We compare results over the geological model between the hybrid ML-physics model and the physics-based model using the linear transfer. For the latter, the transfer function is parameterised using $N_f = 3$ and $k' = 1 \times 10^{-4}$ md. Finally, despite only training for a series corresponding to 100 hours we run each simulation for a 1000 hours, thus extrapolating outside of the training conditions.

6.6.3 Results

Here we present the matrix pressure evolution results for the test cases described above.

Case 1: $p_m^0 \in [1, 1 \times 10^6]$ *Pa*

Results for the first test case are shown Fig. 6.7. In all cases we see pressure increasing with time as the matrix equilibrates with the boundary pressure. We can see for both tests there is a measurable discrepancy between the DC model using a linear transfer and the equivalent microscale description. This discrepancy is particularly pronounced for test I (Fig. 6.7a). For this test case, the linear transfer is a particularly poor early-time model when the difference between continuum pressures is several orders of magnitude. In contrast, the DC approach with the ML transfer produces high quality matches for both test cases without the computational expense taken to run the microscale models. In Fig. 6.5b we observed small errors in the middle-time FC-NN predictions for test series corresponding to low initial rates of change. However, Fig. 6.7b shows despite these discrepancies, the FC-NN still outperforms the linear transfer model with respect to the microscale solution.

(a) $p_m^{0,I} = 3$ Pa

(b) $p_m^{0,II} = 0.8$ MPa

Figure 6.7: Average matrix pressure evolutions for test case 1 with $p_m^{0,I} = 3$ Pa (a) and $p_m^{0,II} = 0.8$ MPa (b). Notations 'DC-L' and 'DC-ML' denote the dual-continuum model equipped with the linear and machine learning constitutive transfer models respectively.

Lastly, for both tests we also provide the analytical solutions (Fig. 6.7). The benefit of this addition is most clear from from Fig. 6.7a. From Fig. 6.7a we observe a small discrepancy between the microscale model and the analytical solution for the first few timesteps. This discrepancy arises due to the timestep discretisation error in the microscale model. Remarkably, we do not see this discrepancy between the ML-based approach and the analytical solution, since the learnt model comes from data unaffected by these discretisation errors. This subtle result corroborates the aim of multiscale approaches. Specifically, to combine

the accuracy of microscopic representations with the practicality of macroscopic models.

Case 2: $P_f \in \{2, 8\}$ *MPa*

Results for the second test case are shown in Fig. 6.8. As before we see pressure increasing with time in response to the pressure step. Similar to Fig. 6.7a, Fig. 6.8 shows the DC model with the linear transfer to underpredict early time average pressure by up to an order of magnitude. However, despite not having learnt with data containing such a big pressure jump, the hybrid ML-physics approach still manages a good match to the microscale results across the whole time range. These results thus suggest some form of self-similarity in the solution that is well approximated by the learnt model. Generalisability such as that shown in Fig. 6.8 is highly desirable, although perhaps more difficult to obtain in more complex scenarios. In this regard, theory-driven ML approaches have been shown to have good generalisibility performance compared to purely data-driven methods (Zhu et al. 2019; Wang, Zhang, Chang and Li 2020; Wang, Kashinath, Mustafa, Albert and Yu 2020). Accordingly, it is interesting to incorporate these techniques in future work.
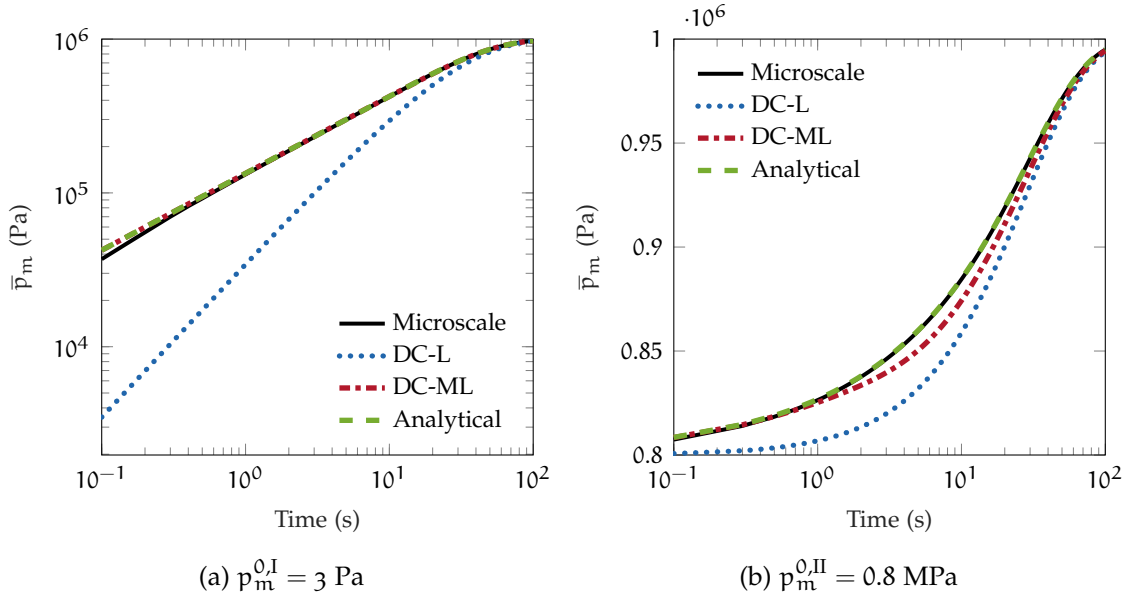

(a) $P_f = 2$ MPa   (b) $P_f = 8$ MPa
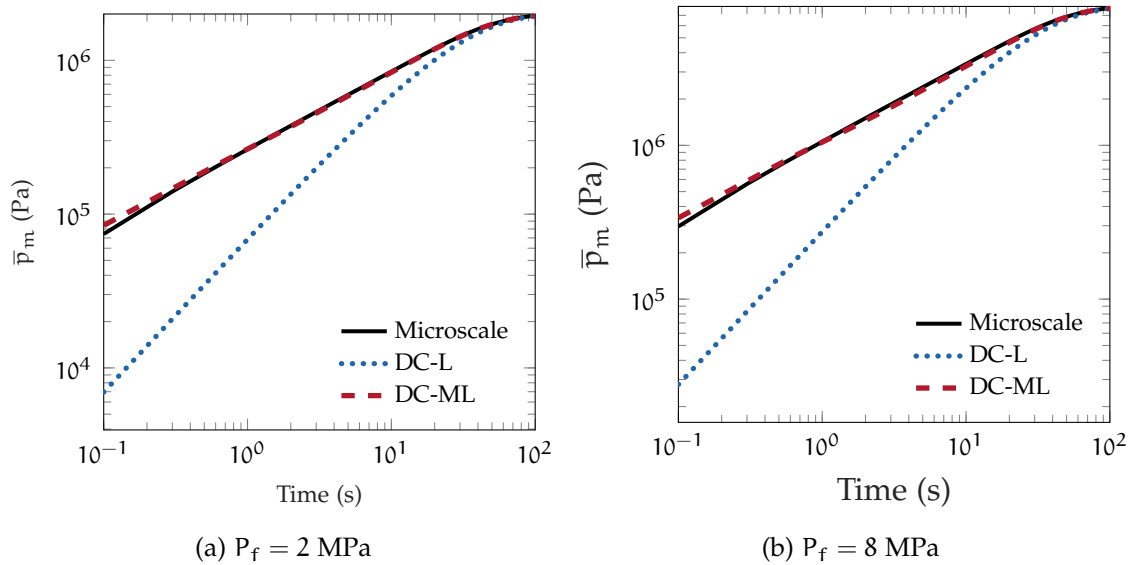
Figure 6.8: Average matrix pressure evolutions for test case 2 with $P_f = 2$ Pa (a) and $P_f = 8$ MPa (b). Notations 'DC-L' and 'DC-ML' denote the dual-continuum model equipped with the linear and machine learning constitutive transfer models respectively.

Case 3: Application to a geological model

Figs. 6.9 to 6.10 show the results for the geological model test case using the traditional and ML-physics model respectively. In both figures we can see matrix

pressure rising over time in response to diffusion driven equilibration with the fractures. However, we can see significant differences between the two modelling approaches following the initial conditions up until equilibrium conditions. Comparing Figs. 6.9 to 6.10 at t = 1 hour, we can see the matrix pressures are noticeably higher when using the hybrid ML-physics approach. This observation is consistent with the results in the previous test which showed the matrix pressures to be significantly underestimated when using a linear approximation. Accordingly, matrix fluxes are underpredicted when using this approach. Such errors could be significant in geological settings such as groundwater remediation (Haggerty and Gorelick 1995). Similar differences between the two approaches to those just described are observed at t = 50, 100 hours, with the ML-physics approach predicting higher pressures than the traditional approach.
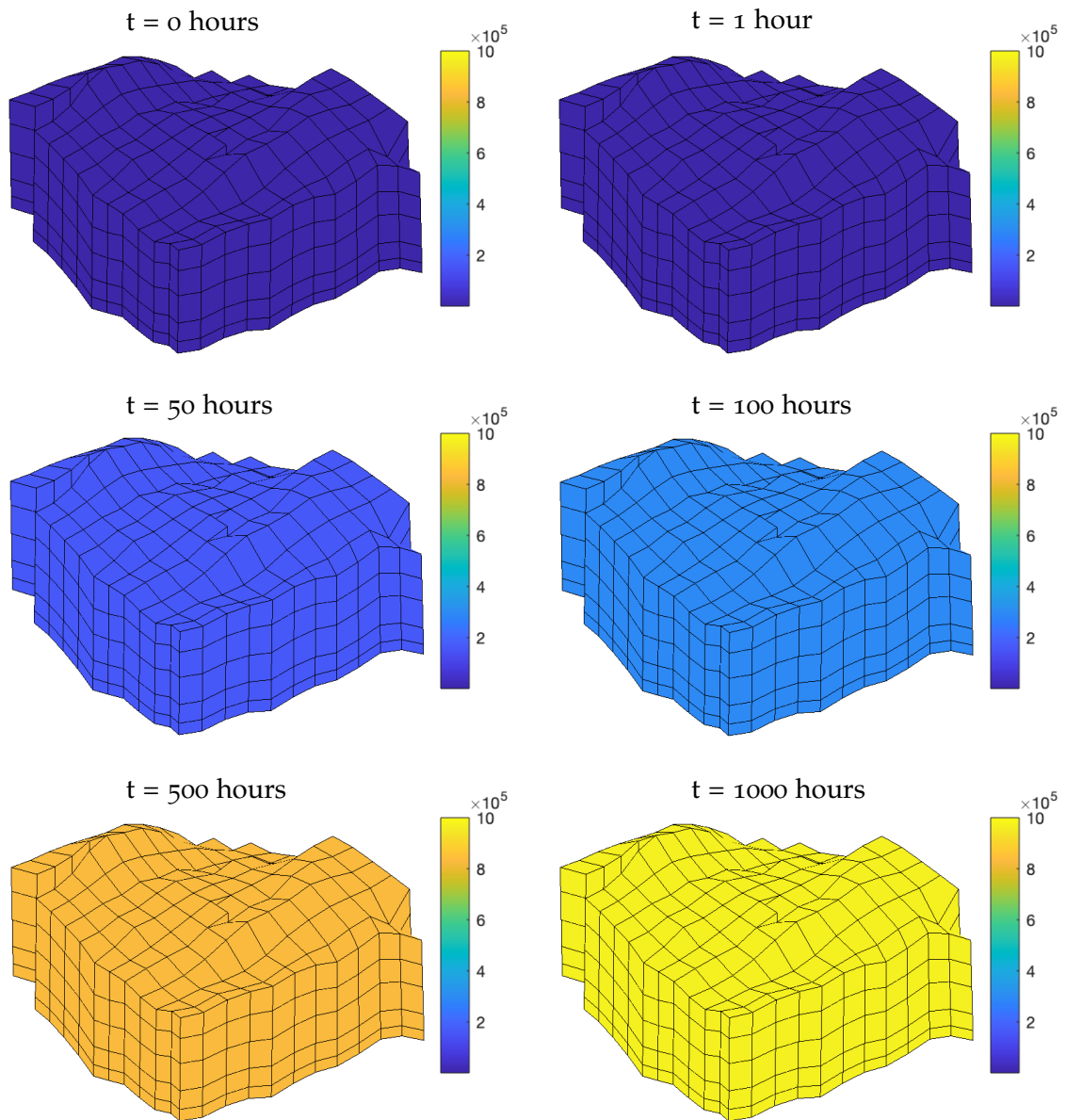
Figure 6.9: Matrix pressure evolutions on a geological model using the linear transfer model.
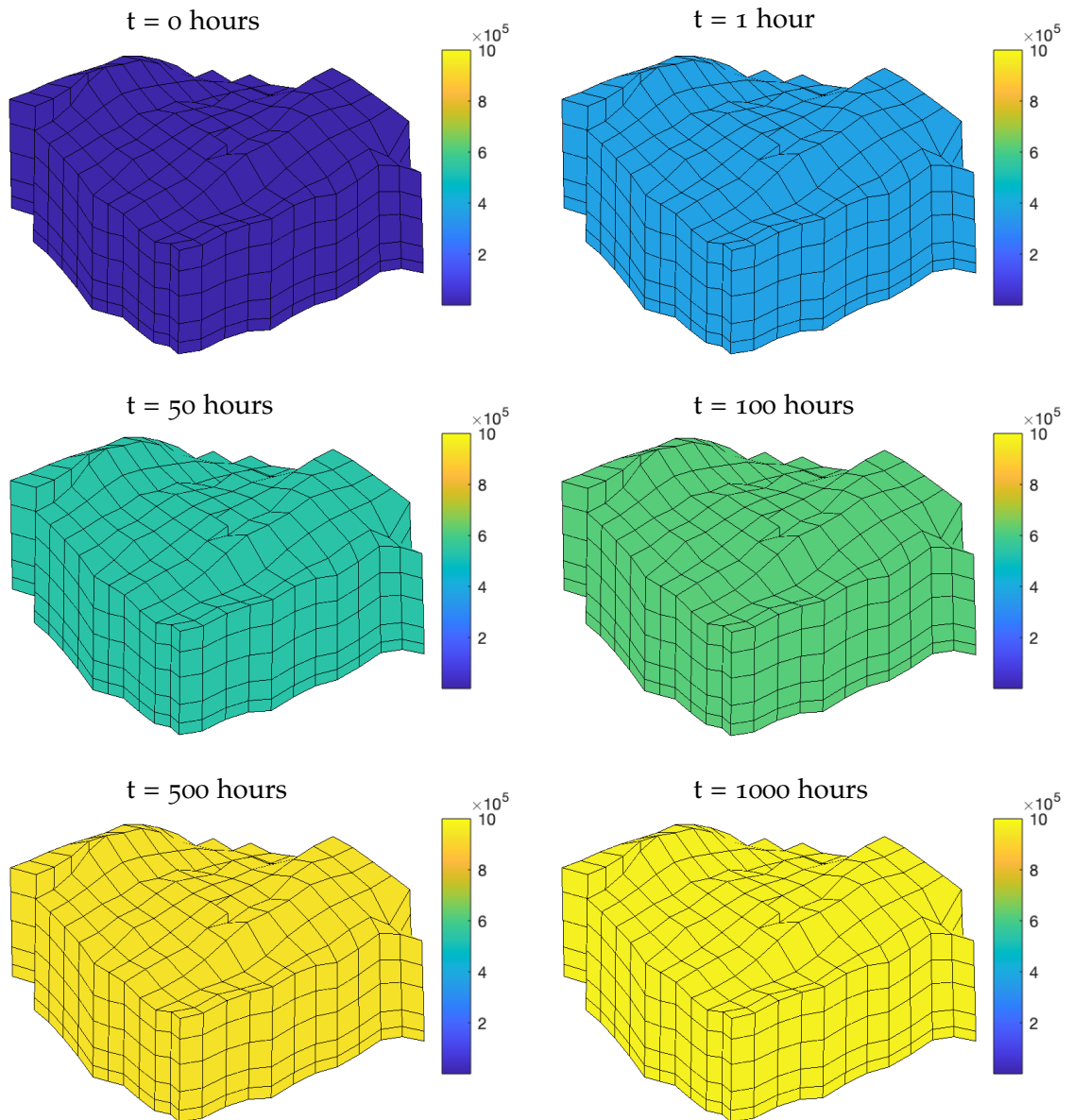
Figure 6.10: Matrix pressure evolutions on a geological model using the machine learning-based transfer model.

When extrapolating outside of the training conditions, the hybrid approach shows physically reasonable results (consistent with the previous timesteps) at t = 500 hours. Accordingly, at this timestep, matrix pressures coming from the hybrid approach are higher compared to the traditional approach. However, by t = 1000 hours, the two models have converged to the equilibrated pressure state. This last result shows the hybrid approach is capable of converging to an equilibrated state.

In summary, the results presented for the described tests show the potential for the ML-physics approach for multiscale modelling. With this framework we can capture the accuracy of microscopic representations with the practicality of macroscopic models. Although we consider relatively simple examples in this work, a number of interesting extensions could be investigated using this hybrid approach.

6.7 Conclusions

This chapter introduces and applies a machine learning-based multiscale constitutive modelling framework. We detail the key components of the framework as: data generation, surrogate constitutive model learning and ML-physics model coupling. In doing, we describe various considerations that the user should make at each step. To test the framework we consider a model multiscale pressure diffusion problem. Specifically, that of inter-continuum mass transfer in double-porosity materials. In practice, it is common to describe this constitutive relation using a simple linear model. When applying the framework we introduce the various machine learning methods used to create the surrogate constitutive model. We account for time-dependence using autoregressive approaches, considering both polynomial and neural network regressors. We found the latter to be more robust and give higher accuracy when used as a multi-step ahead predictor. Accordingly, we integrated the resulting data-driven surrogate into a physics-based model, creating a hybrid ML-physics approach. We showed the resulting hybrid approach to give high quality results for a number of test cases compared to the traditional approach based on the linear constitutive model.

There are a number of exciting possibilities for future work. We hypothesise the real benefit of this framework to come when using data coming from more complex microscale scenarios (e.g. dynamic boundary conditions) than the ones considered here. In such cases data is likely to be obtained numerically. However, numerical data can be expensive, leading to sparse datasets. Accordingly, different sampling and learning strategies such as active learning, theory-driven ML and probablistic approaches will be useful to improve learning efficiency, generalisability and to understand uncertainty in multiscale settings.

Closure

7.1 Summary

The goal of this thesis was to apply multiscale and multiphysics modelling concepts to the study of strongly heterogeneous (deformable) porous media, to better understand and represent the links between various scales of interest. For the multiscale component we were interested in the coupling between microscale and (macroscopic) dual-continuum representations. For the multiphysics component we were interested in the coupling between linear deformation and flow, referred to as poroelasticity. To address our goal we split this thesis into three parts concerned with the following objectives:

1. Investigate the relations between microscale and dual-continuum poroelastic consitutive models, including previously introduced phenomogelogical models, using micromechanical approaches.

2. Introduce a numerical framework for dual-continuum poroelastic modelling. Use the resulting framework to further study the links between different modelling scales given various material and modelling assumptions made at the microscale.

3. Establish a machine learning-based multiscale modelling approach to improve the accuracy of macroscopic models. Apply the resulting framework to the modelling of inter-continuum mass transfer.

Accordingly, in Part I we investigated the relations between microscopic and dual-continuum poroelastic constitutive behaviour using the framework of micromechanics. We derived a dual-continuum poroelastic constitutive model through homogenisation. We then showed how the resulting model reduces to previously introduced phenomological models under assumptions of material isotropy and stiffness properties of the fracture phase. For the remainder of Part I, we studied in further detail those previously introduced phenomenological models. In doing, we considered simplifying decoupling assumptions made by past users on

these models. Using micromechanical arguments we showed these decoupling assumptions to coincide with bounds on effective properties arising from geometric assumptions at the microscale. Using analytical solutions to a poroelastic model problem, we also demonstrated qualitatively the effects of using these decoupling assumptions (and resulting parameter bounds). Consequently, we recommended against the use of explicit decoupling assumptions without fully understanding their microscopic implications. Finally, through further qualitative studies, we showed that expressions for the effective constitutive parameters without intrinsic mechanical fracture properties (void space assumption) to be good starting points for using poroelastic constitutive models. Specifically, given the compliance of fractures compared to the stiffnesses of the other constituents, it is fair to neglect fracture stiffness effects.

In Part II we introduced a numerical framework for poroelastic dual-continuum modelling. The framework combines the finite-volume method for flow and the virtual-element method for mechanics. The former ensures local mass conservation with respect to the flow problem. The latter ensures the flexibility of the hybrid approach with respect to the complex grids encountered within the subsurface. We benchmarked the hybrid approach against analytical solutions and tested it on a geologic grid. We observed good results in both cases. With our framework, we further investigated links between microscale and dual-continuum poroelastic materials. In particular, we studied these links given various modelling and material assumptions made at the microscale. For the latter, we considered anisotropic effects. Through several tests of varying complexity we observed that anisotropy can have measurable impacts on flow and deformation behaviour. However, in all the cases considered, we showed the DC approach is able to capture the global poroelastic behaviours of equivalent microscale representations. Discrepancies between the two modelling approaches arose when local equilibration processes not accounted for in the homogenisation approach, were significant.

Finally, in Part III we presented a machine-learning based multiscale constitutive modelling framework. The framework itself is inspired by sequential computational multiscale approaches, where the machine learning model then acts as a bridge between scales. Accordingly, we introduced the framework describing the key components and considerations therein. We then applied the framework to the problem of modelling inter-continuum mass transfer for uncoupled (flow only) dual-materials. We reviewed various machine learning methods for modelling the time-dependent problem and injected the ensuing data-driven model into a physics-based simulator. We tested the resulting hybrid machine learning-physics-based approach against a dual-continuum model using the conventional linear transfer approximation and a microscale model. The

hybrid approach gave high quality results compared to the microscale reference solutions, without the computational expense of the latter.

7.2 Recommendations for future work

Throughout the course of this thesis we have endeavoured to highlight open questions and potential areas for future work. We summarise these accordingly.

7.2.1 Parameter measurement

In analogy to Biot and Willis (1957), it is highly desirable to develop methods of measurement for the parameters introduced in this work. However, this poses several challenges particularly to the current constitutive framework where we consider fractures as poroelastic continua at the microscale. Specifically, it is not clear how to map commonly measured planar properties such as the fracture normal and shear stiffnesses to continuum properties such as Young's modulus and Poisson's ratio. One possible solution to this is to model fractures as lower-dimensional objects at the microscale as done in discrete fracture network models (Berre et al. 2019). Such lower-dimensional objects naturally align with the planar properties typically measured on fractures (Garipov et al. 2016). At the macroscale we could then treat the dual-continuum model using the void space constitutive/coefficient models as a first approximation. Fracture stiffness effects would then be captured in the homogenised stiffness tensor. Additionally, analytical micromechanical approaches may also provide useful insights into experimental and theoretical methodologies for mapping such quantities (Lemarchand et al. 2009; Dormieux and Kondo 2016).

7.2.2 Multiscale effects

Nonlinear deformation and impacts on multiphysics

It is well recognised that heterogeneities such as fractures and inter-aggregate pores deform nonlinearly, and irreversibly, even under small deformations (Bemer et al. 2001; Deude et al. 2002; Lemarchand et al. 2009; Bidgoli et al. 2013; Borja and Choo 2016). As a result, we can expect geometric nonlinearities at the microscale to lead to material nonlinearities at the macroscale. Examples of such effects include hardening, stress-dependent permeability and evolving material anisotropy. Accordingly, impacts on flow are likely to be significant. Whilst incorporating nonlinear multiscale coupling effects is a necessary step towards more realistic models, doing it in practice is nontrivial. Multiscale analytical methods exist for nonlinear deformations within poroelasticity (Brown et al. 2014; Col-

lis et al. 2017). However, their use for practical applications remains limited at present (Concha and Hurtado 2020). Instead, the most promising approach to consider such phenomena is to use computational multiscale strategies (Geers et al. 2017). Challenges and recommendations for these latter approaches are discussed below.

Multiphase flows

Despite considering only single-phase flows in this work, extensions to multiphase systems are desirable given their propensity in the subsurface. However, the key challenge here is the formulation of an appropriate constitutive model in light of additional multiphysics couplings due to capillarity and surface energy effects between components at the microscale (Coussy 2004). Micromechanical approaches have been successfully applied to deriving such constitutive models in the case of single-porosity materials (Chateau and Dormieux 2002; Dormieux et al. 2006). However, the extension of these methods to the dual-continuum case still remains an open. One potential barrier to such developments in the case of fractures, is the paucity of experimental studies on multiphase flow through these materials.

7.2.3 Computational multiscale approaches

Numerical modelling

The main challenge for computational approaches to nonlinear hierarchical problems is the need for potentially significant developments in methods and software for modelling each scale. For example, realistic microscale simulations of fractures require specialised methods (e.g. discrete-element methods) to account for phenomena such as contact and sliding (Sun et al. 2013; Wang and Sun 2019). Additionally, finding efficient ways to couple between scales is a recurring theme when considering such approaches, particularly when realistic microscale simulations are considered. One possible solution to this latter problem is the use of machine learning. For the methods and software problem, despite the complexities of physics such as fracture mechanics (and assigning meaningful properties therein), treating fractures as continua at the microscale still provides useful insight into multiscale couplings. Accordingly, a good first step toward understanding the impacts of nonlinear microscale deformation would be to extend the numerical framework considered here to finite deformations (Chi et al. 2017).

With respect to the numerical methods used in this work, several interesting paths could be explored. For example, complex microstructures in hierarchical problems can pose challenges for conventional finite-element methods in terms of grid requirements (Rivarola et al. 2019). Such challenges may also be

encountered in concurrent multiscale settings. For example, when modelling nonhomogenisable phenomena such as the interface problems in faults or constructing the traces of large scale fractures (Benedetto et al. 2016; Wriggers et al. 2016). The flexibility of VEM could be used to address such issues in both hierarchical and concurrent multiscale settings. Further, several works, including this one, have shown the suitability of mixed discretisations to address coupled flow and deformation problems (Kim et al. 2009; Jha and Juanes 2014). However, previous computational multiscale studies applied to poroelasticity problems have used nested finite-element methods (e.g. Van den Eijnden et al. 2016). Accordingly, applying mixed discretisations for nested sequential multiscale and multiphysics problems still remains open.

Machine learning

Lastly, one of the fundamental challenges when using computational multiscale approaches is efficient information passing between scales. To address this, as well as other challenges, we could leverage the remarkable advances being made in machine learning. For future work, an exciting development building on the work done in this thesis, would be using theory-driven learning approaches to supplement microscale data. For example, given the mass-transfer case considered here, an interesting experiment is to see if we can supplement (or completely bypass) the data generation process by embedding the physics of the problem within the constitutive model learning step. Alternatively, we could explore if so-called generative models could be used to supplement expensive-to-compute training data using semi-supervised learning procedures. Finally, probablistic machine learning methods could further enhance multiscale capabilities. For example, using Bayesian inference we could provide feedback into when surrogate constitutive predictions are uncertain. In cases of high model (epistemic) uncertainty we could run the required explicit microscale simulation, feeding the results into a macroscale model whilst also adding them to an offline database for model retraining. Further, in high cost applications, such as those in the subsurface, understanding uncertainties is invaluable, especially if we can propagate aleatoric (data) uncertainties coming from the microscale as well.

Examples such as the above, are just some of the ways in which we could utilise the vast capabilities of machine learning within multiscale systems. We predict the intersection of these two fields to be an exciting area for future developments.

7.3 Final remarks

In science and engineering, developments are driven by our desire for greater understanding, accuracy and efficiency. Accordingly, multiscale approaches are indispensable in light of these goals, particularly as we seek to incorporate more scales of interest and (multi)physical phenomena when modelling. However, a key challenge is how to make multiscale methods efficient enough to be used at large scales or for computationally demanding tasks such as uncertainty quantification. Addressing this challenge will require further work in computational approaches, informed by analytical techniques where necessary. In this regard, we hope this thesis can be a stepping stone to further developments in multiscale methods and their applications to the subsurface.

A

Appendix: Maxwell symmetry relations

Here we present the Maxwell symmetry relations for a dual-continuum owing to the state equations in Eq. (2.18). Accordingly,

$$\frac{\partial^2 \mathcal{F}_s}{\partial E_{ij}\partial E_{kl}} \;:\; \frac{\partial \Sigma_{ij}}{\partial E_{kl}} = \frac{\partial \Sigma_{kl}}{\partial E_{ij}}, \tag{A.1}$$

$$\frac{\partial^2 \mathcal{F}_s}{\partial P_m \partial E_{ij}} \;:\; \frac{\partial \Sigma_{ij}}{\partial P_m} = -\frac{\partial \phi_m}{\partial E_{ij}}, \tag{A.2}$$

$$\frac{\partial^2 \mathcal{F}_s}{\partial P_f \partial E_{ij}} \;:\; \frac{\partial \Sigma_{ij}}{\partial P_f} = -\frac{\partial \phi_f}{\partial E_{ij}}, \tag{A.3}$$

$$\frac{\partial^2 \mathcal{F}_s}{\partial P_m \partial P_f} \;:\; \frac{\partial \phi_m}{\partial P_f} = \frac{\partial \phi_f}{\partial P_m}, \tag{A.4}$$

Note, Eq. (A.4) suggests $Q_m = Q_f$ in Eqs. (2.20) to (2.21) (resp. Eqs. (2.23) to (2.24)). However, from Eq. (2.101) and Eq. (2.103) we show this equivalence only holds when the matrix and fracture materials are isotropic.

Appendix: Dual-continuum Mandel solution

Here we present the solutions to the dual-continuum Mandel problem following the work of Nguyen and Abousleiman (2010). To start we present the poroelastic governing equations under assumptions of material isotropy, no gravity, use of a linear inter-continuum mass transfer model and assuming $\gamma' \approx 0$ such that

$$\boldsymbol{\Sigma} = 2G^*\mathbf{E} + \lambda^*E\mathbf{1} - \sum_{\alpha=m,f} B_\alpha P_\alpha \mathbf{1} = 0, \tag{B.5}$$

$$\frac{\partial}{\partial t}\left(B_m E + \frac{P_m}{M_m} + \frac{P_f}{Q}\right) - \nabla \cdot \left(\frac{K_m}{\mu_l}\nabla P_m\right) = \chi(P_f - P_m), \tag{B.6}$$

$$\frac{\partial}{\partial t}\left(B_f E + \frac{P_m}{Q} + \frac{P_f}{M_f}\right) - \nabla \cdot \left(\frac{K_f}{\mu_l}\nabla P_f\right) = \chi(P_m - P_f), \tag{B.7}$$

where we have replaced the coefficient of the linear transfer model coming from Eq. (2.7) with χ. Next, we give expressions for $\Sigma_{yy}(x, t)$ and $E_{yy}(y, t)$, which are used in the analyses in Chapter 3 and Chapter 4. First, integrating Eq. (2.4) in the x-direction given the assumptions above, whilst noting there is no applied stress at the boundaries $\pm h_1$ leads to

$$\Sigma_{xx} = 0. \tag{B.8}$$

From Eq. (B.5) and Eq. (B.8) we express the horizontal and vertical components of stress as

$$\Sigma_{xx} = 0 = 2G^*E_{xx} + \lambda^*E - B_m P_m - B_f P_f. \tag{B.9}$$

$$\Sigma_{yy} = 2G^*E_{yy} + \lambda^*E - B_m P_m - B_f P_f. \tag{B.10}$$

Using Eq. (3.50) in Eq. (B.10) to eliminate E leads to

$$\Sigma_{yy} = -2G^*C_m P_m - 2G^*C_f P_f + (2G^* + 2\lambda^*)I(t), \tag{B.11}$$

where we eliminate $E_{yy} = E - E_{xx}$. Finally, combining Eq. (B.10) with Eq. (B.11) leads to

$$E_{yy} = (2G^* + \lambda^*)I(t). \tag{B.12}$$

Accordingly, to calculate Σ_{yy} and E_{yy} we require expressions for $P_m(x,t)$, $P_f(x,t)$ and $I(t)$. With this goal in mind, we substitute Eq. (3.50) into Eqs. (B.6) to (B.7) leading to

$$\left(\mathcal{M}\frac{\partial}{\partial t} - \mathcal{K}\nabla^2 + \chi\right)\begin{bmatrix} P_m \\ P_f \end{bmatrix} = -\begin{bmatrix} B_m \\ B_f \end{bmatrix}\frac{\partial I(t)}{\partial t}, \tag{B.13}$$

where $\mathcal{M}$, $\mathbf{K}$ and χ in Eq. (B.13) are given as

$$\mathcal{M} = \begin{bmatrix} M_m^{-1} + B_m C_m & Q^{-1} + B_m C_f \\ Q^{-1} + B_f C_m & M_f^{-1} + B_f C_f \end{bmatrix}, \tag{B.14}$$

$$\mathcal{K} = \frac{1}{\mu_l}\begin{bmatrix} K_m & 0 \\ 0 & K_f \end{bmatrix}, \tag{B.15}$$

$$\chi = \chi\begin{bmatrix} 1 & -1 \\ -1 & 1 \end{bmatrix}, \tag{B.16}$$

Following Nguyen and Abousleiman (2010), the pressure solutions can be defined in terms of infinite series through combined Fourier and Laplace transformations. We do not go into details of this solution procedure but instead refer the interested reader towards Appendix D in Nguyen and Abousleiman (2010). However, we do provide resulting solutions for $I(t)$ and P_α. Accordingly, $I(t)$ is given as

$$I(t) = \frac{F}{2h_1\tau}\left\{1 + \sum_{i=1}^{\infty}\left[\frac{(e^{\omega_i t} - 1)}{\omega_i Q'(s = \omega_i)}\right]\right\}, \tag{B.17}$$

where s, $Q'(s)$ and ω_i denote the Laplace transform parameter, $dQ(s)/s$ and the roots of the equation $1 - Q(s) = 0$, respectively. $Q(s)$ is given by

$$Q(s) = \frac{2}{(h_1)^2\tau}\sum_{n=1}^{\infty}\frac{1}{\eta^2}\left(\frac{\Phi_{m,n}s_{m,n}}{s + s_{m,n}} - \frac{\Phi_{f,n}s_{f,n}}{s + s_{f,n}}\right), \tag{B.18}$$

where $\eta = (2n-1)\pi/2h_1$ denotes the Fourier transform parameter (for a given Fourier term n). The remaining parameters appearing in Eqs. (B.17) to (B.18)

will be given following the presentation of the solution for P_α. Accordingly, the solution for P_α is

$$P_\alpha(x,t) = \frac{Fq_\alpha}{(h_1)^2\tau} \sum_{n=1}^{\infty} \frac{(-1)^n}{\eta(s_{m,n} - s_{f,n})} \left\{ \left[(s_{m,n} - r_{\alpha,n})e^{-s_{m,n}t} \right.\right.$$

$$\left.\left. - (s_{f,n} - r_{\alpha,n})e^{-s_{f,n}t} \right] \left[1 + \sum_{i=1}^{\infty} \frac{(e^{\omega_i t} - 1)}{\omega_i Q'(\omega_i)} \right] \right\} \cos(\eta x). \qquad \text{(B.19)}$$

The remaining parameters appearing in Eqs. (B.17) to (B.19) are defined as

$$q_m = \frac{\mathcal{M}_{22}B_m - \mathcal{M}_{12}B_f}{\det(\mathcal{M})}, \quad q_f = \frac{\mathcal{M}_{11}B_f - \mathcal{M}_{21}B_m}{\det(\mathcal{M})}, \qquad \text{(B.20)}$$

$$r_{m,n} = \frac{[B_m(\eta^2\mathcal{M}_{22} + \chi) + B_f\chi)]}{q_m \det(\mathcal{M})}, \quad r_{f,n} = \frac{[B_f(\eta^2\mathcal{M}_{11} + \chi) + B_m\chi)]}{q_f \det(\mathcal{M})}, \qquad \text{(B.21)}$$

$$s_{\alpha,n} = -\frac{\left(-\mathcal{D} \pm \sqrt{\Delta}\right)}{2\det(\mathcal{M})}, \qquad \text{(B.22)}$$

$$\mathcal{D} = (\mathcal{M}_{11} + \mathcal{M}_{22} + \mathcal{M}_{12} + \mathcal{M}_{21})\chi + \eta^2(\mathcal{M}_{11}\mathcal{K}_{22} + \mathcal{M}_{22}\mathcal{K}_{11}), \qquad \text{(B.23)}$$

$$\Delta = \mathcal{D}^2 - 4\det(\mathcal{M})[(\eta^2\mathcal{K}_{11} + \chi)(\eta^2\mathcal{K}_{22} + \chi) - \chi^2], \qquad \text{(B.24)}$$

$$\tau = G^*C_m q_m + G^*C_f q_f + \frac{G^*}{1 - 2\nu^*}, \qquad \text{(B.25)}$$

$$\Phi_{\alpha,n} = \frac{G^*C_m q_m(s_{\alpha,n} - r_{m,n}) + G^*C_f q_f(s_{\alpha,n} - r_{f,n})}{(s_{m,n} - s_{f,n})}, \qquad \text{(B.26)}$$

where $\det(\cdot)$ denotes the determinant of a matrix.

References

Aboudi, J. (1991), *Mechanics of composite materials: a unified micromechanical approach*, Elsevier. (Cited on page 51.)

Adler, P. M., Thovert, J.-F. and Mourzenko, V. V. (2013), *Fractured porous media*, Oxford University Press. (Cited on page 2.)

Aifantis, E. C. (1977), 'Introducing a multi-porous medium', *Dev. Mech* **8**(3), 209–211. (Cited on pages 6 and 37.)

Aifantis, E. C. (1979), 'On the response of fissured rocks', *Dev. Mech* **10**, 249–253. (Cited on pages 6 and 37.)

Alber, M., Tepole, A. B., Cannon, W. R., De, S., Dura-Bernal, S., Garikipati, K., Karniadakis, G., Lytton, W. W., Perdikaris, P., Petzold, L. et al. (2019), 'Integrating machine learning and multiscale modeling—perspectives, challenges, and opportunities in the biological, biomedical, and behavioral sciences', *NPJ Digital Medicine* **2**(1), 1–11. (Cited on pages 5 and 100.)

Andersen, O., Nilsen, H. M. and Raynaud, X. (2017a), Coupled geomechanics and flow simulation on corner-point and polyhedral grids, *in* 'SPE Reservoir Simulation Conference', Society of Petroleum Engineers. (Cited on pages 69, 71, and 88.)

Andersen, O., Nilsen, H. M. and Raynaud, X. (2017b), 'Virtual element method for geomechanical simulations of reservoir models', *Computational Geosciences* **21**(5-6), 877–893. (Cited on pages 69, 71, 72, 73, and 74.)

Ashworth, M. and Doster, F. (2019a), An open source numerical framework for dual-continuum geomechanical simulation, *in* 'SPE Reservoir Simulation Conference', Society of Petroleum Engineers. (Cited on page 68.)

Ashworth, M. and Doster, F. (2019b), 'Foundations and Their Practical Implications for the Constitutive Coefficients of Poromechanical Dual-Continuum Models', *Transport in Porous Media* **130**(3), 699–730. (Cited on pages 12 and 35.)

Ashworth, M. and Doster, F. (2020), 'Anisotropic dual-continuum representations for multiscale poroelastic materials: Development and numerical modelling', *International Journal for Numerical and Analytical Methods in Geomechanics* . (Cited on pages 12, 35, 68, and 82.)

Asproulis, N. and Drikakis, D. (2013), 'An artificial neural network-based multiscale method for hybrid atomistic-continuum simulations', *Microfluidics and Nanofluidics* **15**(4), 559–574. (Cited on page 100.)

Auriault, J.-L. (2002), 'Upscaling heterogeneous media by asymptotic expansions', *Journal of Engineering Mechanics* **128**(8), 817–822. (Cited on pages 3 and 13.)

Babuška, I. (1976), Homogenization and its application. mathematical and computational problems, *in* 'Numerical Solution of Partial Differential Equations–III', Elsevier, pp. 89–116. (Cited on page 4.)

Babuska, V. and Cara, M. (1991), *Seismic anisotropy in the Earth*, Vol. 10, Springer Science & Business Media. (Cited on page 26.)

Bai, M., Meng, F., Elsworth, D., Abousleiman, Y. and Roegiers, J. (1999), 'Numerical modelling of coupled flow and deformation in fractured rock specimens', *International Journal for Numerical and Analytical Methods in Geomechanics* **23**(2), 141–160. (Cited on pages 6 and 69.)

Bai, S., Kolter, J. Z. and Koltun, V. (2018), 'An empirical evaluation of generic convolutional and recurrent networks for sequence modeling', *arXiv preprint arXiv:1803.01271* . (Cited on pages 100, 107, and 108.)

Barenblatt, G., Zheltov, I. and Kochina, I. (1960), 'Basic concepts in the theory of seepage of homogeneous liquids in fissured rocks [strata]', *Journal of Applied Mathematics and Mechanics* **24**(5), 1286–1303. (Cited on pages 3, 14, and 16.)

Bear, J. and Bachmat, Y. (1991), *Introduction to modeling of transport phenomena in porous media*, Kluwer. (Cited on pages 12, 13, and 20.)

Beirão da Veiga, L., Brezzi, F., Cangiani, A., Manzini, G., Marini, L. D. and Russo, A. (2013), 'Basic principles of virtual element methods', *Mathematical Models and Methods in Applied Sciences* **23**(01), 199–214. (Cited on pages 69, 72, and 73.)

Beirão da Veiga, L., Brezzi, F., Marini, L. D. and Russo, A. (2014), 'The hitchhiker's guide to the virtual element method', *Mathematical Models and Methods in Applied Sciences* **24**(08), 1541–1573. (Cited on pages 69 and 72.)

Bemer, E., Boutéca, M., Vincké, O., Hoteit, N. and Ozanam, O. (2001), 'Poromechanics: From linear to nonlinear poroelasticity and poroviscoelasticity', *Oil & Gas Science and Technology* **56**(6), 531–544. (Cited on pages 33 and 124.)

Benedetto, M. F., Berrone, S., Borio, A., Pieraccini, S. and Scialò, S. (2016), 'A hybrid mortar virtual element method for discrete fracture network simulations', *Journal of Computational Physics* **306**, 148–166. (Cited on page 126.)

Beran, M. (1971), 'Application of statistical theories to heterogeneous materials', *Physica Status Solidi (a)* **6**(2), 365–384. (Cited on page 20.)

Berkowitz, B. (2002), 'Characterizing flow and transport in fractured geological media: A review', *Advances in Water Resources* **25**(8-12), 861–884. (Cited on pages 2, 3, 14, 33, and 51.)

Berkowitz, B., Bear, J. and Braester, C. (1988), 'Continuum models for contaminant transport in fractured porous formations', *Water Resources Research* **24**(8), 1225–1236. (Cited on page 90.)

Berre, I., Doster, F. and Keilegavlen, E. (2019), 'Flow in fractured porous media: A review of conceptual models and discretization approaches', *Transport in Porous Media* **130**(1), 215–236. (Cited on pages 2, 14, and 124.)

Berryman, J. G. (2002), 'Extension of poroelastic analysis to double-porosity materials: New technique in microgeomechanics', *Journal of Engineering Mechanics* **128**(8), 840–847. (Cited on pages ix, xv, xvi, 7, 26, 35, 36, 40, 42, 43, 44, 51, 55, 56, and 57.)

Berryman, J. G. and Pride, S. R. (2002), 'Models for computing geomechanical constants of double-porosity materials from the constituents' properties', *Journal of Geophysical Research: Solid Earth* **107**(B3), ECV–2. (Cited on pages 7, 26, 35, and 36.)

Berryman, J. G. and Wang, H. F. (1995), 'The elastic coefficients of double-porosity models for fluid transport in jointed rock', *Journal of Geophysical Research: Solid Earth* **100**(B12), 24611–24627. (Cited on pages 7, 26, 35, 37, 39, 45, and 47.)

Bidgoli, M. N., Zhao, Z. and Jing, L. (2013), 'Numerical evaluation of strength and deformability of fractured rocks', *Journal of Rock Mechanics and Geotechnical Engineering* **5**(6), 419–430. (Cited on pages 33 and 124.)

Biot, M. A. (1941), 'General theory of three-dimensional consolidation', *Journal of Applied Physics* **12**(2), 155–164. (Cited on pages 6, 17, 27, and 32.)

Biot, M. A. and Temple, G. (1972), 'Theory of finite deformations of porous solids', *Indiana University Mathematics Journal* **21**(7), 597–620. (Cited on page 6.)

Biot, M. A. and Willis, D. (1957), 'The elastic coefficients of the theory of consolidation', *J Appl Mech* **15**, 594–601. (Cited on page 124.)

Bishop, A. W. (1959), 'The principle of effective stress', *Teknisk ukeblad* **39**, 859–863. (Cited on page 18.)

Bonnet, E., Bour, O., Odling, N. E., Davy, P., Main, I., Cowie, P. and Berkowitz, B. (2001), 'Scaling of fracture systems in geological media', *Reviews of Geophysics* **39**(3), 347–383. (Cited on page 3.)

Borja, R. I. (2006), 'On the mechanical energy and effective stress in saturated and unsaturated porous continua', *International Journal of Solids and Structures* **43**(6), 1764–1786. (Cited on page 18.)

Borja, R. I. and Choo, J. (2016), 'Cam-clay plasticity, part viii: A constitutive framework for porous materials with evolving internal structure', *Computer Methods in Applied Mechanics and Engineering* **309**, 653–679. (Cited on pages 33, 41, and 124.)

Borja, R. I. and Koliji, A. (2009), 'On the effective stress in unsaturated porous continua with double porosity', *Journal of the Mechanics and Physics of Solids* **57**(8), 1182–1193. (Cited on pages ix, 2, 7, 30, 33, 36, 39, 40, 41, 44, 47, 48, 56, 61, 62, and 63.)

Boucher, S. (1974), 'On the effective moduli of isotropic two-phase elastic composites', *Journal of Composite Materials* **8**(1), 82–89. (Cited on page 51.)

Bowen, R. M. (1982), 'Compressible porous media models by use of the theory of mixtures', *International Journal of Engineering Science* **20**(6), 697–735. (Cited on page 6.)

Brassart, L., Doghri, I. and Delannay, L. (2010), 'Homogenization of elasto-plastic composites coupled with a nonlinear finite element analysis of the equivalent inclusion problem', *International Journal of Solids and Structures* **47**(5), 716–729. (Cited on page 25.)

Brooks, R. J. and Tobias, A. M. (1996), 'Choosing the best model: Level of detail, complexity, and model performance', *Mathematical and Computer Modelling* **24**(4), 1–14. (Cited on page 1.)

Brown, D. L., Popov, P. and Efendiev, Y. (2014), 'Effective equations for fluid-structure interaction with applications to poroelasticity', *Applicable Analysis* **93**(4), 771–790. (Cited on page 124.)

Budiansky, B. (1965), 'On the elastic moduli of some heterogeneous materials', *Journal of the Mechanics and Physics of Solids* **13**(4), 223–227. (Cited on page 4.)

Burridge, R. and Keller, J. B. (1981), 'Poroelasticity equations derived from microstructure', *The Journal of the Acoustical Society of America* **70**(4), 1140–1146. (Cited on page 6.)

Callari, C. and Federico, F. (2000), 'FEM validation of a double porosity elastic model for consolidation of structurally complex clayey soils', *International Journal for Numerical and Analytical Methods in Geomechanics* **24**(4), 367–402. (Cited on page 37.)

Chateau, X. and Dormieux, L. (2002), 'Micromechanics of saturated and unsaturated porous media', *International Journal for Numerical and Analytical Methods in Geomechanics* **26**(8), 831–844. (Cited on pages 6, 28, and 125.)

Cheng, A. H.-D. (2016), *Poroelasticity*, Springer. (Cited on pages 43, 57, and 63.)

Chi, H., Da Veiga, L. B. and Paulino, G. (2017), 'Some basic formulations of the virtual element method (vem) for finite deformations', *Computer Methods in Applied Mechanics and Engineering* **318**, 148–192. (Cited on pages 69 and 125.)

Choo, J. and Borja, R. I. (2015), 'Stabilized mixed finite elements for deformable porous media with double porosity', *Computer Methods in Applied Mechanics and Engineering* **293**, 131–154. (Cited on pages 7, 16, 26, 36, 37, 41, 47, and 69.)

Choo, J., White, J. A. and Borja, R. I. (2016), 'Hydromechanical Modeling of Unsaturated Flow in Double Porosity Media', *International Journal of Geomechanics* **16**(6), D4016002. (Cited on pages 36, 37, 39, 41, 47, and 69.)

Chung, J., Gulcehre, C., Cho, K. and Bengio, Y. (2014), 'Empirical evaluation of gated recurrent neural networks on sequence modeling', *arXiv preprint arXiv:1412.3555* . (Cited on page 107.)

Collis, J., Brown, D., Hubbard, M. E. and O'Dea, R. D. (2017), 'Effective equations governing an active poroelastic medium', *Proceedings of the Royal Society A: Mathematical, Physical and Engineering Sciences* **473**(2198), 20160755. (Cited on page 124.)

Concha, F. and Hurtado, D. E. (2020), 'Upscaling the poroelastic behavior of the lung parenchyma: A finite-deformation micromechanical model', *Journal of the Mechanics and Physics of Solids* **145**, 104147. (Cited on page 125.)

Cordero, J. A. R., Sanchez, E. C. M. and Roehl, D. (2019), 'Integrated discrete fracture and dual porosity-dual permeability models for fluid flow in deformable fractured media', *Journal of Petroleum Science and Engineering* **175**, 644–653. (Cited on page 55.)

Coussy, O. (1995), *Mechanics of porous continua*, Wiley. (Cited on page 6.)

Coussy, O. (2004), *Poromechanics*, John Wiley & Sons. (Cited on pages 1, 6, 14, 15, 17, 18, 27, 30, 32, 40, 57, and 125.)

Crank, J. (1979), *The mathematics of diffusion*, Oxford university press. (Cited on page 105.)

Crombecq, K. (2011), Surrogate modeling of computer experiments with sequential experimental design, PhD thesis, Ghent University. (Cited on page 101.)

Da Veiga, L. B., Lovadina, C. and Mora, D. (2015), 'A virtual element method for elastic and inelastic problems on polytope meshes', *Computer Methods in Applied Mechanics and Engineering* **295**, 327–346. (Cited on page 73.)

Dalal, D. K. and Zickar, M. J. (2012), 'Some common myths about centering predictor variables in moderated multiple regression and polynomial regression', *Organizational Research Methods* **15**(3), 339–362. (Cited on page 109.)

Daniel, I. M., Ishai, O., Daniel, I. M. and Daniel, I. (1994), *Engineering mechanics of composite materials*, Vol. 3, Oxford university press New York. (Cited on page 87.)

De Boer, R. (2006), *Trends in continuum mechanics of porous media*, Vol. 18, Springer Science & Business Media. (Cited on page 6.)

Deude, V., Dormieux, L., Kondo, D. and Maghous, S. (2002), 'Micromechanical approach to nonlinear poroelasticity: application to cracked rocks', *Journal of Engineering Mechanics* **128**(8), 848–855. (Cited on pages 33 and 124.)

Dormann, C. F., Elith, J., Bacher, S., Buchmann, C., Carl, G., Carré, G., Marquéz, J. R. G., Gruber, B., Lafourcade, B., Leitao, P. J. et al. (2013), 'Collinearity: a review of methods to deal with it and a simulation study evaluating their performance', *Ecography* **36**(1), 27–46. (Cited on page 109.)

Dormieux, L. and Kondo, D. (2016), *Micromechanics of fracture and damage*, John Wiley & Sons. (Cited on page 124.)

Dormieux, L., Kondo, D. and Ulm, F.-J. (2006), *Microporomechanics*, John Wiley & Sons. (Cited on pages 6, 7, 19, 23, 26, 27, 28, 29, 31, 37, 39, 44, 50, 87, and 125.)

Egya, D. O., Geiger, S., Corbett, P. W. M., March, R., Bisdom, K., Bertotti, G. and Bezerra, F. (2019), 'Analysing the limitations of the dual-porosity response during well tests in naturally fractured reservoirs', *Petroleum Geoscience* **25**(1), 30–49. (Cited on page 7.)

Elsworth, D. and Bai, M. (1992), 'Flow-deformation response of dual-porosity media', *Journal of Geotechnical Engineering* **118**(1), 107–124. (Cited on pages 6, 26, and 37.)

Eshelby, J. D. (1957), 'The determination of the elastic field of an ellipsoidal inclusion, and related problems', *Proceedings of the royal society of London. Series A. Mathematical and physical sciences* **241**(1226), 376–396. (Cited on page 4.)

Feyel, F. (1999), 'Multiscale fe2 elastoviscoplastic analysis of composite structures', *Computational Materials Science* **16**(1-4), 344–354. (Cited on page 5.)

Fish, J. (2006), 'Bridging the scales in nano engineering and science', *Journal of Nanoparticle Research* **8**(5), 577–594. (Cited on page 4.)

Fornells, P., García-Aznar, J. M. and Doblaré, M. (2007), 'A finite element dual porosity approach to model deformation-induced fluid flow in cortical bone', *Annals of Biomedical Engineering* **35**(10), 1687–1698. (Cited on pages 37 and 69.)

Frey, J., Chambon, R. and Dascalu, C. (2013), 'A two-scale poromechanical model for cohesive rocks', *Acta Geotechnica* **8**(2), 107–124. (Cited on page 97.)

Gain, A. L., Talischi, C. and Paulino, G. H. (2014), 'On the virtual element method for three-dimensional linear elasticity problems on arbitrary polyhedral meshes', *Computer Methods in Applied Mechanics and Engineering* **282**, 132–160. (Cited on pages 72 and 73.)

Garipov, T., Karimi-Fard, M. and Tchelepi, H. (2016), 'Discrete fracture model for coupled flow and geomechanics', *Computational Geosciences* **20**(1), 149–160. (Cited on page 124.)

Geers, M. G., Kouznetsova, V. G. and Brekelmans, W. (2010), 'Multi-scale computational homogenization: Trends and challenges', *Journal of Computational and Applied Mathematics* **234**(7), 2175–2182. (Cited on pages 3 and 13.)

Geers, M. G., Kouznetsova, V. G., Matouš, K. and Yvonnet, J. (2017), 'Homogenization methods and multiscale modeling: nonlinear problems', *Encyclopedia of Computational Mechanics Second Edition* pp. 1–34. (Cited on pages 5 and 125.)

Geiger, S., Dentz, M., Neuweiler, I. et al. (2013), 'A novel multi-rate dual-porosity model for improved simulation of fractured and multiporosity reservoirs', *SPE Journal* **18**(04), 670–684. (Cited on pages 3 and 105.)

Geiger, S., Roberts, S., Matthäi, S. K., Zoppou, C. and Burri, A. (2004), 'Combining finite element and finite volume methods for efficient multiphase flow simulations in highly heterogeneous and structurally complex geologic media', *Geofluids* **4**(4), 284–299. (Cited on page 2.)

Gerke, H. H. (2006), 'Preferential flow descriptions for structured soils', *Journal of Plant Nutrition and Soil Science* **169**(3), 382–400. (Cited on page 2.)

Gerke, H. H. and Van Genuchten, M. T. (1993), 'A dual-porosity model for simulating the preferential movement of water and solutes in structured porous media', *Water Resources Research* **29**(2), 305–319. (Cited on page 3.)

Gers, F. A., Eck, D. and Schmidhuber, J. (2002), Applying lstm to time series predictable through time-window approaches, *in* 'Neural Nets WIRN Vietri-01', Springer, pp. 193–200. (Cited on page 108.)

Ghaboussi, J., Garrett Jr, J. and Wu, X. (1991), 'Knowledge-based modeling of material behavior with neural networks', *Journal of engineering mechanics* **117**(1), 132–153. (Cited on page 100.)

Ghaboussi, J., Pecknold, D. A., Zhang, M. and Haj-Ali, R. M. (1998), 'Autoprogressive training of neural network constitutive models', *International Journal for Numerical Methods in Engineering* **42**(1), 105–126. (Cited on page 100.)

Ghavamian, F. and Simone, A. (2019), 'Accelerating multiscale finite element simulations of history-dependent materials using a recurrent neural network', *Computer Methods in Applied Mechanics and Engineering* **357**, 112594. (Cited on pages 6, 100, and 107.)

Goh, A. T. (1995), 'Back-propagation neural networks for modeling complex systems', *Artificial Intelligence in Engineering* **9**(3), 143–151. (Cited on page 100.)

Haggerty, R. and Gorelick, S. M. (1995), 'Multiple-rate mass transfer for modeling diffusion and surface reactions in media with pore-scale heterogeneity', *Water Resources Research* **31**(10), 2383–2400. (Cited on pages 3, 105, and 119.)

Hajiabadi, M. R. and Khoei, A. R. (2019), 'A bridge between dual porosity and multiscale models of heterogeneous deformable porous media', *International Journal for Numerical and Analytical Methods in Geomechanics* **43**(1), 212–238. (Cited on page 55.)

Hambli, R., Katerchi, H. and Benhamou, C.-L. (2011), 'Multiscale methodology for bone remodelling simulation using coupled finite element and neural network computation', *Biomechanics and Modeling in Mechanobiology* **10**(1), 133–145. (Cited on page 100.)

Hashash, Y., Jung, S. and Ghaboussi, J. (2004), 'Numerical implementation of a neural network based material model in finite element analysis', *International Journal for Numerical Methods in Engineering* **59**(7), 989–1005. (Cited on page 103.)

Hashin, Z. (1972), *Theory of fiber reinforced materials*, NASA CR-1974. (Cited on pages 20, 21, 22, 23, 24, and 42.)

Hashin, Z. (1983), 'Analysis of composite materials—a survey', *Journal of Applied Mechanics* **50**(3), 481–505. (Cited on pages 4 and 20.)

Hashin, Z. and Shtrikman, S. (1963), 'A variational approach to the theory of the elastic behaviour of multiphase materials', *Journal of the Mechanics and Physics of Solids* **11**(2), 127–140. (Cited on pages 4 and 50.)

Hill, R. (1963), 'Elastic properties of reinforced solids: some theoretical principles', *Journal of the Mechanics and Physics of Solids* **11**(5), 357–372. (Cited on pages 3, 4, 23, 24, 25, 38, 46, and 49.)

Hill, R. (1965), 'Continuum micro-mechanics of elastoplastic polycrystals', *Journal of the Mechanics and Physics of Solids* **13**(2), 89–101. (Cited on page 4.)

Jaeger, J. C., Cook, N. G. and Zimmerman, R. (2009), *Fundamentals of rock mechanics*, John Wiley & Sons. (Cited on pages 26 and 51.)

Jha, B. and Juanes, R. (2014), 'Coupled multiphase flow and poromechanics: A computational model of pore pressure effects on fault slip and earthquake triggering', *Water Resources Research* **50**(5), 3776–3808. (Cited on pages 75 and 126.)

Jiang, J., Younis, R. M. et al. (2016), 'Hybrid coupled discrete-fracture/matrix and multicontinuum models for unconventional-reservoir simulation', *SPE Journal* **21**(03), 1–009. (Cited on page 81.)

Jozefowicz, R., Zaremba, W. and Sutskever, I. (2015), An empirical exploration of recurrent network architectures, *in* 'International conference on machine learning', pp. 2342–2350. (Cited on page 107.)

Karimi-Fard, M., Durlofsky, L. J., Aziz, K. et al. (2003), An efficient discrete fracture model applicable for general purpose reservoir simulators, *in* 'SPE Reservoir Simulation Symposium', Society of Petroleum Engineers. (Cited on pages 2 and 69.)

Khalili, N. (2003), 'Coupling effects in double porosity media with deformable matrix', *Geophysical Research Letters* **30**(22). (Cited on pages 6, 7, 39, 55, and 59.)

Khalili, N., Khabbaz, M. H. and Valliappan, S. (2000), 'An effective stress based numerical model for hydro-mechanical analysis in unsaturated porous media', *Computational Mechanics* **26**(2), 174–184. (Cited on pages 36 and 69.)

Khalili, N. and Selvadurai, A. P. S. (2003), 'A fully coupled constitutive model for thermo-hydro-mechanical analysis in elastic media with double porosity', *Geophysical Research Letters* **30**(24), 1–5. (Cited on page 39.)

Khalili, N. and Valliappan, S. (1996), 'Unified theory of flow and deformantion in double porous media', *European Journal of Mechanics. A. Solids* **15**(2), 321–336. (Cited on pages ix, 7, 26, 35, 36, 39, 40, 44, 45, 47, 48, 51, 54, 55, 56, 57, 59, 60, 61, 62, 63, and 76.)

Kim, J. and Moridis, G. J. (2013), 'Development of the t+ m coupled flow–geomechanical simulator to describe fracture propagation and coupled flow–thermal–geomechanical processes in tight/shale gas systems', *Computers & Geosciences* **60**, 184–198. (Cited on page 50.)

Kim, J., Sonnenthal, E. L. and Rutqvist, J. (2012), 'Formulation and sequential numerical algorithms of coupled fluid/heat flow and geomechanics for multiple porosity materials', *International Journal for Numerical Methods in Engineering* **92**(5), 425–456. (Cited on pages 36, 37, 43, 48, 50, 56, and 75.)

Kim, J., Tchelepi, H. A., Juanes, R. et al. (2009), Stability, accuracy and efficiency of sequential methods for coupled flow and geomechanics, *in* 'SPE reservoir simulation symposium', Society of Petroleum Engineers. (Cited on pages 68, 75, and 126.)

Koliji, A., Vulliet, L. and Laloui, L. (2008), 'New basis for the constitutive modelling of aggregated soils', *Acta Geotechnica* **3**(1), 61. (Cited on page 44.)

Kouznetsova, V., Brekelmans, W. and Baaijens, F. (2001), 'An approach to micro-macro modeling of heterogeneous materials', *Computational Mechanics* **27**(1), 37–48. (Cited on page 5.)

Kouznetsova, V., Geers, M. G. and Brekelmans, W. (2004), 'Multi-scale second-order computational homogenization of multi-phase materials: a nested finite element solution strategy', *Computer Methods in Applied Mechanics and Engineering* **193**(48-51), 5525–5550. (Cited on pages 4 and 13.)

Lea, C., Flynn, M. D., Vidal, R., Reiter, A. and Hager, G. D. (2017), Temporal convolutional networks for action segmentation and detection, *in* 'proceedings of the IEEE Conference on Computer Vision and Pattern Recognition', pp. 156–165. (Cited on page 107.)

Lemarchand, E., Davy, C. A., Dormieux, L., Chen, W. and Skoczylas, F. (2009), 'Micromechanics contribution to coupled transport and mechanical properties of fractured geomaterials', *Transport in Porous Media* **79**(3), 335–358. (Cited on pages 26, 33, and 124.)

Lemonnier, P. and Bourbiaux, B. (2010), 'Simulation of naturally fractured reservoirs. state of the art-part 2–matrix-fracture transfers and typical features of

numerical studies', *Oil & Gas Science and Technology–Revue de l'Institut Français du Pétrole* **65**(2), 263–286. (Cited on page 90.)

Levin, V. (1967), 'On the coefficients of thermal expansion of heterogeneous materials', *Mechanics of Solids* **2**, 58–61. (Cited on page 30.)

Lewandowska, J., Szymkiewicz, A., Burzyński, K. and Vauclin, M. (2004), 'Modeling of unsaturated water flow in double-porosity soils by the homogenization approach', *Advances in Water Resources* **27**(3), 283–296. (Cited on pages 3 and 7.)

Lewis, R. W. and Ghafouri, H. R. (1997), 'A novel finite element double porosity model for multiphase flow through deformable fractured porous media', *International Journal for Numerical and Analytical Methods in Geomechanics* **21**(11), 789–816. (Cited on pages 6 and 69.)

Lewis, R. W. and Schrefler, B. A. (1998), *The finite element method in the static and dynamic deformation and consolidation of porous media*, John Wiley & Sons. (Cited on page 75.)

Lie, K.-A. (2019), *An introduction to reservoir simulation using MATLAB/GNU Octave*, Cambridge University Press. (Cited on pages 68, 71, 72, 74, 75, and 114.)

Lie, K.-A., Krogstad, S., Ligaarden, I. S., Natvig, J. R., Nilsen, H. M. and Skaflestad, B. (2012), 'Open-source matlab implementation of consistent discretisations on complex grids', *Computational Geosciences* **16**(2), 297–322. (Cited on page 71.)

Lim, K. T. and Aziz, K. (1995), 'Matrix-fracture transfer shape factors for dual-porosity simulators', *Journal of Petroleum Science and Engineering* **13**(3-4), 169–178. (Cited on pages 3, 16, and 116.)

Ling, J., Jones, R. and Templeton, J. (2016), 'Machine learning strategies for systems with invariance properties', *Journal of Computational Physics* **318**, 22–35. (Cited on page 102.)

Long, J., Remer, J., Wilson, C. and Witherspoon, P. (1982), 'Porous media equivalents for networks of discontinuous fractures', *Water Resources Research* **18**(3), 645–658. (Cited on page 14.)

Loret, B. and Rizzi, E. (1999), 'Strain localization in fluid-saturated anisotropic elastic–plastic porous media with double porosity', *Journal of the Mechanics and Physics of Solids* **47**(3), 503–530. (Cited on pages 7, 26, 37, and 39.)

Lu, X., Giovanis, D. G., Yvonnet, J., Papadopoulos, V., Detrez, F. and Bai, J. (2019), 'A data-driven computational homogenization method based on neural networks for the nonlinear anisotropic electrical response of graphene/polymer nanocomposites', *Computational Mechanics* **64**(2), 307–321. (Cited on page 6.)

March, R., Doster, F. and Geiger, S. (2016), 'Accurate early-time and late-time modeling of countercurrent spontaneous imbibition', *Water Resources Research* **52**(8), 6263–6276. (Cited on page 90.)

Matouš, K., Geers, M. G., Kouznetsova, V. G. and Gillman, A. (2017), 'A review of predictive nonlinear theories for multiscale modeling of heterogeneous materials', *Journal of Computational Physics* **330**, 192–220. (Cited on pages 4, 5, and 99.)

Mehrabian, A. (2018), 'The poroelastic constants of multiple-porosity solids', *International Journal of Engineering Science* **132**, 97–104. (Cited on pages 36, 43, 48, 50, and 56.)

Mehrabian, A. and Abousleiman, Y. N. (2014), 'Generalized biot's theory and mandel's problem of multiple-porosity and multiple-permeability poroelasticity', *Journal of Geophysical Research: Solid Earth* **119**(4), 2745–2763. (Cited on pages 36, 37, 43, 48, 50, and 56.)

Mehrabian, A. and Abousleiman, Y. N. (2015), 'Gassmann equations and the constitutive relations for multiple-porosity and multiple-permeability poroelasticity with applications to oil and gas shale', *International Journal for Numerical and Analytical Methods in Geomechanics* **39**(14), 1547–1569. (Cited on page 50.)

Min, K.-B. and Jing, L. (2003), 'Numerical determination of the equivalent elastic compliance tensor for fractured rock masses using the distinct element method', *International Journal of Rock Mechanics and Mining Sciences* **40**(6), 795–816. (Cited on page 14.)

Min, K.-B., Rutqvist, J., Tsang, C.-F. and Jing, L. (2004), 'Stress-dependent permeability of fractured rock masses: a numerical study', *International Journal of Rock Mechanics and Mining Sciences* **41**(7), 1191–1210. (Cited on page 33.)

Moinfar, A., Varavei, A., Sepehrnoori, K., Johns, R. T. et al. (2013), Development of a coupled dual continuum and discrete fracture model for the simulation of unconventional reservoirs, *in* 'SPE Reservoir Simulation Symposium', Society of Petroleum Engineers. (Cited on page 81.)

Mori, T. and Tanaka, K. (1973), 'Average stress in matrix and average elastic energy of materials with misfitting inclusions', *Acta Metallurgica* **21**(5), 571–574. (Cited on page 4.)

Nelson, R. (2001), *Geologic analysis of naturally fractured reservoirs*, Gulf Professional Publishing. (Cited on pages 2 and 54.)

Nemat-Nasser, S. and Hori, M. (1993), *Micromechanics: overall properties of heterogeneous materials*, Elsevier. (Cited on pages 20, 23, and 51.)

Neuman, S. P. (1988), Stochastic continuum representation of fractured rock permeability as an alternative to the rev and fracture network concepts, *in* 'Groundwater Flow and Quality Modelling', Springer, pp. 331–362. (Cited on page 14.)

Nguyen, V. X. and Abousleiman, Y. N. (2010), 'Poromechanics solutions to plane strain and axisymmetric mandel-type problems in dual-porosity and dual-permeability medium', *Journal of Applied Mechanics* **77**(1). (Cited on pages 26, 36, 48, 50, 51, 53, 129, and 130.)

Nur, A. and Byerlee, J. (1971), 'An exact effective stress law for elastic deformation of rock with fluids', *Journal of Geophysical Research* **76**(26), 6414–6419. (Cited on page 18.)

Olsson, R. and Barton, N. (2001), 'An improved model for hydromechanical coupling during shearing of rock joints', *International Journal of Rock Mechanics and Mining Sciences* **38**(3), 317–329. (Cited on page 26.)

Open Porous Media Initiative (2015), 'Open datasets'.
    URL: *https://github.com/OPM/opm-data* (Cited on page 78.)

Ostoja-Starzewski, M. (2006), 'Material spatial randomness: From statistical to representative volume element', *Probabilistic Engineering Mechanics* **21**(2), 112–132. (Cited on page 13.)

Pao, W. K. and Lewis, R. W. (2002), 'Three-dimensional finite element simulation of three-phase flow in a deforming fissured reservoir', *Computer Methods in Applied Mechanics and Engineering* **191**(23-24), 2631–2659. (Cited on pages 37 and 69.)

Pascanu, R., Mikolov, T. and Bengio, Y. (2013), On the difficulty of training recurrent neural networks, *in* 'International conference on machine learning', pp. 1310–1318. (Cited on page 100.)

Pecullan, S., Gibiansky, L. and Torquato, S. (1999), 'Scale effects on the elastic behavior of periodic andhierarchical two-dimensional composites', *Journal of the Mechanics and Physics of Solids* **47**(7), 1509–1542. (Cited on page 87.)

Peng, G. C., Alber, M., Tepole, A. B., Cannon, W. R., De, S., Dura-Bernal, S., Garikipati, K., Karniadakis, G., Lytton, W. W., Perdikaris, P. et al. (2020),

'Multiscale modeling meets machine learning: What can we learn?', *Archives of Computational Methods in Engineering* pp. 1–21. (Cited on pages 5 and 100.)

Prévost, M., Lepage, F., Durlofsky, L. J. and Mallet, J.-L. (2005), 'Unstructured 3d gridding and upscaling for coarse modelling of geometrically complex reservoirs', *Petroleum Geoscience* **11**(4), 339–345. (Cited on page 69.)

Price, N. J. and Cosgrove, J. W. (1990), *Analysis of geological structures*, Cambridge University Press. (Cited on page 26.)

Pruess, K. et al. (1985), 'A practical method for modeling fluid and heat flow in fractured porous media', *Society of Petroleum Engineers Journal* **25**(01), 14–26. (Cited on page 3.)

Raissi, M., Perdikaris, P. and Karniadakis, G. E. (2019), 'Physics-informed neural networks: A deep learning framework for solving forward and inverse problems involving nonlinear partial differential equations', *Journal of Computational Physics* **378**, 686–707. (Cited on page 102.)

Razavi, S., Tolson, B. A. and Burn, D. H. (2012), 'Review of surrogate modeling in water resources', *Water Resources Research* **48**(7). (Cited on pages 5 and 101.)

Reuss, A. (1929), 'Berechnung der fließgrenze von mischkristallen auf grund der plastizitätsbedingung für einkristalle.', *ZAMM-Journal of Applied Mathematics and Mechanics/Zeitschrift für Angewandte Mathematik und Mechanik* **9**(1), 49–58. (Cited on pages 4 and 49.)

Rivarola, F., Benedetto, M., Labanda, N. and Etse, G. (2019), 'A multiscale approach with the virtual element method: Towards a ve2 setting', *Finite Elements in Analysis and Design* **158**, 1–16. (Cited on pages 97 and 125.)

Royer, P., Auriault, J.-L. and Boutin, C. (1996), 'Macroscopic modeling of double-porosity reservoirs', *Journal of Petroleum Science and Engineering* **16**(4), 187–202. (Cited on pages 3 and 104.)

Royer, P., Auriault, J.-L., Lewandowska, J. and Serres, C. (2002), 'Continuum modelling of contaminant transport in fractured porous media', *Transport in Porous Media* **49**(3), 333–359. (Cited on page 87.)

Samardzioska, T. and Popov, V. (2005), 'Numerical comparison of the equivalent continuum, non-homogeneous and dual porosity models for flow and transport in fractured porous media', *Advances in Water Resources* **28**(3), 235–255. (Cited on page 3.)

Sarma, P., Aziz, K. et al. (2004), New transfer functions for simulation of naturally fractured reservoirs with dual porosity models, *in* 'SPE Annual Technical Conference and Exhibition', Society of Petroleum Engineers. (Cited on page 90.)

Snow, D. T. (1969), 'Anisotropic permeability of fractured media', *Water Resources Research* **5**(6), 1273–1289. (Cited on page 26.)

Stephenson, D., Kermode, J. R. and Lockerby, D. A. (2018), 'Accelerating multiscale modelling of fluids with on-the-fly gaussian process regression', *Microfluidics and Nanofluidics* **22**(12), 139. (Cited on pages 5 and 6.)

Strang, G. (2019), *Linear algebra and learning from data*, Wellesley-Cambridge Press. (Cited on page 109.)

Sun, W., Kuhn, M. R. and Rudnicki, J. W. (2013), 'A multiscale dem-lbm analysis on permeability evolutions inside a dilatant shear band', *Acta Geotechnica* **8**(5), 465–480. (Cited on page 125.)

Taron, J., Elsworth, D. and Min, K. B. (2009), 'Numerical simulation of thermal-hydrologic-mechanical-chemical processes in deformable, fractured porous media', *International Journal of Rock Mechanics and Mining Sciences* **46**(5), 842–854. (Cited on page 37.)

Taylor, R., Simo, J., Zienkiewicz, O. and Chan, A. (1986), 'The patch test—a condition for assessing fem convergence', *International Journal for Numerical Methods in Engineering* **22**(1), 39–62. (Cited on page 73.)

Torquato, S. (1991), 'Random heterogeneous media: microstructure and improved bounds on effective properties', *Applied mechanics reviews* **44**(2), 37–76. (Cited on page 45.)

Torquato, S. (2002), *Random heterogeneous materials: microstructure and macroscopic properties*, Springer. (Cited on pages 51 and 84.)

Tuncay, K. and Corapcioglu, M. Y. (1995), 'Effective stress principle for saturated fractured porous media', *Water Resources Research* **31**(12), 3103–3106. (Cited on page 37.)

Tuncay, K. and Corapcioglu, M. Y. (1996), 'Wave propagation in fractured porous media', *Transport in Porous Media* **23**(3), 237–258. (Cited on page 37.)

Unger, J. F. and Könke, C. (2009), 'Neural networks as material models within a multiscale approach', *Computers & Structures* **87**(19-20), 1177–1186. (Cited on page 100.)

Van den Eijnden, A., Bésuelle, P., Chambon, R. and Collin, F. (2016), 'A fe2 modelling approach to hydromechanical coupling in cracking-induced localization problems', *International Journal of Solids and Structures* **97**, 475–488. (Cited on pages 27, 97, and 126.)

Vernerey, F. J. and Kabiri, M. (2014), 'Adaptive concurrent multiscale model for fracture and crack propagation in heterogeneous media', *Computer Methods in Applied Mechanics and Engineering* **276**, 566–588. (Cited on page 81.)

Voigt, W. (1887), *Theoretische studien über die elasticitätsverhältnisse der krystalle*, Königliche Gesellschaft der Wissenschaften zu Göttingen. (Cited on pages 4 and 46.)

Voigt, W. (1928), *Lehrbuch der Kristallphysik (mit Ausschluss der Kristalloptik)*, Springer-Verlag. (Cited on pages 4 and 46.)

Wang, H. F. (2000), *Theory of linear poroelasticity with applications to geomechanics and hydrogeology*, Princeton University Press. (Cited on pages 54 and 63.)

Wang, K. and Sun, W. (2016), 'A semi-implicit discrete-continuum coupling method for porous media based on the effective stress principle at finite strain', *Computer Methods in Applied Mechanics and Engineering* **304**, 546–583. (Cited on page 97.)

Wang, K. and Sun, W. (2018), 'A multiscale multi-permeability poroplasticity model linked by recursive homogenizations and deep learning', *Computer Methods in Applied Mechanics and Engineering* **334**, 337–380. (Cited on pages 5, 6, 33, 37, 97, 100, 102, and 107.)

Wang, K. and Sun, W. (2019), 'An updated lagrangian lbm–dem–fem coupling model for dual-permeability fissured porous media with embedded discontinuities', *Computer Methods in Applied Mechanics and Engineering* **344**, 276–305. (Cited on pages 33, 97, and 125.)

Wang, N., Zhang, D., Chang, H. and Li, H. (2020), 'Deep learning of subsurface flow via theory-guided neural network', *Journal of Hydrology* **584**, 124700. (Cited on page 118.)

Wang, R., Kashinath, K., Mustafa, M., Albert, A. and Yu, R. (2020), Towards physics-informed deep learning for turbulent flow prediction, *in* 'Proceedings of the 26th ACM SIGKDD International Conference on Knowledge Discovery & Data Mining', pp. 1457–1466. (Cited on page 118.)

Warren, J. E. and Root, P. J. (1963), 'The behavior of naturally fractured reservoirs', *Society of Petroleum Engineers Journal* **3**(03), 245–255. (Cited on pages 3, 15, 16, and 103.)

Watt, J. P., Davies, G. F. and O'Connell, R. J. (1976), 'The elastic properties of composite materials', *Reviews of Geophysics* **14**(4), 541–563. (Cited on pages 38 and 51.)

Weinan, E. (2011), *Principles of multiscale modeling*, Cambridge University Press. (Cited on pages 5, 6, and 99.)

Wilson, R. K. and Aifantis, E. C. (1982), 'On the theory of consolidation with double porosity', *International Journal of Engineering Science* **20**(9), 1009–1035. (Cited on pages 6 and 37.)

Witherspoon, P. A., Wang, J. S., Iwai, K. and Gale, J. E. (1980), 'Validity of cubic law for fluid flow in a deformable rock fracture', *Water Resources Research* **16**(6), 1016–1024. (Cited on pages 54 and 83.)

Wriggers, P., Rust, W. and Reddy, B. (2016), 'A virtual element method for contact', *Computational Mechanics* **58**(6), 1039–1050. (Cited on page 126.)

Xiao, N.-C., Zuo, M. J. and Zhou, C. (2018), 'A new adaptive sequential sampling method to construct surrogate models for efficient reliability analysis', *Reliability Engineering & System Safety* **169**, 330–338. (Cited on page 101.)

Yoon, H. C. and Kim, J. (2018), 'Spatial stability for the monolithic and sequential methods with various space discretizations in poroelasticity', *International Journal for Numerical Methods in Engineering* **114**(7), 694–718. (Cited on page 68.)

Zaoui, A. (2002), 'Continuum micromechanics: survey', *Journal of Engineering Mechanics* **128**(8), 808–816. (Cited on page 23.)

Zhang, Q., Choo, J. and Borja, R. I. (2019), 'On the preferential flow patterns induced by transverse isotropy and non-darcy flow in double porosity media', *Computer Methods in Applied Mechanics and Engineering* . (Cited on pages 26, 36, 37, 85, and 90.)

Zhou, Q., Oldenburg, C. M., Spangler, L. H. and Birkholzer, J. T. (2017), 'Approximate solutions for diffusive fracture-matrix transfer: Application to storage of dissolved co2 in fractured rocks', *Water Resources Research* **53**(2), 1746–1762. (Cited on page 90.)

Zhu, Y., Zabaras, N., Koutsourelakis, P.-S. and Perdikaris, P. (2019), 'Physics-constrained deep learning for high-dimensional surrogate modeling and uncertainty quantification without labeled data', *Journal of Computational Physics* **394**, 56–81. (Cited on pages 102 and 118.)

Zimmerman, R. (2000), 'Coupling in poroelasticity and thermoelasticity', *International Journal of Rock Mechanics and Mining Sciences* **37**(1-2), 79–87. (Cited on page 17.)

Zimmerman, R. W., Chen, G., Hadgu, T. and Bodvarsson, G. S. (1993), 'A numerical dual-porosity model with semianalytical treatment of fracture/matrix flow', *Water Resources Research* **29**(7), 2127–2137. (Cited on pages 3, 16, 90, and 104.)